Gulf General Atomic
Incorporated
P.O. Box 608, San Diego, California 92112

AEC RESEARCH AND
DEVELOPMENT REPORT

GA-9639

GAS-COOLED FAST BREEDER REACTOR

QUARTERLY PROGRESS REPORT

FOR THE PERIOD MAY 1, 1969 THROUGH JULY 31, 1969

by

Project Staff

Prepared under
Contract AT(04-3)-167
Project Agreement No. 23
for the
San Francisco Operations Office
U. S. Atomic Energy Commission

Gulf General Atomic Project 393

August 30, 1969

Progress Report Series

Annual

GA-5537	November 1, 1963 to July 31, 1964
GA-6667	August 1, 1964 to July 31, 1965
GA-7645	August 1, 1965 to July 31, 1966
GA-8107	August 1, 1966 to July 31, 1967
GA-8787	August 1, 1967 to July 31, 1968

Quarterly

GA-8895	August 1, 1968 through October 31, 1968
GA-9229	November 1, 1968 through January 31, 1969
GA-9359	February 1, 1969 through April 30, 1969

CONTENTS

CONTENTS (Continued)

FIGURES

FIGURES (Continued)

TABLES

TABLES (Continued)

1. INTRODUCTION

Gulf General Atomic Incorporated is in its sixth year of work on the Gas-Cooled Fast Breeder Reactor (GCFR) concept under Atomic Energy Commission (AEC) sponsorship. The program effort consists of four tasks: program planning, core design, fuels and materials development, and reactor physics. The broad objectives of the four tasks and the current efforts on each task are summarized below.

1.1. TASK A - PROGRAM PLANNING

In Task A, a plan for development and demonstration of the GCFR concept is prepared.

The planning effort is focused on a detailed definition of the work required to develop a proved core design. A revision of portions of the GCFR Core Development Plan (Ref. 1)*, modified to include the necessary evaluation of the metal swelling phenomenon that occurs in a fast-flux environment, was submitted to the AEC. Specific comments received from the AEC and from Oak Ridge National Laboratory (ORNL) reviewers are being reviewed so that the Core Development Plan can be updated.

A comparison of irradiation facilities and their applicability to the GCFR program has been made. The facilities were evaluated for their heat-sink, pumping, test-space, and heat-transfer capacities in their present configurations, and modifications which may be required were determined. The comparison will appear among some updating revisions in the GCFR Core Development Plan (Ref. 1).

---

*References are listed by section.

1.2. TASK B - CORE DESIGN

In Task B, further detailed analysis of the referenced fuel-rod concept and an analysis of alternative core design concepts are made. Core design work during this period has been concerned with fuel-rod concept evaluation and development of an analytical model for the mechanical behavior of the GCFR fuel rods.

A status report on the CRECOL development code, which is used to predict the behavior of sealed-rod cladding in a pressurized environment, was completed. Since the pressure-balanced manifolded concept has been selected as the reference concept for GCFR, a lower priority was placed on the backup sealed rod, and further work on CRECOL was postponed.

Future analysis and design effort will emphasize (1) the development of the analytical model (BRITL) for the mechanical behavior of the reference manifolded-type GCFR fuel rod under irradiation and (2) the cumulative damage to the cladding and fuel-swelling conditions.

1.3. TASK C — FUELS AND MATERIALS DEVELOPMENT

The objectives of Task C are: (1) to review the work from related programs, particularly the Liquid Metal Fast Breeder Reactor (LMFBR), that is applicable to GCFR and (2) to perform in-pile and out-of-pile tests as part of the overall fuel-element development program for the GCFR.

During the present quarter surveillance was carried out in a number of selected areas. A review of fuel-rod performance under irradiation is continuing, and the objectives of this review and the experiments being evaluated for application to GCFR are discussed. A preliminary review of the creep of oxide fuels has failed to indicate a reliable basis for estimating the irradiation behavior of mixed oxide fuels. A study of the annealing of irradiation-induced swelling of the cladding and the structural materials

was made. This study indicated the conditions under which annealing may be feasible on GCFR cladding and core materials. Also, a survey of information available on transient fuel-rod behavior has been initiated.

Fuel irradiation in the Oak Ridge Research Reactor (ORR) is part of a joint Gulf General Atomic Incorporated (GGA) - ORNL program in the screening tests of fuel-rod materials and the selection of a fuel-rod concept and design. Fission-gas analyses were performed on three sealed $(Pu-U)O_2$ fuel rods irradiated in ORR thermal flux to exposures ranging from 47,000 to 59,000 MWd/Te, and the end-of-life gas pressures internal to the rods have been calculated. Fabrication of the instrumented manifolded type $(Pu-U)O_2$ fuel rod for the ORR 04P9 capsule irradiation test has been completed. The startup of 04P9 irradiation to the goal burnup of 50,000 MWd/Te is now scheduled for October 17, 1969.

As a prelude to first fast-flux irradiations under the GCFR program, design modifications of a standard B-7 EBR-II subassembly to allow irradiation of a $(Pu-U)O_2$-fueled GCFR rods are being examined.

Out-of-pile testing includes thermal-cycling a section of a fuel rod under simulated GCFR pressure and temperature conditions to study fuel-cladding interaction. Check-out test runs of the out-of-pile thermal cycling rig at linear heat generation ratings of 12 kW/ft are continuing, and plans are being formulated for a test program employing this rig.

1.4. TASK D - REACTOR PHYSICS PROGRAM

Task D is currently a continuation of the critical experiments to be performed cooperatively with the Battelle Northwest Laboratory (BNWL) critical facility. The experimental program planned for the 1 to 1, H to Pu ratio plutonium-fueled assemblies consisted of:

1. Measurement of the critical mass and size of an unclad, near-cube shape plutonium fuel with a 1 to 1,H to Pu ratio

2. Measurement of the critical size and mass of an unclad, plutonium-fueled assembly of 1 to 1,H to Pu ratio with a base size suitable for the resonance-poison plates (e.g., 12 in. x 18 in.).

3. Measurement of the critical size and mass of an unclad, plutonium-fueled assembly of 1 to 1,H to Pu ratio containing layers of resonance-poison plates:

   a. with gadolinium-oxide plates
   b. with hafnium-oxide plates
   c. with dysprosium-oxide plates

   The number of poison layers added to be limited by the fuel available for criticality.

4. Measurement of the fission ratios for Pu-239 and U-235 in the unclad 1 to 1, H to Pu assembly (item 1) and flux distribution measurements in this unclad assembly and at least one of the poisoned systems.

All the experiments, with the exception of the fission ratio and flux distribution measurements, have been completed, and an analysis of the results is underway.

Severe radiation and heating problems were encountered with the 1 to 1 fuel, with the result that it was found impossible to perform the fission ratio and flux measurements because these experiments require considerable irradiation time in the critical assembly. Several alternative experiments of interest in the GCFR program will be performed in place of these measurements. These alternative experiments were not included

in the initial experimental program due to budget and time limitations. The choice of the particular experiments will be made after the analysis of the completed measurements.

REFERENCE

1. "Gas-Cooled Fast Breeder Reactor Development Plan,Section 4XXX, Core Development," USAEC Report GA-8009, Gulf General Atomic Incorporated, October 30, 1968.

2. TASK A - PROGRAM PLANNING

During the quarter the GCFR Core Development Plan (Ref. 1) was approved by the AEC subject to certain comments and suggestions. These are now being studied, and revisions are being made in the plan, as appropriate.

2.1. COMPARISON OF POTENTIAL IRRADIATION FACILITIES

Data contained in Table 4400-1 of Ref. 1 have been updated and revised. The usefulness of various loop irradiation facilities to the GCFR program was evaluated quantitatively with respect to their (1) heat-sink capacity, (2) pumping capacity, (3) test-section space, and (4) heat-transfer capacity. This was done by expressing the capability of each facility in terms of equivalent numbers of GCFR rods using the 1000 MW(e) GCFR described in Ref. 2 for the reference conditions.

Equivalence among the various facilities was computed. The heat-sink capacity is found as follows:

$$\text{Equivalent No. of GCFR rods} = \frac{\text{design heat-sink capacity of facility}}{\text{average heat rating of GCFR rod}}$$

The hydraulic pumping power expended P_h (pumping capacity) in the test section is

$$P_h = C_1 \, F(\Delta P), \tag{2.1}$$

where P_h = hydraulic power

C_1 = conversion constant

F = volumetric flow rate

ΔP = pressure loss in the test section

Using

$$\rho = P/RT \text{ and } F = \frac{\omega}{\rho M} ,$$

where P = pressure

ρ = density of gas

R = gas constant

T = absolute temperature of gas

ω = mass flow rate

M = molecular weight of gas

and substituting into Eq. 2.1 gives

$$P_h = C_1 \, RT \quad \frac{\omega(\Delta P)}{MP} . \tag{2.2}$$

If T is held constant, the hydraulic power is proportional to the factor in parentheses. Then the equivalent number of GCFR rods is found by

$$\text{Equivalent No. GCFR rods} = \frac{P_h \text{ (facility)}}{P_h \text{ (required by one GCFR rod)}} .$$

In some cases, it was of interest to know the pumping capacity when the gas was changed, for instance, changing a facility design for CO_2 to He cooling without changing the blowers. In these transformations it was assumed that the blowers were constant volumetric-rate pumps and could deliver the same pumping power. Therefore, using Eq. 2.2 to equate the pumping power with the original (subscript) and substitute (subscript 2) coolant gases,

$$\frac{\omega_2(\Delta P)_2}{M_2 \, P_2} = \frac{\omega_1 \, (\Delta P)_1}{M_1 \, P_1} . \tag{2.3}$$

Pressure drop through the core is

$$\Delta P = \left(f \frac{L}{D} \frac{RT}{A_t^2 \, 2g} \right) \frac{\omega^2}{P} .$$

If the geometry of the elements is not changed and T is held constant, then

$$\Delta P = \frac{K_1 \, \omega^2}{P} , \tag{2.4}$$

where K_1 is a proportionality constant defined as follows:

$$K_1 = f \frac{L}{D} \left(\frac{RT}{A_c^2 \quad 2g} \right) ,$$

where f = friction coefficient
L = channel length
D = channel diameter
A_c = channel cross-sectional flow area
g = conversion constant

and R and T have been previously defined, K_1 can be found from the initial conditions:

$$K_1 = \frac{P_1 \, (\Delta P_1)}{\omega_1^2}$$

and

$$(\Delta P)_2 = K_1 \quad \frac{\omega_2^2}{P_2} .$$

Then it is found that

$$\omega_2 \, (\Delta P)_2 = \omega_1 \, (\Delta P)_1 \, \frac{M_2 \, P_2}{M_1 \, P_1}$$

from the solution of Eq. 2.3, whereupon

$$\omega_2 = \omega_1 \left(\frac{P_2}{P_1}\right)^{2/3} \left(\frac{M_2}{M_1}\right)^{1/3}$$

and

$$(\Delta P)_2 = (\Delta P)_1 \left(\frac{P_2}{P_1}\right)^{1/3} \left(\frac{M_2}{M_1}\right)^{2/3} .$$

By selecting the new gas and its pressure at the conditions required, compatible flow and ΔP conditions could be derived.

2.2. TEST-SECTION SPACE

The test-section space capacity was evaluated by the cross-sectional area only. A separate evaluation of test-section length was not carried out since in most facilities a reasonable length of 2 to 3 ft is available.

The cross-sectional area of the free area of the test-section hole was computed and then this value was divided by the cross-sectional area of a GCFR rod plus its associated coolant flow area (i.e., the area of a unit cell around a rod) to determine the equivalent number of rods for the test section.

2.3. HEAT TRANSFER CAPACITY

The heat transfered to the cooling gas is

$$q = \omega \, C_p \, \Delta T,$$

where q = heat rate to gas

C_p = heat capacitance at constant pressure

ΔT = temperature rise across the test section

The maximum temperature limits of all the facilities are higher than the required coolant temperatures for testing GCFR rods. If it is assumed that C_p and ΔT are constant and limited by materials, the heat removal capability depends on how much gas can be pumped through the core. From Eq. 2.4 this is seen to be

$$\omega^2 = K_1 P(\Delta P),$$

where fuel element geometry and T are not changed.

Thus, it is seen that

$$q = \left[K_1^{1/2} C_p (\Delta T)\right] \left[P(\Delta P)\right]^{1/2} \tag{2.5}$$

and

$$\text{Equivalent No. GCFR rods} = \frac{g \text{ (facility)}}{g \text{ (one GCFR rod)}} = \left[\frac{P_1 (\Delta P_1)}{P_2 (\Delta P_2)}\right]^{\frac{1}{2}}$$

where subscripts 1 and 2 refer to the facility and GCFR, respectively.

The facilities listed in the original table, Table 4400-1 of Ref. 1, were evaluated on the above basis and compared. The results were tabulated as shown in Table 2.1. The table readily shows any imbalance in the facility design with respect to GCFR testing. The most limiting capability of each facility is footnoted in the table. Also, this evaluation is based on an advanced 1000 MW(e) GCFR, and generally less capacity would be required for early testing for a demonstration GCFR. This evaluation pertains only to the heat power characteristics and not to other important problems, such as time to reach burnup and fast fluence goals.

TABLE 2.1

COMPARISON OF IRRADIATION FACILITIES
FOR GCFR FUEL DEVELOPMENT TESTING

Facility Identification	Coolant Pressure (atm)	Heat Sink Capacity (rod)	Pumping Capacity (rod)	Test Section Space Capacity (rod)	Heat Transfer Capacity (rod)
Gas-Cooled Fast Breeder Reactor, GCFR (per rod)	85.0 He	1.0	1.0	1.0	1.0
Oak Ridge Research Reactor, ORR Loop 1	40 He	1.5	0.72	0.98	0.28[a]
Test Reactor BR-2 Mol Belgium-gas loop, BR-2GL	60 CO_2	6.25[a]	9.5	15	11
Advanced Test Reactor-gas loop, ATR-GCL	20 He	15[a]	80	51	30
Plutonium Recycle Test Reactor-gas loop, PRTR-GL	34 CO_2	12.5	5[a]	16	8.3
Fast-Flux Test Facility-gas loop 1, FFTF-GL1[b]	68 He	50	26[a]	45	47
Fast-Flux Test Facility-gas loop 2, FFTF-GL2[b]	68 He	7.5	4.3[a]	8.8	9.2
Gas-Cooled Fast Breeder Reactor Experiment, GCFRE	68 He	-	80[a]	205	151

[a] Most limiting capability of facility.

[b] The characteristics of these loops are based on requirements to test GCFR fuel elements in the FFTF as described in Ref. 3.

REFERENCES

1. "Gas-Cooled Fast Breeder Reactor Development Plan, Section 4XXX," USAEC Report GA-8009, Gulf General Atomic Incorporated, October 30, 1968.

2. "An Evaluation of Alternate Cooled Fast Breeders," ORNL Topical Report, Oak Ridge National Laboratory, March 13, 1968.

3. "Functional Test Requirements for the Fast Flux Test Facility in Support of Gas-Cooled Fast Reactor Development," USAEC Report GA-8061, General Dynamics, General Atomic Division, June 28, 1967.

3. TASK B - CORE DESIGN

The title of this task has been changed from "Core Development" by direction of AEC. Work formerly included on surveillance of relevant LMFBR fuel work has been moved to Task C and is reported in Section 4.

3.1. FUEL-ROD CONCEPT EVALUATION

In the prior reports (Refs. 1,2) the main fuel-rod concepts were discussed and recommendations were made for the selection of a reference fuel-rod concept and an alternative, or backup, concept. The manifolded fuel rod was selected as the reference concept for further detailed GCFR system study and experimental work. The fuel-cladding-interacting fuel rod, which employs a relatively strong cladding as a sealed can, was selected as the alternative.

Analysis work on creep collapse of cladding which applies to the alternative fuel rod concept has been summarized (Ref. 3). Future analysis and design effort will emphasize the development of an analytical model of the mechanical behavior of the reference GCFR fuel rod under irradiation and fuel swelling conditions.

During the operating lifetime of the fuel rods, the nonpressure-equalized design is subject to an applied pressure differential that tends to cause creep collapse of the cladding. The CRECOL computer code was developed as a design tool for predicting the creep deformation of fuel cladding under reactor operation conditions. Since the pressure-balanced, manifolded fuel rod has been selected as the reference concept, a lower-priority has been placed on the sealed rod as a backup concept and continued development of CRECOL, and further work is being postponed. A status report on CRECOL that describes its current configuration was completed during this period.

3.2. FUEL-ROD BEHAVIOR MODEL

The analytical model of the mechanical behavior of the GCFR fuel element presently in use at GGA (BRITL) considers the interaction of a swelling fuel with a metallic cladding. Creep strains of the cladding and of the fuel, which is considered to be cracked radially due to thermal stresses, are calculated using a visco-elastic approach; the radial cracks in the fuel are allowed to close as a result of subsequent swelling and creep. When BRITL was written, some of the material properties necessary for the calculation were unknown, and assumptions were necessary to solve the problem. Most of these unknown data are now or shortly will be available. Also, new properties in the fast-reactor environment have been discovered. To allow inclusion of the new data, BRITL is being altered to make it as general as possible.

Work has been initiated on the alteration of the model. It is planned to include calculations of fuel swelling, fuel creep, cladding creep, and cumulative exhaustion of cladding ductility as subroutines to the main program. Also, cladding swelling, which has not been considered previously, will be included.

A number of fuel swelling models have been described in the literature. These models usually consider that fuel swelling is a function of temperature, burnup, porosity, and local hydrostatic stress. It is planned to investigate the effect of the different swelling models on the calculated fuel-element behavior using the new program.

Little data are presently available on creep of $(Pu,U)O_2$. However, examples of the variables that probably affect creep and that can be considered in the new BRITL program when data become available are temperature, stress, fission rate, and porosity. Similarly, the effects of important variables on cladding swelling, creep, and ductility can be considered.

REFERENCES

1. "Gas-Cooled Fast Breeder Reactor, Quarterly Progress Report for the period August 1, 1967 through July 31, 1968," USAEC Report GA-8787, Gulf General Atomic Incorporated, September 20, 1968.

2. "Gas-Cooled Fast Breeder Reactor, Quarterly Progress Report for the Period August 1 through October 31, 1968," USAEC Report GA-8895, Gulf General Atomic Incorporated, December 2, 1968.

3. Hopkins, H. C., Jr., and D. R. Buttemer, "CRECOL, A Computer Program for Estimating Creep Deformation of Slightly Oval Tubes," USAEC Informal Report GAMD-9623, to be published.

4. TASK C - FUELS AND MATERIALS DEVELOPMENT

During the present quarter, surveillance was carried out in a number of selected areas. A review of fuel-rod performance under irradiation is continuing, and the objectives of this review and the experiments being evaluated for application to GCFR are discussed. A preliminary review of the creep of oxide fuels has indicated no reliable basis for estimating the irradiation behavior of mixed oxide fuels. A study of annealing or irradiation-induced swelling of cladding and structural materials was made, which indicated the conditions under which annealing may be feasible on GCFR cladding and core materials. Also, a survey of information available on transient fuel-rod behavior has been initiated.

Fission gas analyses were performed on three sealed $(Pu,U)O_2$-fueled rods irradiated in ORR thermal flux to exposures ranging from 47,000 to 59,000 MWd/Te, and the end-of-life gas pressures internal to the rods have been calculated.

Fabrication of the instrumented manifolded type $(Pu,U)O_2$ fuel rod for the ORR 04P9 capsule irradiation test has been completed. The startup of 04P9 irradiation to a goal burnup of 50,000 MWd/Te is now scheduled for October 17, 1969.

As a prelude to first fast-flux irradiations under the GCFR program, design modifications of a standard B-7 EBR-II subassembly to allow irradiation of $(Pu,U)O_2$-fueled GCFR rods are being examined.

Check-out test runs of the out-of-pile thermal cycling rig at linear heat generation ratings of 12 kW/ft are continuing and plans are being formulated for a test program employing this rig.

4.1. REVIEW OF LMFBR FUEL WORK

Since the requirements for the GCFR fuel-rod design have a great deal in common with those for the Liquid Metal Fast Breeder Reactor (LMFBR), a continuing review of results of LMFBR work, as well as of other relevant work, is an essential part of this GCFR task.

The criterion for admissibility of data from this surveillance program is the relation of the data to the design parameters and operating conditions for the GCFR. The primary sources of information are the USAEC and U.K. LMFBR fuel and materials development and irradiations programs. In general, the GCFR fuel-element design parameters and core conditions are in the same range as the LMFBR. A major difference is that the maximum cladding surface temperature of the GCFR may be approximately 700 C to 800 C, compared with approximately 650 C to 700 C for the LMFBR. The only other essential difference is the use of pressurized (approximately 1000 to 1250 psi) inert helium gas instead of liquid sodium as the coolant.

Because the pressure difference across the cladding is minimized, the commonality of the GCFR with the LMFBR is increased further with the use of the manifolded pressure-equalizing fuel-rod design for the GCFR. The pressure difference in the GCFR fuel rod remains at a low value throughout its lifetime, whereas an internal pressure buildup occurs in the sealed-can LMFBR designs.

Information from the LMFBR and other programs that would be ideal for the GCFR would be a completely rational basis for design of the fuel rod. Since this ideal is unlikely to be realized on a practical time scale, a more empirical approach is necessary. This approach consists of:

1. Analyzing as many test results as possible where the parameters are in the range of interest for the GCFR

2. Endeavoring to construct rational bases for interpolating or extrapolating the observed results to GCFR conditions.

Specifically, the items of particular interest include:

1. General behavior of oxide fuels
2. General behavior of cladding materials in fast-flux tests and information on the behavior mechanisms
3. Establishment of failure criteria
4. Effects on fuel-rod swelling at GCFR conditions of:
   a. Fuel-cladding gap
   b. Burnup
   c. Fuel density
   d. Fuel composition
   e. Fabrication method
   f. Linear heat generation rate
   g. Cladding temperature
5. Dependence of fuel-rod failure on:
   a. Cladding temperature
   b. Cladding strain
   c. Cladding material
   d. Burnup
   e. Cladding fast neutron nvt.
6. Contribution to total fuel-rod swelling of:
   a. Internal gas pressure
   b. Fuel swelling
   c. Cladding swelling
7. Information on fuel-rod behavior under cyclic pressure and temperature conditions
8. Information on fuel-rod bundles where the rods are subjected to external constraints, such as spacers and holders
9. Fuel-rod behavior under nuclear transients and loss-of-coolant excursions

Experimental knowledge of these items would contribute toward a rational basis for designing GCFR fuel elements.

4.1.1. Thermal Versus Fast-Flux Testing and Interpretation of Results

Facilities for testing fuel elements in a fast-neutron flux are very limited and data have been obtained only in unpressurized fuel-rod environments and with fuel rods operating at cladding OD surface temperatures less than or equal to 650 C. Thermal reactor irradiations at design cladding temperatures are more readily available and do provide for the use of instrumentation, but application of the results to GCFR has specific limitations. The high-fission cross section of the plutonium and enriched uranium causes self-shielding, which leads to nonuniform heat generation within the fuel, especially during the early life of the fuel. This is accompanied by a preferential burnup at the fuel periphery and an atypical temperature gradient across the fuel. The results of self-shielding also cause differences in fuel swelling rates (Ref. 1) and the distribution of the fission products. Another important difference is that the fast-neutron damage (embrittlement and swelling) to the cladding cannot be duplicated. A tentative model has been developed to interpret some aspects of thermal-flux tests of fast-reactor fuel rods (Ref. 2).

4.1.2. Fast-Flux Tests

Insofar as it was possible, the fast-flux irradiation data selected were from those experiments in which the cladding surface temperatures and the linear heat-generation ratings in the fuel rods were in the range of GCFR operating conditions. Although the data have some value in guiding the GCFR program, there are limitations, as follows:

1. The maximum cladding surface temperatures in LMFBR fuel-rod irradiation tests are generally well below the GCFR maximums (less than 600 C as compared with 700 C to 800 C for GCFR)

and even below the LMFBR maximums (650 C to 700 C). Further, since the fast-flux tests have all been uninstrumented, there is a considerable amount of uncertainty in the accuracy of the temperatures reported.

2. The combination of the desired burnups (ranging from 50,000 to 100,000 MDd/Te) coupled with the required cladding exposures (approximately 1×10^{23} to 3×10^{23} nvt) has never been achieved simultaneously in any of the LMFBR fuel-rod irradiation tests. This combination of exposures in fuel-rod proof tests is required for both the GCFR and the LMFBR fuel-rod development programs before a reliable fuel-rod design can be assured.

3. Few, if any, LMFBR fuel-rod irradiation tests have included the fuel-cladding interface time-temperature history required to simulate actual GCFR or LMFBR conditions that would reveal the extent of fuel-cladding chemical interactions.

Table 4.1 lists the experiments from which data were selected. The experiments are primarily single-rod tests performed in the Experimental Breeder Reactor-II (EBR-II) and the Dounreay Fast Reactor (DFR), but some data from 77-rod bundle tests performed in DFR are also included. Insofar as was possible, a distinction was made between the rod behavior in fueled regions and in plenum and blanket regions.

4.1.3. Thermal Fast-Flux Tests

Even though thermal-flux tests have limited value for developing fast-reactor fuel rods because cladding embrittlement and swelling effects and fuel thermal gradients and burnup effects cannot be adequately simulated, there is some valuable information to be gained from the results of the key thermal-flux test data selected for this report:

Table 4.1

FAST-FLUX IRRADIATION TEST RESULTS

Code No.	Test Identification	Test Reactor and Position	Total[a] Fluence Status/ Goal	Fuel-rod Type	Fuel-Cladding Thermal Bond	Fuel						Cladding			Normalized Conditions				Significant Features or Results					
						Composition	%T.D.	%S.D.	Geometry	Stoichiometry	Fuel Cladding Gap (in.)	Composition	Thickness/ OD (in.)	Pretreatment	Heat Rating (kW/ft)	Max. Clad. OD Temp. (C)	Max. Fuel Temp. (C)	Heavy Metal Burnup (atom-%)	ΔD(in.)	ΔD/D%	ΔL	ΔV%	% F.G. Rel.	Condition
	UK ATOMIC ENERGY AUTHORITY																							
1	77-rod Mk I assembly	DFR	~1x10[22] nvt in cladding	Sealed can	He	85% UO_2 15% PuO_2		75-82	V and P, A[b]	NA[c]	0.002, 0.007 for P,A	M316	0.015/ 0.230	ST[d] and CW[e]	~10	545		4.8 - 5.5 (peak)	0.0017 P,A; 0.002 V	Nil to ~1% for P,A; nil to ~1.5 for V	0.33% St			No failures in subassembly. Lower strain in CW rods is evidence that CW reduces rod swelling
																			0.009 V; CW		0.06% St,			
2	Mk IB					75% UO_2			V and P,A			M316				575		6.1 - 7.0 (peak)	0.003 P,A;St		0.24% CW			
2a	Mk II					25% PuO_2			V and P,A			M316				615		6.4 - 7.3 (peak)	0.002 V,P,A; CW		0.27% CW			
3	V.166					85% UO_2 15% PuO_2		85.3	V			316[f]	0.015/ 0.230	CW	10.6	640		5.8		0.65	0.1	1.425		Intact
4	V.162							84.7	V			316L		CW	13.2	610		5.1		0.3	0.157	0.758		Intact
5	V.162R													CW	12.8	580		7.1		0.63	0.242	1.508	71	Intact
6	V.035							82.3						ST	9.83	590		5.2		0.39	0.05	0.831		Intact
7	V.037							82.5						ST	9.67	536		6.9		0.52	0.18	1.224		Intact
8	V.039							82.6						CW	10.15	590		5.7		0.42	0.14	0.982		Intact
9	V.039R							82.6						CW	10.0	600		7.5		0.76	0.17	1.698	81	Intact
10	V.173							82.1						ST	10.2	570		6.7		0.6	0.07	1.274		Intact
11	A.151							72.4	P,A					CW	9.88	540		5.8		0.14	0.035	0.315		Intact
12	A.151R							72.4						CW	9.44	600		7.7		0.5	0.046	1.048	44	Intact
13	A.153							72.9						CW	11.1	580		7.0		1.3	0.025	2.642		Intact
14	V.177							83.2	V			Nim. 80A		FHT[g]	9.36	625		2.9		0.25	0.05	0.55		Intact
15	V.177R							83.2				Nim. 80A		CW	9.25	620		5.8		0.25		0.50		Intact
16	V.233							83.3				316L		CW	12.88	540		6.0		0.56	0.014	1.137		Intact
17	V.259							79.3						CW	12.1	400		6.0		0.65	0.05	1.355	78	Intact
18	V.258							81.6					0.025/ 0.325	CW	23.4	580		6.0		0.85	0.14	1.849	92	Intact

TABLE 4.1 (continued)

Code No.	Test Identification	Test Reactor and Position	Total[a] Fluence Status/ Goal	Fuel-rod Type	Fuel Cladding Thermal Bond	Fuel: Composition	Fuel: % T.D.	Fuel: % S.D.	Fuel: Geometry	Fuel: Stoichiometry	Fuel: Fuel Cladding Gap (in.)	Cladding: Composition	Cladding: Thickness/ OD (in.)	Cladding: Pretreatment	Normalized Conditions: Heat Rating (kW/ft)	Normalized Conditions: Max. Clad. OD Temp (C)	Normalized Conditions: Max. Fuel Temp. (C)	Normalized Conditions: Heavy Metal Burnup (atom-%)	Significant Features or Results: ΔD(in.)	Significant Features or Results: ΔD/D%	Significant Features or Results: ΔL	Significant Features or Results: ΔV%	Significant Features or Results: % F.G. Rel.	Condition
UK ATOMIC ENERGY AUTHORITY (continued)																								
19	V.024	DFR		Sealed can	He	85% UO_2 15% PuO_2		79.3	V	NA[c]	0.002, 0.007 for P,A	316L	0.015/ 0.230	ST	9.2	680		7.1		1.0	1.4	3.438	36	Failed
20	V.021	↓		↓	↓	↓		81.7	V	↓	↓	↓	↓	ST	11.7	625		8.1		1.7	1.14	4.607	45	Failed
21	V.035R							82.3	V					ST	9.55	600		6.9		0.7	0.025	1.429	76/ 85	Failed
22	A.153R							72.9	P,A					CW	10.77	600		9.1		1.7	0.02	3.448		Failed
GENERAL ELECTRIC																								
23	F2F	EBR-II 4E2 XG06 MKA	$4.2x10^{22}$	Sealed can	He	$(U-20Pu)O_2$	96.7	94.8	P	1.98	0.003	Inc. 800	0.015/ 0.250	ST	16.1	540	2200	6.3	0.053		NA		50	Failed
24	F2G	EBR-II 4C2 XG05 MKA	$5.5x10^{22}$	↓	↓	↓	95.5	92.9	P	2.00	0.002 - 0.006	347SS	↓	↓	16.4	540	↓	7.6	Irradiation continuing					
25	F2H	EBR-II 4C2 XG05 MKA	$5.5x10^{22}$				96.1	94.9	P	1.98	0.002 - 0.006	316SS			16.4	540		7.9	0.002	0.92	0.442%			
26	F2N	EBR-II 4E2 XG06 MKA	$4.2x10^{22}$/ $9x10^{22}$				96.3	92.6	P	2.00	0.0034	347SS	0.010/ 0.250		16.1	600		5.8	0.0022	0.88	0.028 in.	2.571	50	Good
27	F2O	EBR-II 4C2 XG05 MKA	$5.5x10^{22}$				95.7	94.0		2.03	0.0018 - 0.0045				17.2	540		7.6	Failed cracked from one end to the other				51	Failed
28	F2P	EBR-II 4E2 XG06 MKA	$4.2x10^{22}$				95.5	94.5	P	2.00	0.0030				11.7	500		3.6	0.0013	0.52	0.029	1.868	32	Good
29	F2Q	EBR-II 4E2 XG06 MKA	$4.2x10^{22}$				96.2	96.7	P	2.00	0.0012				15.8	590	2200	6.0	0.0023	0.92	0.032	2.767	47	Good
30	F2R	EBR-II 4C2 XG05 MKA	$5.5x10^{22}$				95.3	95.2	P	2.00	0.001 - 0.002				15.8	590		7.6	0.0044	1.12	0.519%			
31	F2S	EBR-II 4E2 XG06 MKA	$4.2x10^{22}$				97.1	96.7	P	2.00	0.0012		0.030/ 0.250		16.4	570		6.3	0.0043	1.715	0.014	3.868	55	Good
32	F2T	EBR-II 4C2 XG05 MKA	$5.5x10^{22}$				96.1	94.6		2.00	0.001 - 0.006		0.015/ 0.250		16.4	620		7.9	0.0043	1.1	0.533%			
33	F2U	EBR-II 4E2 XG06 MKA	$4.2x10^{22}$				89.6	87.0	P	1.98	0.0034				16.3	580		5.9	0.001	0.4	0.017 in.	1.2848	63	Good
34	F2V	EBR-II 4C2 XG05 MKA	$5.5x10^{22}$				89.5	86.8	P	1.99	0.002 - 0.006	316SS			16.3	580		7.5	Irradiation continuing					
35	F2W	EBR-II 4E2 XG06 MKA	$4.2x10^{22}$	↓	↓	↓	NA	83.8	V	1.99		347SS	↓	↓	15.8	570	↓	5.1	0.0011	0.44	0.013 in.	1.251	58	Good

TABLE 4.1 (continued)

Code No.	Test Identification	Test Reactor and Position	Total[a] Fluence Status/ Goal	Fuel-rod Type	Fuel Cladding Thermal Bond	Fuel: Composition	Fuel: % T.D.	Fuel: % S.D.	Fuel: Geometry	Fuel: Stoichiometry	Fuel: Cladding Gap (in.)	Cladding: Composition	Cladding: Thickness/ OD (in.)	Cladding: Pretreatment	Normalized Conditions: Heat Rating (kW/ft)	Normalized Conditions: Max. Clad. OD Temp (C)	Normalized Conditions: Max. Fuel Temp. (C)	Normalized Conditions: Heavy Metal Burnup (atom-%)	Significant Features or Results: ΔD(in.)	ΔD/D%	ΔL	ΔV%	% F.G. Rel.	Condition
GENERAL ELECTRIC (continued)																								
36	F2X	EBR-II 4C2 XG05 MKA	5.5×10^{22}	Sealed can	He	$(U\text{-}20Pu)O_2$	NA	84.0	P	1.99	0.002 - 0.006	316SS	0.015/ 0.250	ST	14.1	570		7.5		Irradiation continuing				
37	F2Y	EBR-II 4E2 XG06 MKA	4.2×10^{22}				NA	83.9	V	1.99					14.1	550		5.0	0.001	0.4	0.006 in.	0.971	56	Good
38	F2Z	EBR-II 4E2 XG06 MKA	4.2×10^{22}				89.3	87.2	P	1.99	0.0029				14.4	580		5.8	0.0016	0.64	0.011 in.	1.016	58	Good
42	F4D	EBR-II 2F1 XO11 MKA	3.1×10^{22}				89.2	86.8	P	2.00		Inc. 800			17.20	550		3.7	0.0008	0.3%	0.8%		52	Failed
43	F4E	EBR-II 2F1 XO11 MKA	3.1×10^{22}				89.9	87.3				316			18.21	550		3.7						
44	F4F	EBR-II 2F1 XO11 MKA	3.1×10^{22}				89.3	86.3	P	2.00		Inc. 800			18.21	550		3.7	NA		0.8%		NA	Failed
45	F0A	EBR-II 7D1 XG03 MKA	3.6×10^{22}/ 4.1×10^{22}			$(U,Pu)O_2$	95.7	93.2	P		0.002	347SS			6	650	1500	5.4		No PIE Report				
46	F0B	EBR-II 7B1 XG04 MKA	3.6×10^{22}/ 8.8×10^{22}				94.1	92.5			0.001				6	650	1500	10.8 goal		Irradiation continuing				
47	F0C	EBR-II 7D1 XG03 MKA	3.6×10^{22}/ 4.2×10^{22}				94.2	93.7			0.002				6	650	1500	5.4		No PIE Report				
48	F0D	EBR-II 7B1 XG04 MKA	3.6×10^{22}/ 8.8×10^{22}				95.9	93.2			0.004				6	650	1500	10.8 goal		Irradiation continuing				
49	F0E	EBR-II 7A1 XG02 MKA	2.9×10^{22}				97.1	93.6			0.002				6	650	1500	5.4		No PIE Report				
56	F2A	EBR-II 4E2 XG06 MKA	4.2×10^{22}/ 9×10^{22}				95.5	94.0		2.00	0.0025				15.5	550	2200	5.8	0.0014	0.56	-0.033	2.063	49	Good
57	F2B	EBR-II 4E2 XG06 MKA	4.2×10^{22}/ 9×10^{22}				96.0	94.6			0.0026	316SS			15.5	580	2200	6.0	0.0017	0.68	+0.026	2.106	48	Good
58	F2C	EBR-II 4C2 XG05 MKA	5.5×10^{22}/ 6×10^{22}				94.7	93.1			0.002 - 0.005	Inc.			16.1	580	2200	7.6	0.002	0.51				Good
59	F2D	EBR-II 4C2 XG05 MKA	5.5×10^{22}/ 6×10^{22}				96.5	94.9			0.002 - 0.006	347SS			16.1	580	2200	7.8		Irradiation continuing				
60	F2E	EBR-II 4E2 XG06 MKA	4.2×10^{22}/ 9×10^{22}				96.5	94.4			0.0032	316SS			15.8	530	2200	6.1	0.0021	0.84	+0.022	2.319	50	Good

TABLE 4.1 (continued)

Code No.	Test Identification	Test Reactor and Position	Total[a] Fluence Status/ Goal	Fuel-rod Type	Fuel Cladding Thermal Bond	Fuel						Cladding			Normalized Conditions				Significant Features or Results					
						Composition	% T.D.	% S.D.	Geometry	Stoichiometry	Fuel Cladding Gap (in.)	Composition	Thickness/ OD (in.)	Pretreatment	Heat Rating (kW/ft)	Max. Clad. OD Temp (C)	Max. Fuel Temp. (C)	Heavy Metal Burnup (atom %)	ΔD(in.)	ΔD/D%	ΔL	ΔV%	% F.G. Rel.	Condition
						NUMEC																		
A-1	A-1	EBR-II 4C3 X017	3.4×10^{22}	Sealed can	He	UO_2	89.71	86.85	P	1.989	0.002 - 0.0022	316L	0.015/ 0.250		12-14	550		4.4	0.00137	0.54				Intact
A-2	A-2	↓	↓	↓	↓	$(U\text{-}20Pu)O_2$	90.19	88.99	↓	2.000	0.00095 - 0.00225	↓	0.030/ 0.250	↓	↓	↓	↓	↓	0.00142	0.50	↓	↓	↓	Intact
A-3	A-3	↓	↓	↓	↓	↓	90.31	87.60	↓	1.974	0.00185 - 0.00215	↓	0.015/ 0.250	↓	↓	↓	↓	↓	0.00157	0.62	↓	↓	↓	Intact
A-4	A-4	↓	↓	↓	↓	↓	82.75	80.51	↓	1.956	0.0018 - 0.002	↓	↓	↓	↓	↓	↓	↓	0.00132	0.52	↓	↓	↓	Intact
A-5	A-5	↓	↓	↓	↓	↓	90.12	87.59	↓	1.989	0.00175 - 0.00205	↓	↓	↓	↓	↓	↓	↓	0.00201	0.79	↓	↓	↓	Intact
A-6	A-6	↓	↓	↓	↓	↓	88.29	87.33	↓	↓	0.0011	↓	↓	↓	↓	↓	↓	↓	0.00144	0.57	↓	↓	↓	Intact
A-7	A-7	↓	↓	↓	↓	↓	83.99	81.64	↓	1.992	0.0011 - 0.00205	↓	↓	↓	↓	↓	↓	↓	0.00139	0.55	↓	↓	↓	Intact
A-8	A-8	↓	↓	↓	↓	↓	83.55	80.99	↓	1.998	0.0011 - 0.0022	↓	↓	↓	↓	↓	↓	↓	0.00209	0.82	↓	↓	↓	Intact
A-9	A-9	↓	↓	↓	↓	↓	89.59	87.16	↓	2.000	0.00105 - 0.002	Hast. X	↓	↓	↓	↓	↓	↓	0.00072	0.29	↓	↓	↓	Intact
A-10	A-10	↓	↓	↓	↓	↓	82.38	79.93	↓	1.940	0.002 - 0.00215	316L	↓	↓	↓	↓	↓	↓	0.00139	0.55	↓	↓	↓	Intact
A-11	A-11	↓	↓	↓	↓	↓	89.90	87.30	↓	1.974	0.0021	316L	↓	↓	↓	↓	↓	↓	0.00149	0.59	↓	↓	↓	Intact

TABLE 4.1 (continued)

Code No.	Test Identification	Test Reactor and Position	Total[a] Fluence Status/ Goal	Fuel-rod Type	Fuel Cladding Thermal Bond	Fuel: Composition	Fuel: % T.D.	Fuel: % S.D	Fuel: Geometry	Fuel: Stoichiometry	Fuel: Cladding Gap (in.)	Cladding: Composition	Cladding: Thickness/ OD (in.)	Cladding: Pretreatment	Normalized Conditions: Heat Rating (kW/ft)	Normalized Conditions: Max. Clad. OD Temp (C)	Normalized Conditions: Max. Fuel Temp. (C)	Normalized Conditions: Heavy Metal Burnup (atom %)	Significant Features or Results: ΔD(in.)	Significant Features or Results: ΔD/D%	Significant Features or Results: ΔL	Significant Features or Results: ΔV%	Significant Features or Results: % F.G. Rel.	Condition
ARGONNE NATIONAL LABORATORY																								
-3	SOV-3	EBR-II 2F1 X011 MKA	~2.3×10^{22}/ 3.5×10^{22}	Sealed can	He	$(U\text{-}20Pu)O_2$		83.1	V	2.00		304SS	0.021/ 0.296		21.4	540		3.7	0.0012	0.4				Intact
-7	SOV-7							85.1				304SS	0.021/ 0.296		21.3	540		3.6	0.0012	0.4			61	Intact
-10	HOV-10							84.8				Hast-X	0.016/ 0.296		22.8	550		3.5		0.8				Failed
-15	HOV-15							79.8				Hast-X	0.016/ 0.296		21.4	550		3.5	0.0008	0.27			82	Intact
-4	HOV-4							80.0				Hast-X	0.016/ 0.0296		22.9	550		3.6						Failed

(a) Fractions of fluence in EBR-II with energies >0.111 MeV are 0.94 for row 2, 0.73 for row 4, and 0.33 for row 7.

(b) V = Vibrationally compacted;
P,A = Pellet, Annular.

(c) NA = Not available.

(d) ST = Solution-treated, 20 min 1050 C.

(e) CW = Cold worked, 20% or 30%.

(f) 316L = Slightly modified.

(g) FHT = Fully heat-treated ST 1080 deg 3 min, + 700 deg 16 hr.

1. Several thermal irradiations have been exposed to high burnups (up to 148,000 MWd/Te) where fuel swelling effects (though different from those in a fast flux) are known to be significant.

2. Instrumented tests have been performed in which the temperatures and pressures and fission-product releases have actually been measured, rather than calculated as in the fast-flux tests. (Some instrumented tests have been performed in the DFR but none in fast-reactor tests in the United States.)

3. Programmed cyclic conditions of power and pressure have been imposed on some thermal-flux tests, whereas no such fast-flux test results are as yet available.

4. Screening-type tests, such as fuel-cladding compatibility studies or fuel-rod concept studies, can be performed under conditions where the temperatures and pressures can be measured.

5. The detrimental effects of thermal aging on cladding properties can, to a fair degree, be differentiated from the detrimental effects of high exposure to fast-neutron.

6. Operating experience in the Advanced Gas Cooled Reactor (AGR) is of interest to the GCFR program because fuel-rod cladding temperatures are similar and surface roughening is employed to improve heat transfer in the gas coolant. Further, the collapsing stress on the cladding of sealed-rod designs is comparable in the two reactor systems.

Table 4.2 shows the results of tests of the experiments from which data were selected.

4.2. CREEP BEHAVIOR OF OXIDE FUELS

To rationally design fuel elements for fast reactors, a thorough knowledge of the creep behavior of the fuel material under service

Table 4.2

THERMAL-FLUX IRRADIATION TEST RESULTS

Code No.	Test Identification	Test Reactor and Position	Time of Irrad. (hr)	Fuel-rod Type	Fuel-Cladding Thermal Bond	Fuel: Composition	Fuel: % T.D.	Fuel: % S.D.	Fuel: Geometry	Fuel: Stoichiometry	Fuel: Fuel Cladding Gap (in.)	Cladding: Composition	Cladding: Thickness/OD (in.)	Cladding: Pretreatment	Normalized Conditions: Heat Rating (kW/ft)	Normalized Conditions: Max. Clad. OD Temp (C)	Normalized Conditions: Max. Fuel Temp. (C)	Normalized Conditions: Heavy Metal Burnup (atom %)	Significant Features or Results: ΔD (in.)	ΔD/D%	ΔL	ΔV%	Final D Gap (in.)	% F.G. Rel	Condition
GENERAL ELECTRIC																									
65	E-1-E-1	Hyd.Rabbit	NA[a]	Sealed can	He	UO 20 PuO_2	94.7	94.7	P[b]	2.00		347	0.015/ 0.218	ST[c]	20	345		9.3	<0.0002	0.09	4.4	4.567			
66	E-1-F-1						94.7	94.6	P	2.00					20/28	345		8.5	<0.0002	0.9	4.2	4.367			
67	E-2-C-1	V Raft					85	85	P	2.00	0.0032				25	570		12.8	<0.0002	0.9	6.1	6.269	0	85	Good
68	E-2-C-2						95	95	P	2.00	0.0037				25	570		12.87	<0.0002	0.9	8.0	8.173	0	83	Good
69	E-2-D-1					UO 25 PuO_2	90	87.5	P	2.00	0.0024/ 0.0029	316	0.014/ 0.182		17/25	565	2250	13.7	<0.0005	0.27	8.3	8.473	0.001	76/86	Good
70	E-2-D-2						92	88.3	P	1.96	0.0022/ 0.0035		0.014/ 0.182		17/25	565		14.3	<0.0005	0.27	4.5	4.667	0.001	82/91	Good
75	E-2-J						96/90	88	P and P,A	1.98			0.218		25	595		13.55	0.0011/ 0.0012	0.44/ 0.48		Annular pellets solid pellets			
77	E-5-B-1	Std.Pool position					86	84	P	2.00	0.0032/ 0.0037	347	0.015/ 0.250		23.5	685		14.5		1.2	4.7	4.867	0		Fuel–cladding chemical interaction
78	E-5-B-2						84	84	V	1.999			0.015/ 0.250		23.5	685		14.5		0.7	3.0	3.165	0		Interaction to depth of 0.002/0.003 in.
OAK RIDGE NATIONAL LABORATORY																	Pressure (psi)		Mode of Failure						Cause of Failure
79	E1A	ETR	5500	Sealed can	He	UO_2	94.0		P	2.002	0.006 Nominally	304SS	0.020/ 0.751	ST	16.4[d]	700	300	0.55	Axial fracture						Impure fuel and overpower operation
80	E4		10,000				93.8		P	2.002					17[d]	700		0.87	Axial fracture						Same as above
81	E6		12,140				94.8		P,A	2.038					15.2[d]	700		1.1	Did not fail						- - - - - - - - - - -
82	E8		12,550				94.6			2.027					12.9[d]	870		1.1	Circumferential fracture						Impure fuel and overpower operation
83	01C-4	ORR	4130				96.0			2.003					8.8	870		1.4	Cladding depression						Chipped fuel pellet
84	0884		4130				95.6			<2.002					8.8	870		1.7	Cladding depression						Groove in fuel pellets

TABLE 4.2 (continued)

Code No.	Test Identification	Test Reactor and Position	Time of Irrad. (hr)	Fuel-rod Type	Fuel-Cladding Thermal Bond	Fuel						Cladding			Normalized Conditions				Significant Features or Results	
						Composition	% T.D.	% S.D.	Geometry	Stoichiometry	Fuel Cladding Gap (in.)	Composition	Thickness/ OD (in.)	Pretreatment	Heat Rating (kW/ft)	Max. Clad OD Temp (C)	Pressure (psi)	Heavy Metal Burnup (atom %)	Mode of Failure	Cause of Failure
OAK RIDGE NATIONAL LABORATORY (continued)																				
85	02-5	ORR	4050	Sealed can	He	UO_2	96.0		P,A	2.002	0.006 nominally	304SS	0.020/ 0.751	ST	8.8	870		1.8	Capillary tube fracture	Faulty tube weld
86	07-5	↓	4050		↓	↓	95.9		↓	2.002	↓	↓	↓	↓	8.8	870		1.7	Cladding depression	Fracture and collapse of pellet
GULF GENERAL ATOMIC																				
87	P4A1-1 GA-1	ORR-P4	650	Sealed can	He	UO_2	~90	< 85	P,A	2.005	0.0018	Hast.-X	0.0091/ 0.379	ST	18/ 21.7	760/ 810	Max. Fuel Temp. (C)		Significant Features or Results	
88	P4A1-2 GA-2		650				~90			2.005	0.0028		0.0092/ 0.378		18/ 21.7	760/ 810		0.41	Specimens collapsed, negligible fuel support	
89	P4B1-1 GA-4		800				~90			2.006	0.001/ 0.0025		0.014/ 0.342		18/ 16.2	760-785/ 680			Good condition; collapse in region of thin cladding, negligible fuel support	
90	P4B2-2 GA-5		800	Sealed can tapered cladding			~90			2.006	0.0008/ 0.0023		0.010 - 0.020/ 0.334 - 0.352		18/ 16.2	760-720/ 680		0.55		
91	P4B3-1 GA-6		1340	Flex can	Na		~95		P	2.005	0.017	304SS	0.010/ 0.375		14.7	660		0.68	Slight creep deformation	
92	P4B3-2 GA-7		1340	Sealed can	He		~90		P,A	2.003	0.0036	Hast.-X	0.015/ 0.343		12.1	660		0.69		
93	P4B4-1 GA-8		2000	Flex can	Na		~95		P	2.0032	0.015	304SS	0.010/ 0.375		13.5/ 15.1	705/ 755		1.01	Good collapse stability	
94	P4B4-2 GA-9		2000	Sealed can,PP	He		~90		P	2.0032	0.0036	Hast.-X	0.015/ 0.343		11.4 12.6	650/ 720		1.07		
95	04P5-1 GA-10	ORR-04	2200	Sealed can,PP					P,A	2.0039	0.0035	Hast.-X partially			14.0	710		1.34	Some cladding deformation under thermocouple used to monitor cladding O.D. temperature	
96	04P5-2 GA-11		2200	Sealed can,PP						2.002	0.0035	Surface roughened			16.2	812		1.46	Good collapse stability	
97	04P6-1 GA-12		1100	Sealed can		$88UO_2$-12 PuO_2				1.98/ 1.99	0.0033				15	710		0.67	Good collapse stability	

TABLE 4.2 (continued)

Code No.	Test Identification	Test Reactor and Position	Time of Irrad. (hr)	Fuel-rod Type	Fuel Cladding Thermal Bond	Fuel: Composition	Fuel: % T.D.	Fuel: % S.D.	Fuel: Geometry	Fuel: Stoichiometry	Fuel: Fuel Cladding Gap (in.)	Cladding: Composition	Cladding: Thickness/OD (in.)	Cladding: Pretreatment	Normalized Conditions: Heat Rating (kW/ft)	Normalized Conditions: Max. Clad. OD Temp (C)	Normalized Conditions: Max. Fuel Temp. (C)	Normalized Conditions: Heavy Metal Burnup (atom %)	Significant Features or Results
GULF GENERAL ATOMIC (continued)																			
98	04P6-2 GA-13	ORR-04	1100	Sealed can	He	$88UO_2$-12 PuO_2	~90	< 85	P,A	1.98/ 1.99	0.0033	Surface roughened	0.015/ 0.343	ST	18	812		0.71	Collapsed into oval shape, negligible fuel support; cladding failed under thermocouple band, negligible fuel support
99	04P6-3 GA-14		1100	Sealed can,PP							0.0033				18	838		0.71	
100	03P7-1 GA-15		~8800 goal	Sealed can		UO_2				2.002	0.0025	Hast.-X	0.020/ 0.353		7.4	760		2.05	Fuel rod intact
101	03P7-2 GA-16		~8800 goal			$88UO_2$-12 PuO_2				1.98/ 1.99	0.0034	Hast.-X	0.020/ 0.353		7.4	760		2.05	Fuel rod failed; fuel structure indicated overtemperature operation
102	04P8-1 GA-17		~11,000 goal				~90					316SS	0.025/ 0.357		16	610(f)		5.0	Good collapse stability, no swelling
103	04P8-2 GA-18		~11,000 goal								0.002	Hast.-X	0.015/ 0.343		16	700		6.3	Good collapse stability, no swelling
104	04P8-3 GA-19		~11,000 goal	Sealed can,PP							0.003		0.015/ 0.343		16	700		6.3	Good collapse stability, no swelling
105	GAL-1 ORR Exp 16	ORR Loop	~ 4 total	Sealed can		UO_2				2.003	0.003	Hast.-X	0.015/ 0.343		16	812		Negligible	Leak developed at location where thermocouple was attached to the cladding

(a) NA = Not available.

(b) P = Pellet,
A = Annular,
V = Vibrationally compacted.

(c) ST = Solution-treated.

(d) Design conditions were 8.8 kW/ft max, 3.8 kW/ft avg.

(e) PP = Prepressurized rod (external pressure 800 to 1000 psi in capsules, 300 psi in loop).

(f) Temperature swung from 560 C to 660 C during each reactor cycle.

conditions is necessary. Presently, knowledge of this aspect of fuel behavior is incomplete. This is partly because of the large number of variables that influence the in-pile creep of fuel materials. The pertinent variables have been classified as environmental or materials variables (Ref. 3). The environmental variables include temperature, stress, atmosphere, and fission rate. Among the variables of the materials are density, grain size and microstructure, stoichiometry, purity, U to Pu ratio, and fission-product concentrations and distributions (burnup).

Extensive studies of the out-of-pile creep of UO_2 have been performed over the last ten years, and the behavior is fairly well characterized. On the other hand, few quantitative results have yet been reported for the creep of $(U,Pu)O_2$. However, work has been initiated at Battelle-Columbus, Battelle Northwest Laboratory, and General Electric (San Jose) to obtain creep values for $(U,Pu)O_2$.

Knowledge of the influence of fission on the creep behavior of oxide fuels is in a preliminary state. Data are being reported, but it is too early to draw conclusions, except that enhancement probably occurs and the use of out-of-pile results at temperatures below about 1000 C to 1200 C may be misleading.

The state of knowledge of the creep of oxide fuel materials is reviewed and some of the work presently in progress is discussed.

4.2.1. Creep of Unirradiated UO_2

4.2.1.1. Stoichiometric UO_2. The laboratory creep data on UO_2 have recently been reviewed by Clauer, Seltzer, and Wilcox (Ref. 4). Therefore, only a brief summary will be given here. Most of the creep data on polycrystalline, stoichiometric UO_2 may be described by two distinct empirical expressions, which suggest the operation of two distinct controlling creep mechanisms. At low stresses (less than 1000 to 10,000 psi) the creep rate of polycrystalline, stoichiometric UO_2 may be described by the equation

$$\dot{\varepsilon} = A \frac{\sigma}{D^2} \exp -(Q/RT), \qquad (4.1)$$

where D is the grain size
σ is the stress
Q is the heat of activation, $\cong$90,000 cal/mole
A is a constant

This equation has the same form as that derived by Herring (Ref. 5) and Nabarro (Ref. 6) for creep by the stress directed flow of vacancies. A similar equation can be derived for creep due to grain boundary deformation.

At higher stresses the creep of polycrystalline, stoichiometric UO_2 may be described by an equation of the form

$$\dot{\varepsilon} = B \sigma^n \exp -(Q/RT), \qquad (4.2)$$

where n = 4 or 5. This type of creep equation is characteristic of a process controlled by the diffusion limited motion of dislocations (climb or nonconservative motion of jogs).

Battelle Memorial Institute-Columbus (BMI) investigators have recently presented their "agreed-on" values for the constants in Eqs. 4.1 and 4.2 (Ref. 7). The values are

$A = 8.6 \times 10^{-4}$ in.^{4}/hr-lb
Q = 87,000 cal/mole
$B = 5.13 \times 10^{-10}$ sq in./hr-lb

An analysis of the stress at which the creep mechanism changes from that described in Eq. 4.1 to that described in Eq. 4.2 has been performed (Ref. 4). It was concluded that the transition stress could be described by

$$\sigma_{tr} = cd^{-1}, \qquad (4.3)$$

where c is 2.37 lb/in. and d is the grain size. The transition stress appeared to be independent of temperature. There were significant uncertainties and inconsistencies involved in the derivation of Eq. 4.3. However, it probably represents the best available estimate of the transition stress.

4.2.1.2. Nonstoichiometric UO_2. The results described previously were obtained on stoichiometric UO_2; however, it is well established that deviations from stoichiometry have a profound influence on the creep rate of UO_2. The creep rate is enhanced by about two orders of magnitude in going from $UO_{2.0}$ to $UO_{2.15}$ (Ref. 8). The dependence of creep rate of UO_{2+x} on stoichiometry can be expressed as $\dot{\varepsilon} \propto x$, from $x = 0.02$ to 0.15. The activation energy for creep of nonstoichiometric UO_2 is 55.7 kcal/mole from $UO_{2.02}$ to $UO_{2.08}$ and 63 kcal/mole for $UO_{2.16}$. These activation energies appear to be significantly lower than those for stoichiometric UO_2.

4.2.1.3. Effects of Impurity Doping. The creep properties of UO_2 containing various impurities have been studied (Refs. 9,10). The results are of interest in assessing the influence of solid fission products on the creep behavior of oxide fuels. In general it was found that soluble impurities depressed the creep rate, perhaps by a solid-solution strengthening effect, and the insoluble inpurity (SiO_2) enhanced the creep rate. The activation energies for all of the doped specimens were somewhat higher than those for pure UO_2.

4.2.1.4. Effect of Porosity. Very little information has been reported on the effect of density on the creep of UO_2. Battelle Memorial Institute-Columbus has reported that the creep rate for densities less than 95% of theoretical is proportional to the square of the porosity (Ref. 7). This is based on very limited data and should be regarded as a tentative conclusion. No dependence of creep rate on porosity has been observed in the range 95% to 98% of theoretical density (Ref. 4).

4.2.2. Creep of $(U,Pu)O_2$

No detailed studies of the creep behavior of mixed oxides have been reported. However, work is in progress at several sites. Preliminary results reported by workers at BNWL indicate that the creep rate, at 1400 C of UO_2-25 wt-% PuO_2 at 80% of theoretical density (TD), in bending is about the same as that for UO_2 in compression (Ref. 3). The experimental value of the stress exponent was 1.6 and the activation energy was 64,000 cal/mole. These results are preliminary and should be used with caution until more work has been completed. This program has been delayed due to the difficulties encountered in fabricating dense creep specimens of the mixed oxides.

Preliminary results on creep of mixed oxides are expected at General Electric Company (San Jose)(Ref. 11), and at BMI (Ref. 12) in the near future.

4.2.3. Fission Effects on Creep

4.2.3.1. Radiation Enhancement of Creep. Enhancement of creep during fissioning was first reported for uranium by Konobeevsky, Provdyuk, and Kutaitsev (Ref. 13) in 1955. Since then the effect has been verified in several investigations (Refs. 14, 15, 16). A workable theory of radiation-enhanced creep, based on agglomeration of the point defects formed in fission spikes in such a manner as to partially relax the elastic component of the applied stress, has been presented by Hesketh (Ref. 17). Recently, enhanced creep has been reported during proton-induced fission of thorium (Ref. 18). The creep rate was independent of temperature (0 C to 200 C) and approximately proportional to the fission rate (2.7×10^{11} to 5×10^{11} f/cc-sec).

Data on the effect of fission on the creep of oxide fuels are scarce. Work on the effect of irradiation on creep of UO_2 at Harwell (Ref. 19)

and at Karlsruhe (Ref. 20) has recently been reported. The Harwell workers reported an enhancement of 10^4 in the creep of UO_2 at 1100 C due to a fission rate of 7.5×10^{12} f/cc-sec. This compares with an enhancement of 10 for UC under the same conditions. The Karlsruhe investigators considered the possible mechanisms of radiation enhanced creep and concluded that the experimental observations could be explained by the effects of fission-fragment-generated thermal spikes. Enhanced creep by increased point defect concentrations and viscous flow of amorphous regions (due to fission product segregation) were also thought to have an effect. The results of the analysis are summarized in Fig. 4.1. The data on the in-pile creep of UO_2, estimated from changes in structure and density of canned porous UO_2, fall well within the band designated "thermal spikes". The width of the band represents the range of available fission rates. It was concluded that the creep of UO_2 is strongly enhanced by irradiation below 1200 C and that the radiation creep rate is independent of temperature and directly proportional to the fission rate. It was also concluded that under fast reactor conditions the creep rate would be at least equal to the liner swelling rate due to the solid and condensed gaseous fission products.

Wilson, Walowit, and Anno (Ref. 21) have described a model for radiation-enhanced creep. In their model, complete annealing of the volume of material within thermal spikes is assumed. Thus, recovery occurs very rapidly and steady-state creep is never established. Very good agreement is reported and fitting in-pile creep results on UC to out-of-pile transient creep measurements. However, the proposed mechanism is somewhat speculative and over simplified, and the agreement may be fortuitous.

Work on in-pile creep of UO_2 and $(U,Pu)O_2$ is in progress at several sites, and more results should be available soon. Experimental difficulties involved in measuring in-pile creep are great, and the uncertainties in the data are large. Consequently, it will probably be quite some

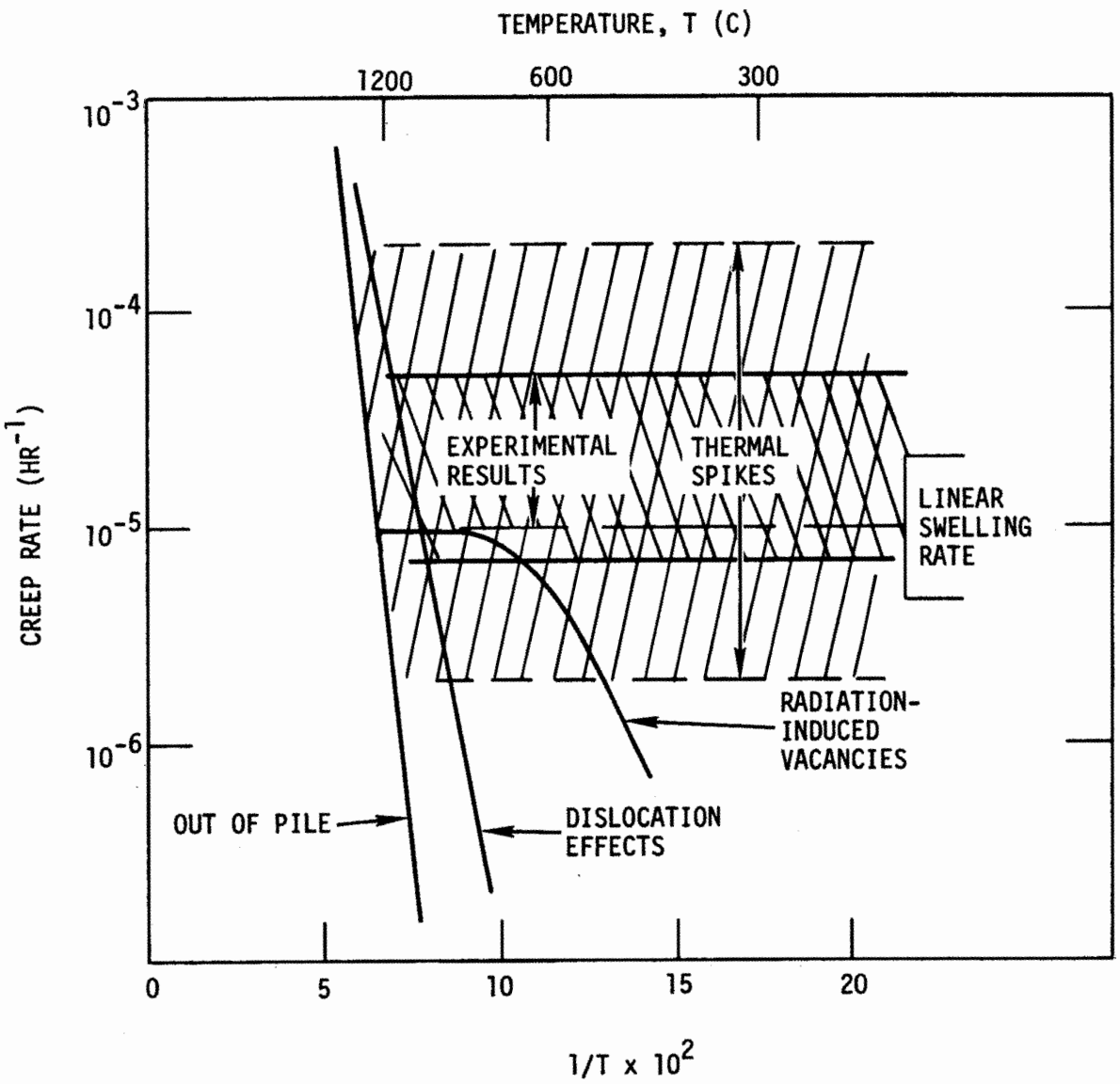

Fig. 4.1. Schematic representation of Karlsruhe work on enhanced creep (adapted from Ref. 20)

time before adequate understanding of the effects of irradiation on the creep of oxide fuels is attained. One of the most serious difficulties with in-pile creep measurement is in analyzing the effect of the large temperature gradients on the results. Bend tests on thin specimens are being performed at BNWL to minimize this problem. However, strain will not be directly read out in these experiments, and there will be considerable uncertainty in correcting for transient creep. The in-pile creep experiments in progress are at fission rates at least an order of magnitude below those that will be encountered in a fast breeder reactor. This is a serious, although necessary, shortcoming. The influence of radiation on creep is due to a complex combination of factors and it is not at all clear that extrapolation of data can be made with confidence over a wide range of experimental or service conditions.

4.2.3.2. Effect of Fission Products on Creep. Work is in progress at BMI to determine the effect of fission products on the creep behavior of UO_2 and $(U,Pu)O_2$ (Ref. 22). This study involves laboratory testing of material irradiated at low temperatures to ensure a uniform microstructure and uniform distribution of fission products. No results have been reported.

4.2.4. Summary

The creep behavior of unirradiated UO_2 is reasonably well established as a function of most pertinent variables. No reliable creep data have been reported for $(U,Pu)O_2$.

In-pile creep data on oxide fuels are scarce. However, the data that are available indicate that the creep rate below about 1000 C or 1200 C is enhanced during irradiation at fission rates near 10^{13} f/cc-sec. The dependence of in-pile creep on temperature and fission rate is not clearly established. However, there is reason to believe that the creep rate in the region where enhancement occurs will be approximately independent of temperature and strongly, perhaps linearly, dependent on

fission rate. The available evidence suggests that the use of out-of-pile creep rates in design calculations for the cool outer rim of fuel is probably invalid.

4.3. ANNEALING OF RADIATION-INDUCED SWELLING IN FAST REACTOR STRUCTURAL MATERIAL*

Stainless steel exposed to fast neutron fluences at temperatures between 300 C and 650 C will swell. The swelling becomes of practical importance (about 0.1%) at fluences of 10^{22} n/sq cm and can amount to several percent at 5 to 10 x 10^{22} n/sq cm. The swelling is caused by the formation of voids in the material. Several workers have shown that the voids can be removed by postirradiation annealing (Refs. 23-27). It is therefore conceivable that some of the engineering problems associated with the radiation-induced swelling of fast reactor structural components could be reduced by periodic annealing to recover the original dimensions. In this section, reported observations on the annealing of voids are reviewed, and estimates of the times and temperatures that might be required for such an annealing treatment are made.

4.3.1. Summary of Reported Observations

All reported work on the annealing of radiation-induced voids in stainless steel has involved 304 or 316 stainless steel irradiated in the EBR-II or the DFR at temperatures between 370 C and 540 C. Observations have been made by transmission electron microscopy, and total void volumes have been estimated from the numbers and sizes of the voids. Most postirradiation annealing treatments were for 1 hr at temperatures between 450 C and 1200 C, but one treatment was for times up to 100 hr at 700 C (Ref. 23). The reported data are given in Table 4.3. Sometimes the total void volume was not given directly but could be calculated from reported data on void sizes and distributions.

*This work was initiated under private funds and utility participation in the GCFR Program. Some of the data obtained from that work are included here because they are of interest in an overall discussion of applicable materials developments.

TABLE 4.3

SUMMARY OF REPORTED DATA ON THE ANNEALING OF RADIATION-INDUCED VOIDS IN STAINLESS STEEL

Reference Number	Material	Reactor	Radiation Temperature (C)	Fast Fluence (n/sq cm)	Postirradiation Void Diameter (A)	Annealing Time (hr)	Annealing Temp (C)	Ratio of Total Void Vol to Original Void Vol
23	304L	EBR-II	430	1.4×10^{22}	~120	1	475	1.0
						1	600	0.72
						1-100	700	(See Fig. 4.2)
						1	800	0.28
						1	900	0
			370	0.8×10^{22}	67-187	1	700	0
			472	0.9×10^{22}	<300	1	800	0
24	304L	EBR-II	421	4.8×10^{22}	~200	1	650	1.0
25	304	EBR-II	538	1.4×10^{22}	160±40	1	593	1.0
						1	648	1.0
						1	704	1.0
						1	760	1.0
						1	816	0.26
						1	871	0
26	M316L	DFR	360	6.5×10^{22}	210	1	700	1.0
						1	900	0
			500	7.8×10^{22}	1140	1	900	Grain boundary zone depleted, but large voids still present.
						1	1100	
						1	1200	

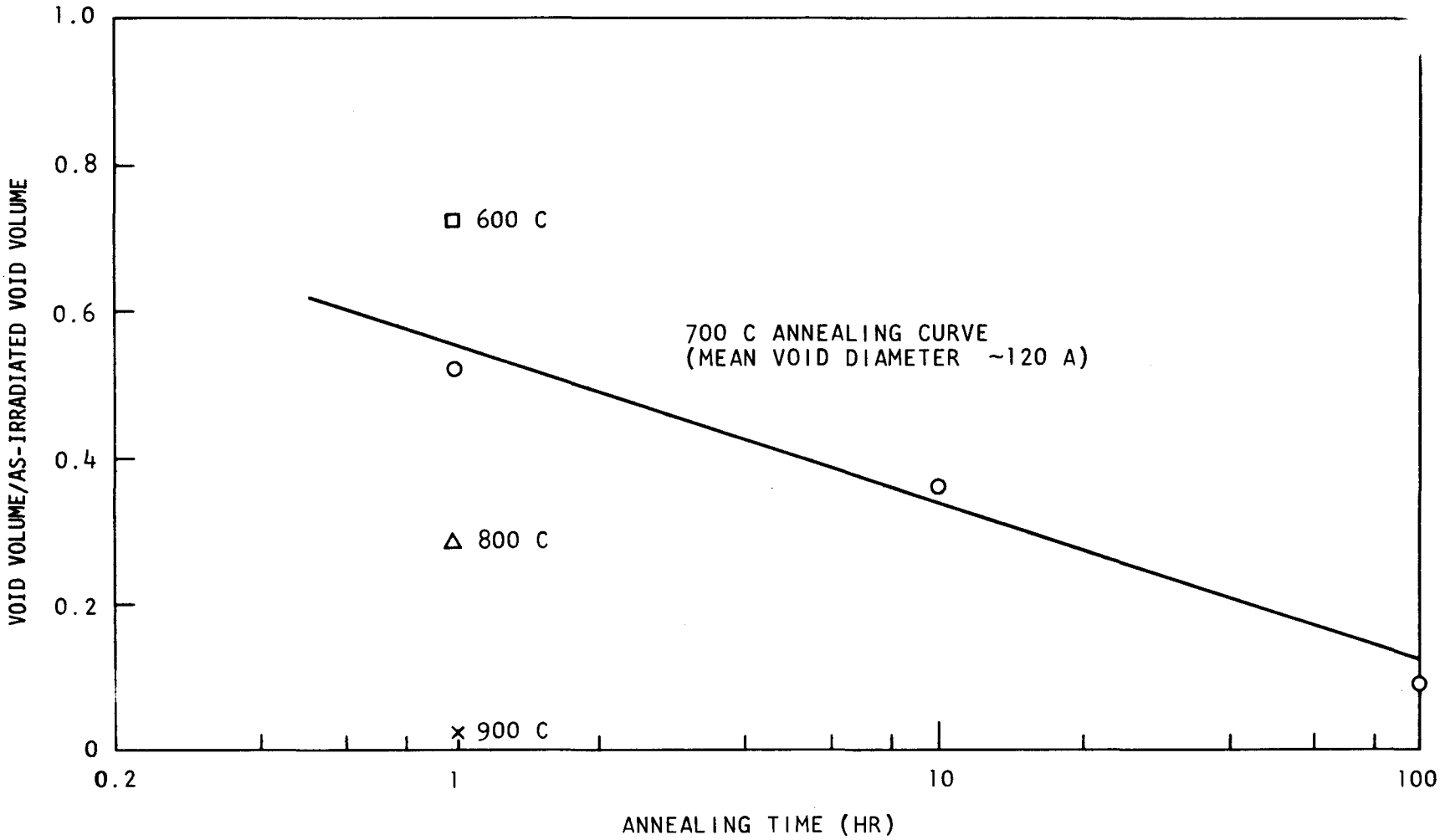

Fig. 4.2. Total void volume in type 304 stainless steel irradiated to 1.4×10^{22} n/sq cm at 430 C, as a function of annealing time at 700 C (data taken from Ref. 23)

In general, annealing reduces the void concentration, with the smaller voids disappearing first. The larger voids are removed much more slowly, and occasionally some growth of the larger voids takes place. An example of the change in void size distribution produced by annealing is given in Fig. 4.3. At the highest temperatures voids are completely removed, with the possible exception of some small pores in the grain boundaries that are attributed to residual helium.

For void diameters less than approximately 300 A, annealing is virtually complete in 1 hr at 900 C. The void volumes are plotted as a function of annealing temperature for 1 hr anneals in Fig. 4.4. The annealing behavior of one sample containing much larger voids (1100 A diameter) was quite different. Annealing to temperatures as high as 1200 C did not remove the voids, except in the vicinity of grain boundaries. Away from the grain boundaries the mean void size increased during annealing. Also, the annealing of a sample containing only small voids (maximum diameter 187 A) was completed at a significantly lower temperature (700 C) than for the bulk of the samples.

The dependence of the total void volume on the time of annealing at 700 C is shown in Fig. 4.2 for a sample containing voids in the 67 A to 300 A range. The void volume decreases approximately linearly with the logarithm of the annealing time.

4.3.2. Kinetics of Annealing

Studies of annealing of voids taking place by the migration of vacancies to sinks, such as a free surface or a grain boundary, have been performed by Volin and Balluffi (Ref. 28). Under these conditions, the diameter of all voids decreases, with small voids shrinking fastest. The total void volume decreases during annealing. The observations of the annealing of radiation-induced voids do not fit this model because coarsening of the larger voids is often observed (Refs. 23, 25, 26).

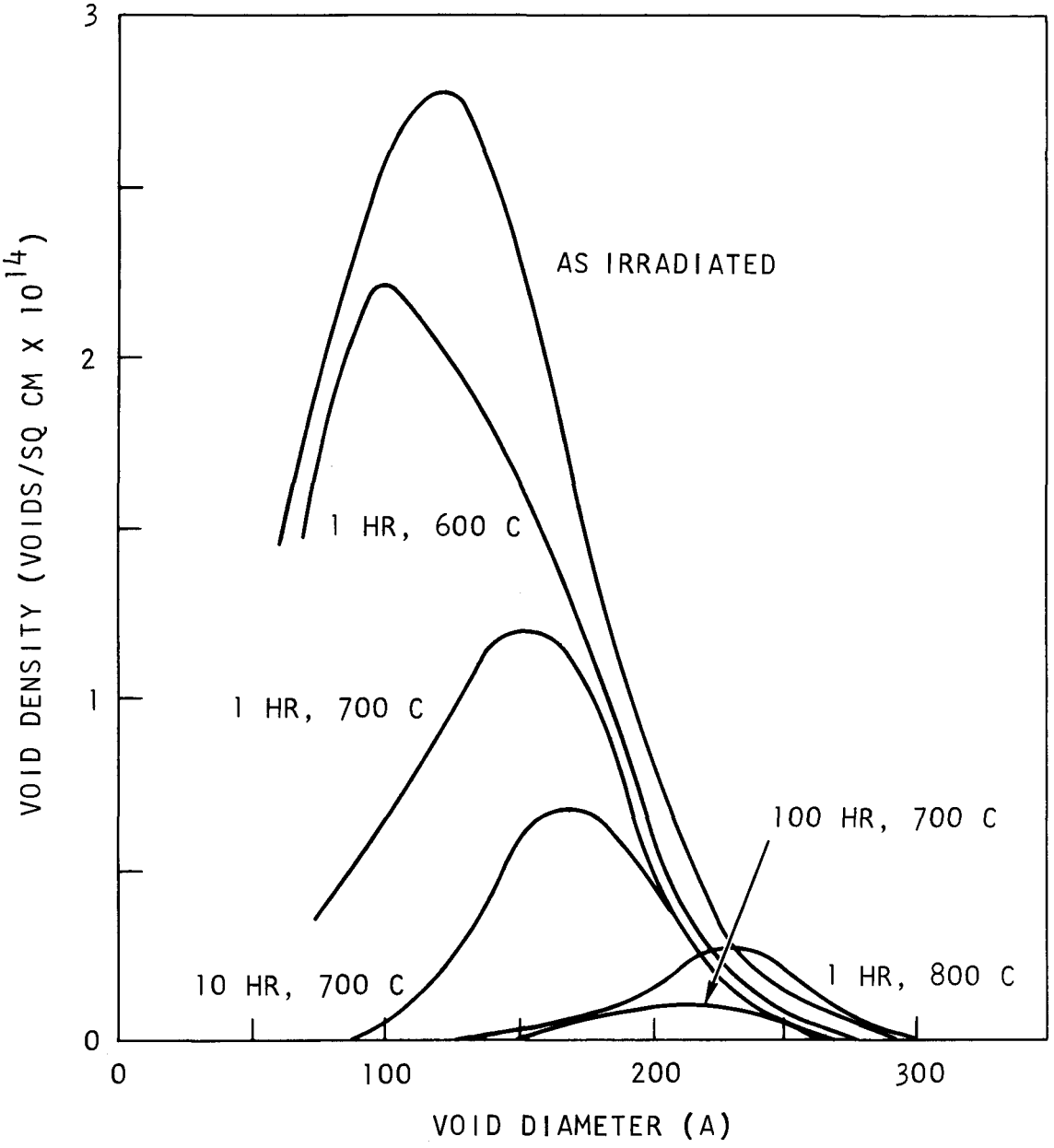

Fig. 4.3. Effect of annealing on void size distribution in 304 stainless steel irradiated to 1.4 x 10^{22} n/sq cm at 430 C (taken from Ref.23)

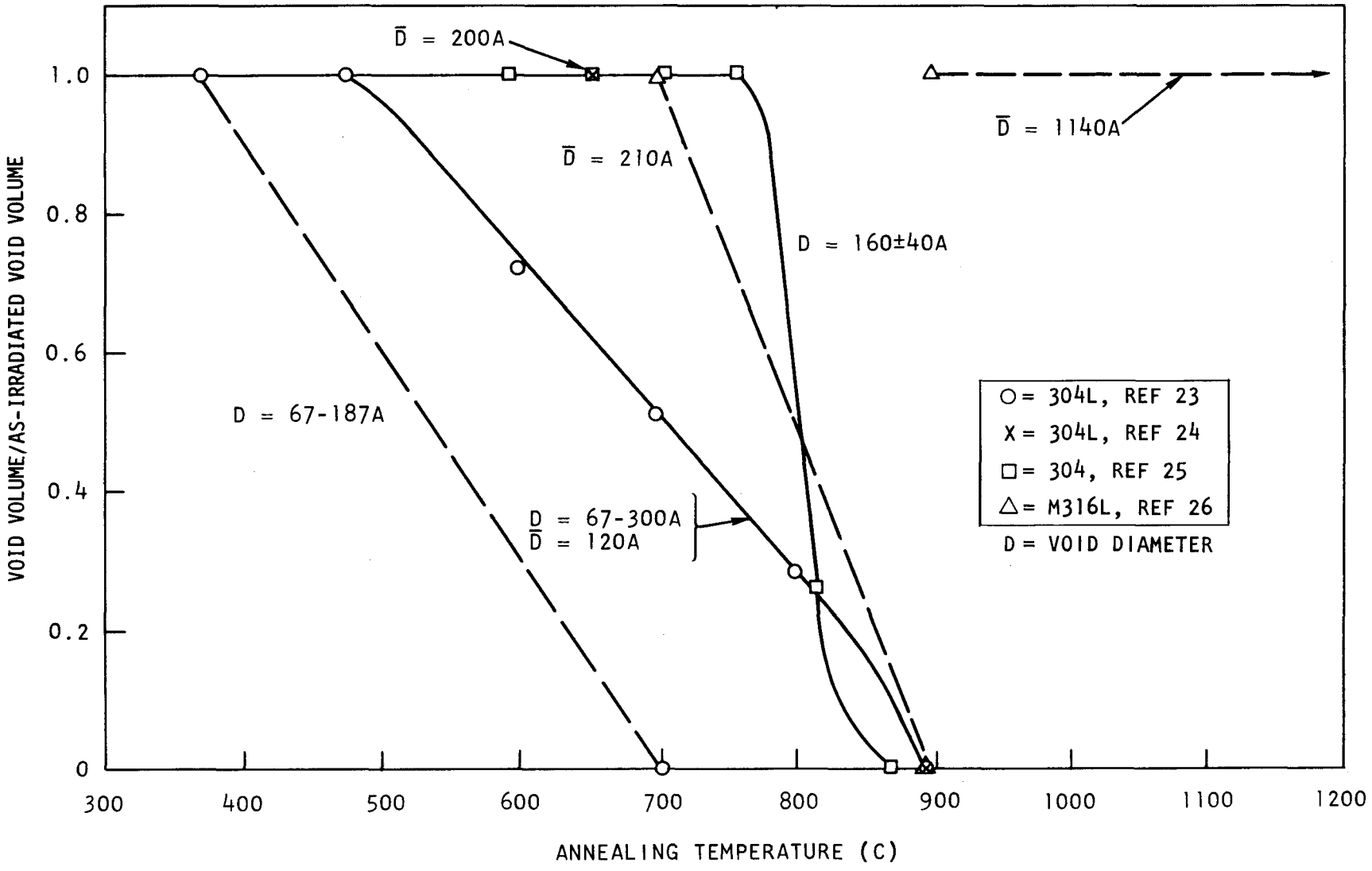

Fig. 4.4. Total void volume in irradiated and annealed types 304 and 316 stainless steel as a function of annealing temperature (annealing times = 1 hr)

A second possibility is the migration of vacancies from small voids to larger voids, causing shrinkage of the former and growth of the latter. This process is analogous to the "ripening" of precipitate particles in a two-phase alloy, which is analyzed in detail by Lifshitz and Slyozov (Ref. 29). In such a process the total volume occupied by the voids is conserved, which is inconsistent with observations, as can be seen from Fig. 4.4. Also, the distribution of void sizes predicted by this model does not fit the observed distributions. Thus, it is probable that the annealing of radiation-induced voids involves both annealing to sinks and ripening, with some voids growing at the expense of smaller voids and some vacancies being lost to grain boundaries.

Because void annealing apparently involves at least two simultaneous processes, it is not feasible to fit the data to a simple model. To make reasonable extrapolations for time and temperature dependence, the next best procedure is to use an empirical approach and scale the annealing rates according to an apparent activation energy.

For an annealing process involving a single activation energy E, the times t_1 and t_2 for an annealing-dependent property to reach the same value at temperatures T_1 and T_2 are related:

$$\ln \frac{t_1}{t_2} = \frac{E}{K} \left(\frac{1}{T_1} - \frac{1}{T_2} \right), \tag{4.4}$$

where K is Boltzmann's constant. This relationship holds regardless of the order of reaction and the value of the pre-exponential term (frequency factor) in the annealing equation. It is also valid where there is a broad distribution of frequency factors, as in the case of a diffusion-controlled annealing process involving diffusion jumps over a range of distances.

The data shown in Figure 4.2 (Ref. 23) can be analyzed in this way by comparing the total void volumes reached in 1 hr at 600 C, 800 C, and 900 C with the time-dependent annealing curve at 700 C. The data were

found to be in fair agreement with an effective activation energy of 2.3 eV. Since the rate-controlling process in void annealing is likely to be the emission of vacancies from voids and their migration to sinks, the effective activation energy would be expected to be that for self-diffusion. There do not appear to be any data for diffusion of the constituent elements in γ-stainless steel, but the activation energies for the diffusion of iron and nickel in γ-iron are reported to be 2.1 and 2.8 eV, respectively (Ref. 30). Thus, a value of 2.3 eV for the effective activation energy for void annealing is reasonable.

Figure 4.5 shows calculated curves for void annealing, based on the data in Ref. 23, which are extrapolated using Eq. 4.4 and an activation energy of 2.3 eV. The data were derived from an as-irradiated range of void diameters of approximately 67 A to 300 A, and other results for voids in this size range are in general agreement (Fig. 4.4). However, results showing the difficulty of fully annealing 1100-A-diameter voids at 1200 C indicate that if voids grow much bigger than 300 A during irradiation, there is a possibility that annealing the swelling will be much more difficult. Similarly, the annealing of smaller voids (for example, the sample with voids in the range 67 A to 187 A, Fig. 4.4.) will be accomplished in shorter times or at lower temperatures.

4.3.3. Limitations on Annealing as a Means of Controlling Swelling

There are two main limitations on the use of periodic annealing to control swelling of fast reactor components. The first concerns the size of voids in the irradiated material. As mentioned above, it is easier to anneal small voids than large voids, and voids larger than approximately 300 A in diameter may not be annealable in the time-temperature zones indicated in Fig. 4.5. Until experimental annealing data become available for void sizes between approximately 300 A and 1100 A, it is not possible to estimate the size where voids become unannealable under practicable conditions. However, it is possible to estimate roughly the irradiation conditions for which voids should

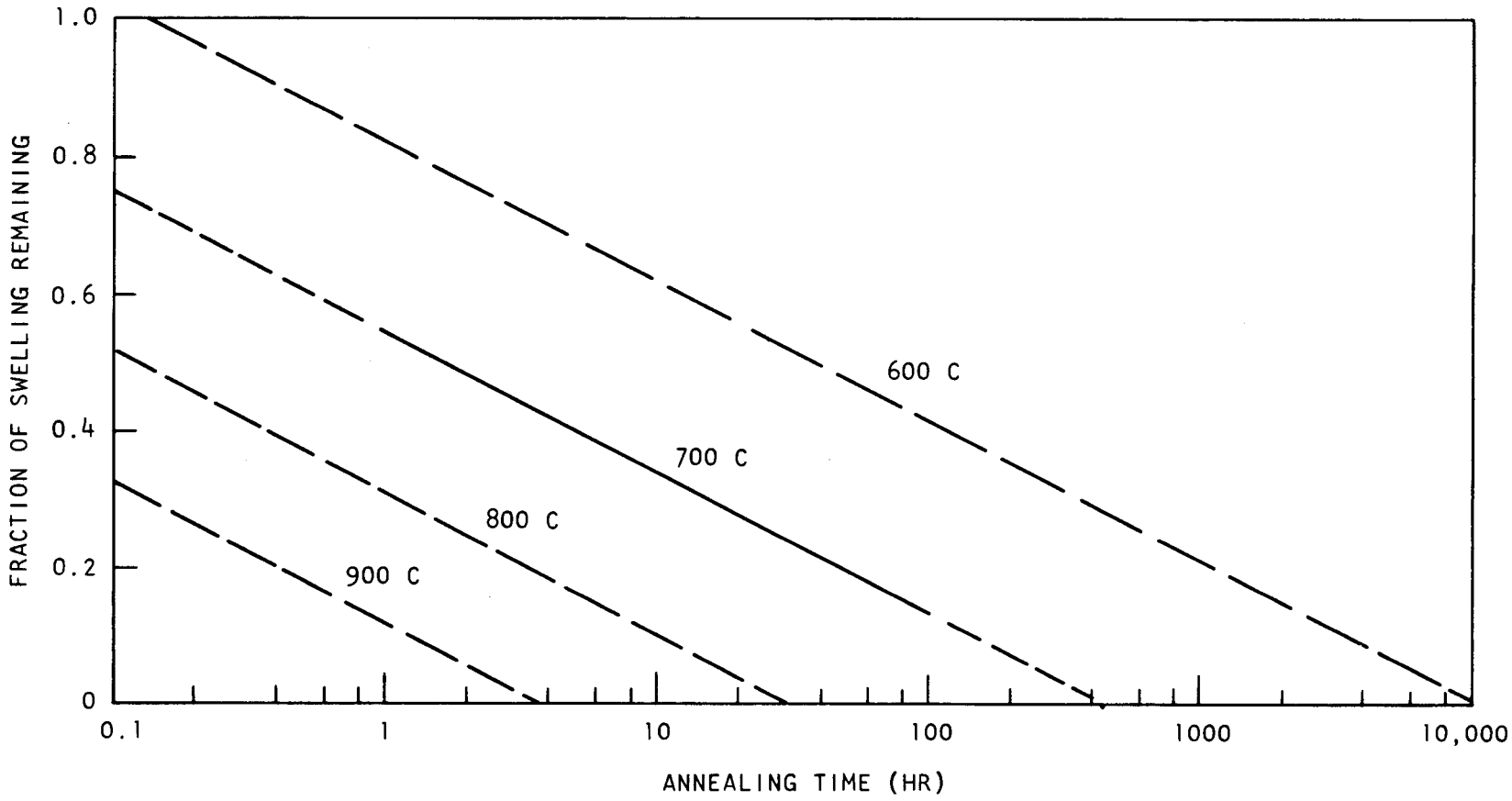

Fig. 4.5. Extrapolated annealing curves for the total void volume in irradiated types 304 and 316 stainless steel containing voids of diameter ≤300 A (effective activation energy = 2.3 eV)

be less than approximately 300 A in diameter. There are not enough results to define the variation of the void size distribution with irradiation temperature, and data on the mean size of voids as a function of fluence and temperature show a great deal of scatter. Typical results taken from Ref. 26 are shown in Fig. 4.6. This figure shows a general increase in mean void diameter with increasing temperature, and little, if any, dependence on neutron fluence. Because the annealing of samples with voids of mean diamter 210 A is completed at the same temperature as for samples with voids of maximum diameter 300 A (Fig. 4.4), it is possible to estimate that irradiation at temperatures below approximately 450 C will produce annealable voids. (See Fig. 4.6). Without more data on void sizes and annealing behavior, it is impossible to say whether voids produced at higher temperatures are likely to anneal.

A second limitation on the use of annealing to control swelling concerns the state of stress in the component. If the voids are large, an applied tensile stress will tend to make them grow. However, for most of the void sizes encountered in practice, the applied tensile stress required to make them grow to an appreciable extent is quite high. Even for void diameters of 300 A, a tensile stress of 25,000 psi would be needed to cause extensive void growth. A more important effect of stress is the possibility of creep deformation during annealing. Because of the extremely low ductility of highly irradiated stainless steels under creep conditions (typically about 1%), a stress high enough to cause a significant creep strain would create a risk of fracture during annealing. Even if the creep strain were not high enough to cause fracture, any extensive dislocation motion during annealing might sweep voids to grain boundaries, where their residual helium would further reduce the ductility during subsequent irradiation. Thus, it is important that the stress level in any component be too low to allow any plastic flow during annealing. In components operating in a temperature gradient, the void sizes may differ in different places. Thus, there is a possibility that during annealing, recovery of the original dimensions may occur faster in some places than in others. The possibility of generating internal stresses during annealing must therefore be taken into account.

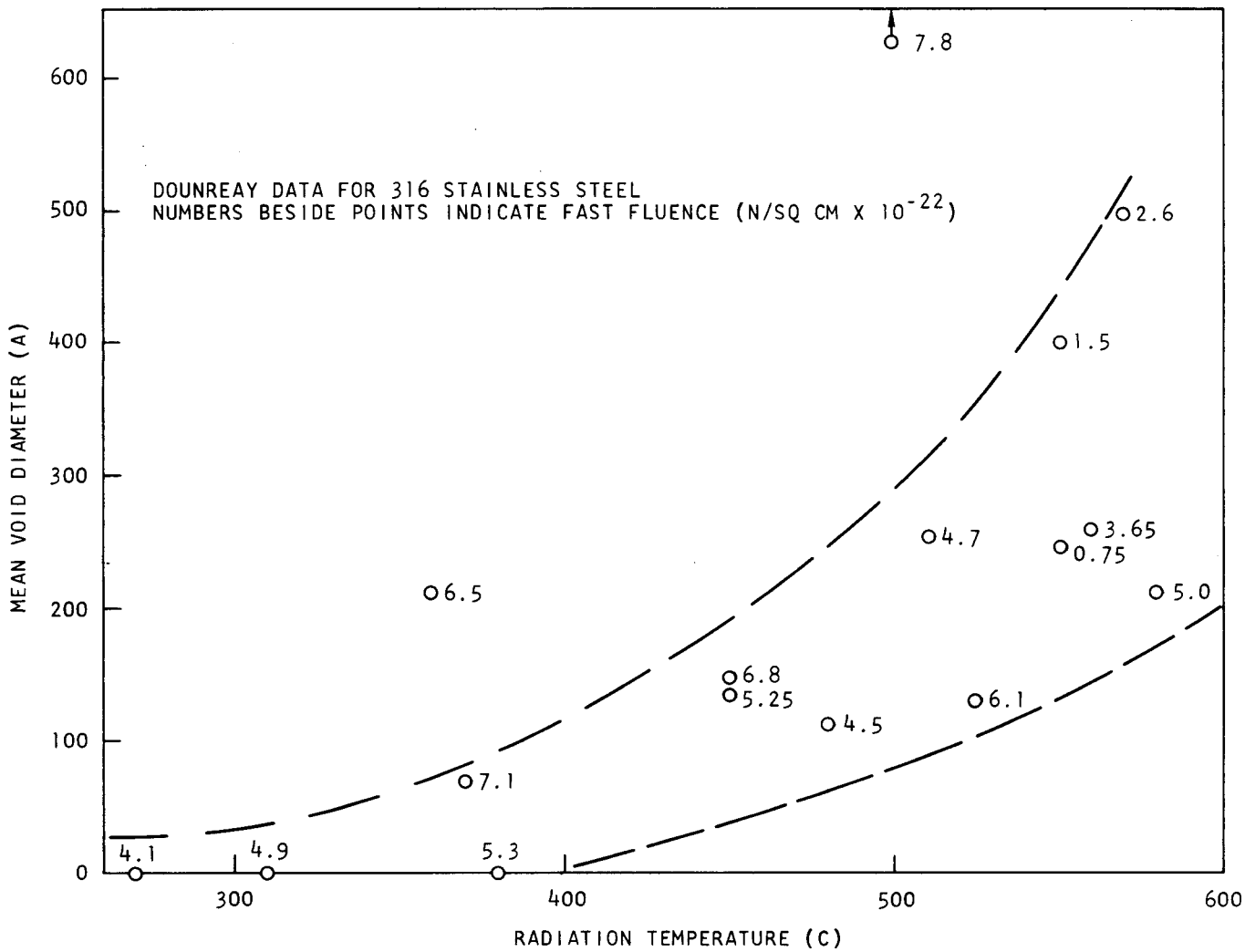

Fig. 4.6. Mean void diameter as a function of irradiation temperature for type 316 stainless steel irradiated in the DFR (data taken from Ref.26)

4.3.4. Summary and Conclusions

1. Periodic annealing may be a feasible way of recovering the original dimensions in fast-reactor structural components that have experienced radiation-induced swelling.

2. Where the swelling is caused by voids less than approximately 300 A in diameter, annealing is virtually complete in 1 hr at 800 C to 900 C, or in 100 hr at 700 C.

3. Small voids are removed rapidly during annealing, while large voids take longer and may temporarily increase in diameter. Voids 1100 A in diameter do not fully anneal in 1 hr at 1200 C.

4. The process of void annealing involves both the migration of vacancies from voids to sinks and that from smaller voids to larger voids. Because of this complexity, there is no simple model that can be used to describe fully the kinetics of annealing. Empirically, the annealing data for material containing 67 A to 300 A diameter voids established as a function of time at 700 C can be scaled to other temperatures according to an effective activation energy of 2.3 eV, thus providing a tentative basis for extrapolating the annealing curves to other times and temperatures.

5. The annealing curves should be valid for material containing voids up to approximately 300 A diameter, which corresponds roughly to irradiation temperatures up to 450 C. Annealing of larger voids may be more difficult, while annealing of samples containing no voids larger than 150 A to 200 A may be completed in shorter times or at lower temperatures.

6. To prevent possible fracture during annealing or increased embrittlement, annealing should only be performed on components whose stress level is not high enough to allow appreciable

plastic flow during annealing. The possibility of generating internal stresses during annealing must be taken into account.

7. More experimental work is needed to define the distributions and sizes of voids as a function of temperature, fluence, and annealing treatment before the predictions can be put on a firmer footing.

4.4. TRANSIENTS

During this reporting period a survey of available information on transient fuel rod behavior pertinent to the GCFR is being started. Initially this task will focus on determining whether enough information is available to establish failure criteria. Conceivable transients, including both neutronic excursions and loss of coolant accidents, will be reviewed and their time constants established. Work will be initiated to develop a descriptive model on fuel-rod behavior under the transient defined. This model development will be coordinated with similar programs at other facilities. As a result of this work, a definition will be made of additional experimental information required for the model development program.

4.5. TASK C - IRRADIATION TEST PROGRAM (IN-PILE AND OUT-OF-PILE TESTS)

4.5.1. Introduction

The fuel-element development program for the GCFR includes the irradiation testing of fuel rods under test conditions established in design studies of demonstration GCFR plants and large GCFR plants. Thermal flux and fast flux tests are included in the program. The thermal flux irradiation program is a joint effort of Gulf General Atomic and ORNL, with irradiations performed on UO_2- and $(Pu,U)O_2$-fueled rods in the ORR poolside facility (Refs. 31, 32). Data from short-term screening tests and high-burnup irradiations will be used to select the most promising fuel-rod concepts, design features, and parameters to be incorporated in future loop irradiations and fast-flux capsule tests. Design of a multirod fast-flux (EBR-II) capsule test is currently underway. Data on irradiation tests to date, tests underway, and tests being planned are summarized in Table 4.4. Information on the manifolded fuel rods, on the fast-flux tests to be conducted in EBR-II, and on the parameters to be tested during FY70 is also presented.

4.5.2. Irradiation Capsule 04P8

Fission gas analyses were performed on $(Pu,U)O_2$ fueled rods irradiated in ORR capsule 04P8 to exposures ranging from 47,000 to 59,000 MWd/Te at linear power generation ratings from 13.2 to 15.5 kW/ft and cladding o.d. surface temperatures from 610 C to 685 C. The results of the fission gas analysis are given in Table 4.5.

The results of the postirradiation visual examination, dimensional measurements, and gamma scanning of the 04P8 fuel rods were previously reported (Ref. 33). Additional postirradiation examination will include:

1. Void volume measurements interval to the fuel rods to provide information regarding the swelling of the $(Pu,U)O_2$ fuel (no external rod swelling was observed (Ref. 33).

TABLE 4.4

SUMMARY OF GCFR IRRADIATIONS

Test Identification	Test Reactor and Position	Schedule of Irrad. (hr)	Fuel-rod Type	Fuel-Clad. Thermal Bond	Fuel: Composition	Fuel: % TD[a]	Fuel: Geometry	Fuel: Stoichiometry (O/M)	Fuel: Fuel-Cladding Gap (in.)	Cladding: Composition	Cladding: Thickness OD (in.)	Conditions: Heat Rating (kW/ft)	Conditions: Max. Cladding Temperature (C)	Conditions: Burnup (MWD/tonne) Heavy Metal	Significant Features or Results
Gulf General Atomic–Oak Ridge National Laboratory GCFR Development-Program Thermal-flux Irradiation Tests Completed															
P4-A1 GA-1	ORR-P4	650	Sealed can	He	UO_2	~90	P,A[b]	2.005	0.0018	Hastelloy-X	0.0091/0.379	18/21.7	760		Specimens collapsed; negl. fuel support
GA-2	ORR-P4	650	Sealed can	He	UO_2	~90	P,A	2.005	0.0028	Hastelloy-X	0.0092/0.378	18/21.7	760	3,400	
P4-B2 GA-4	ORR-P4	800	Sealed can	He	UO_2	~90	P,A	2.006	0.001/0.0025	Hastelloy-X	0.014/0.342	18/16.2	760/673		Good condition; collapse in region of thin cladding; negligible fuel support
GA-5	ORR-P4	800	Sealed can, tapered cladding	He	UO_2	~90	P,A	2.006	0.0008/0.0023	Hastelloy-X	0.010-0.020/ 0.334-0.352	18/16.2	760/565	4,500	
P4-B3 GA-6	ORR-P4	1,340	Flex-can	Na	UO_2	~95	P	2.005	0.017	304 SS	0.010/0.375	14.7	650	5,600	Slight creep deformation
GA-7	ORR-P4	1,340	Sealed can	He	UO_2	~90	P,A	2.003	0.0036	Hastelloy-X	0.015/0.343	12.1	650	5,700	
P4-B4 GA-8	ORR-P4	2,000	Flex-can (c)	Na	UO_2	~95	P	2.0032	0.015	304 SS	0.010/0.375	13.5/15.1	700/715	8,300	Good collapse stability
GA-9	ORR-P4	2,000	Sealed can,PP	He	UO_2	~90	P	2.0032	0.0036	Hastelloy-X	0.015/0.343	11.4/12.6	650/715	8,800	
04-P5 GA-10	ORR-04	2,200	Sealed can,PP	He	UO_2	~90	P,A	2.0039	0.0035	Hast.-X partially surface-roughened	0.015/0.343	14.0	710	11,000	Some cladding deformation under thermocouple used to monitor temperature of OD
GA-11	ORR-04	2,200	Sealed can,PP	He	UO_2	~90	P,A	2.002	0.0035	Hast.-X partially surface-roughened	0.015/0.343	16.2	812	12,000	Good collapse stability
GAL-1 ORR Exp 16	ORR Loop	~4 total	Sealed can	He	UO_2	~90	P,A	2.003	0.003	Hast.-X partially surface-roughened	0.015/0.343	16	812	~10	
04-P6 GA-12	ORR-04	1,100	Sealed can	He	88 UO_2–12 PuO_2	~90	P,A	1.98/1.99	0.0033	Hast.-X partially surface-roughened	0.015/0.343	15	710	4,200	Good collapse stability
GA-13	ORR-04	1,100	Sealed can	He	88 UO_2–12 PuO_2	~90	P,A	1.98/1.99	0.0033	Hast.-X partially surface-roughened	0.015/0.343	18	812	4,800	Collapsed into oval shape; negligible fuel support
GA-14	ORR-04	1,100	Sealed can,PP	He	88 UO_2–12 PuO_2	~90	P,A	1.98/1.99	0.0033	Hast.-X partially surface-roughened	0.015/0.343	18	838	4,800	Cladding failed under thermocouple band; negligible fuel support
03-P7 GA-15	ORR-03	~7,800	Sealed can	He	UO_2	~90	P,A	2.002	0.0025	Hastelloy-X	0.020/0.353	6.8	750	~16,000	Irradiation discontinued at 16,000 MWD/tonne
GA-16	ORR-03	~7,800	Sealed can	He	88 UO_2–12 PuO_2	~90	P,A	1.98/1.99	0.0034	Hastelloy-X	0.020/0.353	8.2	750	~16,000	Fission-product leak detected in rod
04-P8 GA-17	ORR-04	~11,000	Sealed can	He	88 UO_2–12 PuO_2	~90	P,A	1.98/1.99	0.002	316 SS	0.024/0.355	13.2	610[d]	~47,000	
GA-18	ORR-04	~11,000	Sealed can	He	88 UO_2–12 PuO_2	~90	P,A	1.98/1.99	0.003	Hastelloy-X	0.015/0.343	15.5	700	~59,000	Fuel-rod specimens all in excellent condition; little, if any, deform. observed
GA-19	ORR-04	~11,000	Sealed can,PP	He	88 UO_2–12 PuO_2	~90	P,A	1.98/1.99	0.003	Hastelloy-X	0.015/0.343	15.5	700	~59,000	
Gulf General Atomic GCFR Development-Prooram Irradiation Tests Planned															
Thermal-flux Tests															
04-P9	ORR	~11,000	Manifolded to external plenum	He	88 UO_2–12 PuO_2	~90	P,A	~1.98	~0.003-0.004	316 SS	0.024/0.355	15	700	>50,000	Fission-product emission at top of fuel rod and top of fission-product trap will be monitored; instrumented rod and trap; rod external pressure ~950 psi, internal pressure ~1000 psi under normal operating conditions.
Fast-flux Tests															
F-1 Subassembly (7 rods)	EBR-II	~10,000	Manifolded to ext'nl plenum	He	85 UO_2–15 PuO_2	~90	P, A	~1.98	~0.002-0.003	316 SS	OD/ID ~1.15	12 - 16	700-800	>50,000	Not instrumented; ambient pressure
F-2 Subassembly (7 rods)	EBR-II	~10,000 to 20,000	Manifolded to ext'nl plenum and sealed can	He	85 UO_2–15 PuO_2	~90	P, A V[e]	~1.98	~0.002-0.003	316 SS Hast.-X (sealed can only)	OD/ID ~1.15	12 - 16	700-800	>50,000	Not instrumented, ambient pressure. Some sealed rods with high-strength cladding may also be included.

[a] Smear density was less than or equal to 85% of theoretical.

[b] Pellet, annular.

[c] PP = Prepressurized rod (external pressure 800 to 1000 psi in capsules, 300 psi in loop.

[d] Temperature swing on this rod was from 560 C to 660 C during each reactor cycle.

[e] Vibratory compacted.

TABLE 4.5

GAS CONTENT OF FUEL RODS IN CAPSULE 04P8 BASED ON MASS SPECTROGRAPHIC ANALYSIS

Total Gas Content

Fuel-Rod Specimen	Helium Pressure ST, Before Irradiation (psia)	Gas Composition (vol-%)						
		He	Kr	Xe	N_2+CO	H_2O	A	H_2
GA-17	14.7	4.9	7.5	85.6	0.42	0.11	1.4	0.08
GA-18	14.7	3.8	7.7	87.4	0.16	0.17	0.39	0.22
GA-19	260.0 (prepressurized)	47.7	4.2	47.9	0.06	0.02	0.01	0.15

Isotopic Analysis of Kr and Xe (vol-%)

Isotope	Fuel-rod specimen		
	GA-17	GA-18	GA-19
Kr-83	15.17	14.36	14.31
Kr-84	28.76	29.36	29.36
Kr-85	7.26	7.34	7.27
Kr-86	48.81	48.9	49.06
Xe-130	0.07	0.09	0.09
Xe-131	12.51	11.87	11.69
Xe-132	19.35	19.02	18.98
Xe-134	28.25	27.72	27.77
Xe-136	39.82	41.30	41.47

2. Burnup analysis and neutron dosimetry wire analysis

3. Metallography on representative sections and microprobe analysis where the requirement is indicated

4. Analysis of fission product distribution on the plenums

5. Cladding mechanical property tests to evaluate the amount of degradation associated with fuel-cladding interaction and neutron irradiation

During the quarter, additional postirradiation data were received from ORNL, which give the composition of the gases released from fuel rods GA-17, GA-18, and GA-19 of Capsule 04P8 when they were punctured. Previously, data on the pressure-volume measurements of these gases had been received. These data were analyzed to determine the internal pressure of the rods after irradiation.

Assuming the ideal gas law to be applicable,

$$pv = (n_{He} + n_{Kr} + n_{Xe} + n_{other})\ RT \quad ,$$

where

p = total pressure
v = void or gas volume in rods
n = number of moles of gas

and subscripts refer to gas elements.

Then $pv = n_{He}\ RT \left(1 + \frac{n_{Kr}}{n_{He}} + \frac{n_{Xe}}{n_{He}} + \frac{n_{other}}{n_{He}}\right)$

The ratios $\left(n_{Kr}/n_{He}\right)$, $\left(n_{Xe}/n_{He}\right)$, and $\left(n_{other}/n_{He}\right)$ are provided from the composition analysis data. The absolute value of n_{He} was obtained from the conditions at the time the rods were fabricated, assembled,

and sealed since negligible He is generated during irradiation. When the initial number of moles of He in the above equation are included,

$$p_1 v_1 = \left(\frac{p_0 v_0}{RT}\right) RT \left(1 + \frac{n_{Kr}}{n_{He}} + \frac{n_{Xe}}{n_{He}} + \frac{n_{other}}{n_{Xe}}\right) ,$$

where the subscripts 1 and 0 refer to the end of irradiation and time of sealing the rods just before irradiation, respectively.

Then, it is found that

$$p_1 = p_0 \frac{v_0}{v_1} \left(1 + \frac{n_{Kr}}{n_{He}} + \frac{n_{Xe}}{n_{He}} + \frac{n_{other}}{n_{He}}\right) ,$$

Thus, the final internal gas pressure can be obtained provided that the initial and final void or gas volumes are the same or are known. With the assumption that $v_0/v_1 = 1.0$, p_1 was computed and subsequently divided into the pv values measured at the end of irradiation to find v_1. As a test of the assumption the final values of void or gas volume determined in this way are compared in Table 4.6 with the initial values computed from preirradiation fuel characterization and dimensional measurements.

Since the initial and final void volumes agree within a few percent, as assumed above, the calculated fission gas pressures at the end of life (at room temperature, 295K) by the method outlined above are correct and are shown in Table 4.6. Also shown is the pressure at 436 K, the temperature of the plenum estimated for the design calculations. The actual operating pressures at the end of irradiation were greater than the values at 436 K since one-half, one-half, and one-third of the void volumes in the GA-17, GA-18, and GA-19 fuel rods, respectively, were in the fuel at higher than plenum temperatures. However, detailed information on the temperature and void distributions in the fuel is needed before these incremental additions can be found.

TABLE 4.6

FUEL ROD INTERNAL PRESSURE AND VOID VOLUMES
IN CAPSULE 04P8

Fuel Rod No.	Void Volumes: Calc from ORNL Composition and Gas Vol Measurements (cc)	Void Volumes: Calc. from GGA Preirradiation data (cc)	ΔV (Initial-Final) (%)	Final Internal Fuel-Rod Pressure (psia) at 295 K	Final Internal Fuel-Rod Pressure (psia) at 436 K
GA-17	1.200	1.219	1.56	277	410
GA-18	1.187	1.223	2.94	498	736
GA-19	2.160	2.136	-1.125	688	1018

4.5.3. Chemical Analyses of $(Pu,U)O_2$ Fuel Used in Irradiation Capsules 04P6, 03P7, and 04P8.

Because anomalies have occurred (Refs. 33, 34) in the irradiation behavior of these $(Pu,U)O_2$ fueled rods and because ORNL postirradiation analyses of the 04P6 fuel indicated presence of ThO_2, BMI, the fabricator of the fuel pellets, was requested to perform complete analyses of the PuO_2 starting material and sintered control pellets. The results of the analyses shed no light on the anomalies in fuel-rod behavior observed and show that no significant amount of ThO_2 was present in either the starting material or the finished pellets.

The control history specimen of PuO_2 (Lot A82) was analyzed for plutonium content by two different techniques. First, a known amount of PuO_2 was dissolved in HnO_3-HF and diluted to a specific volume, and a number of volumetric samples were taken from this solution and dried. The alpha activity from the dry residue indicated that the PuO_2 (Lot A82) was essentially 100% PuO_2 based on the expected activity from Pu-239, Pu-240, Pu-241, and Pu-242. The presence of ThO_2 in the PuO_2 would have been indicated by a gross lowering of the alpha activity per unit weight. Second, specimens of PuO_2 (Lot A82) were dissolved in HCl and examined by spetrophotometric techniques. In this process, the plutonium in solution is reduced to Pu^{+3} ions and the spectral absorbance of the final solution compared to a standard curve. Again, the characteristics of the solution (Pu^{+3}) indicated that the oxide powder was 100% PuO_2. From the results of these two determinations, it was reasonable to assume that the PuO_2 starting material was fairly pure PuO_2, certainly with no appreciable ThO_2 content.

The control history specimens of the mixed oxides, UO_2-12wt-% PuO_2, as available from Gulf General Atomic fuel assemblies 04P6, 04P7, and 04P8 were also analyzed for ThO_2 and PuO_2 by wet chemical and laser microprobe techniques. In the wet chemical process, triplicate specimens taken from a single M-14 pellet representative of all material used in

04P8 (GA-17, GA-18, and GA-19) loading were dissolved in HNO_3-HF and passed over a Dowex ion exchange column. This removed the plutonium from the solution. The plutonium was then stripped from the column and titrated with a standard cerium ammonium sulfate solution. The results showed a plutonium (Pu not PuO_2) concentration of 11.0, 11.1, and 11.5 wt-% (average 11.2 wt-%) as compared to 10.63 wt-% theoretical for $U_{0.88}Pu_{0.12}O_{1.98}$. The results seem to be consistent, but at this time it is not known whether the higher than expected level is due to the procedure or to the composition. It is reported that most analyses of this type at BMI on mixed oxide fuel material have been biased toward the high side. If it is a valid compositional analysis, the plutonium content will be high by 5.35%. Uranium values were also determined for these samples. Again, a consistent but high value was found (85.4, 84.7, and 84.5 wt-% as compared to 77.63 wt-% theoretical). Obviously, the uranium values, which are approximately 9.3 wt-% higher than expected, are biased more than the plutonium figures. If both figures were high to the same relative extent, then perhaps they could be adjusted downward so that U + Pu would total to 88.26 wt-%.

Sintered control specimens from capsules 04P6 and 03P7 and from sintering runs M-12 and M-14 of capsule 04P8 were laser probed along with sintered specimens of PuO_2 and ThO_2. In this technique, a laser beam burns out a crater (25 to 40 μm in diameter) from the exterior of the pellet. Five positions were probed for each pellet, three along the length of the pellet and one on each end face. From the pure ThO_2 pellet, identification lines were detected at 3188, 3601, 4020, 4381, and 4391 A. The PuO_2 spectrum for our range showed only one line at 4019 A and others toward the high end of the range, which were too high for positive identification studies. In the mixed oxide specimens, only the uranium spectrum plus the line at 4019 A were detectable; other lines present were attributed to minor impurities. The intensity ratio of the strongest uranium line to the plutonium line was approximately the same for all laser shots with the mixed oxides, all having 12 wt-% PuO_2. Since I_U to I_{PU} was essentially constant, this would further attest to

the homogeneity achieved during mechanical blending. The results of the laser microprobe indicated the absence of ThO_2 and the excellent homogeneity in the mixed oxide UO_2-12 wt-% PuO_2 sintered material.

Based on both studies, those with PuO_2 (Lot A82) and those with UO_2-12 wt-% PuO_2, from the three capsule loadings, no significant ThO_2 was in the material fabricated at BMI, and the mixed oxide material produced at BMI was UO_2-12 wt-% PuO_2 and of excellent homogeneity.

4.5.4. Irradiation Capsule 04P9

Capsule 04P9 scheduled for irradiation in the ORR will contain one manifolded (Pu-U)O_2-fueled rod, which will be irradiated to 50,000 MWd/Te burnup at a linear heat-generation rate of 15 kW/ft and at a maximum cladding outer surface temperature of 700 C. The objectives of the irradiation have been discussed previously (Ref. 35). Evaluation of the charcoal fission-product trap is one of the objectives of the test and preirradiation evaluation accomplished during this period is described in Sections 4.5.4.2 and 4.5.4.3. The fuel rod will contain a fission-product trap which will operate with an outer surface temperature of approximately 300 C. The design layout of the fuel-rod specimen is shown in Fig. 4.7 and a schematic of the fission-product-trap monitoring system is shown in Fig. 4.8. A layout of the capsule design is shown in Fig. 4.9. The planned test conditions for capsule 04P9 are given in Table 4.7.

4.5.4.1. Fabrication. Fabrication of the fuel rod for 04P9 capsule has been completed. The fuel data and assembly details for the fuel rod are given in Table 4.8. The 04P9 fuel-rod encapsulation and preirradiation equipment and test procedure checkouts are proceeding at ORNL.

4.5.4.2. Experimental Studies. Laboratory experiments related to the release of noble gases are continuing. Two basic parameters are being measured: (1) the adsorption coefficient K for krypton and xenon

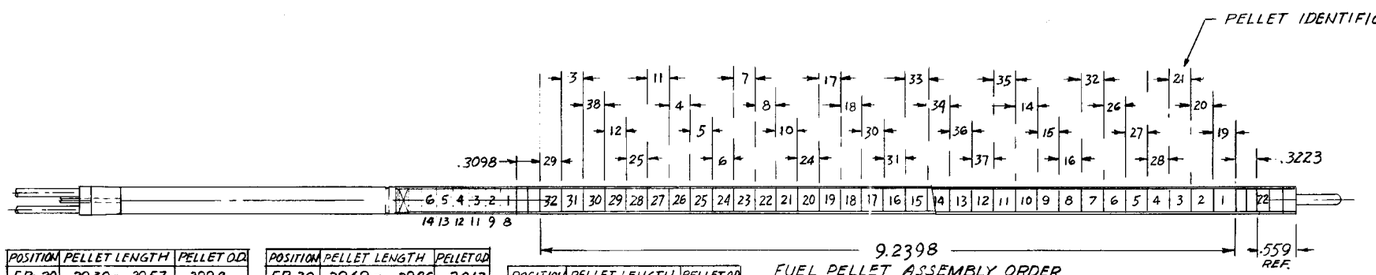

NOTES:

1. ALL DIMENSIONS EXCEPT OVERALL DIMENSIONS ARE REFERENCE & NOMINAL
2. SELECT PELLETS PER SPEC. 393-5002
3. ASSEMBLE PER SPEC. 393- _____
4. ITEM 10 POSITIONED BY ROLLING METHOD OR BY "MAGNA-FORM"
5. UIP - UPPER INSULATOR PELLET
   UBP - UPPER BLANKET PELLET
   USP-8.3 - UPPER SUPPRESSOR PELLET
   USP-14.9 - UPPER SUPPRESSOR PELLET
   FP- FUEL PELLET
   LSP-14.9 - LOWER SUPPRESSOR PELLET
   LSP-8.3 LOWER SUPPRESSOR PELLET
   LBP- LOWER BLANKET PELLET
   LIP- LOWER INSULATOR PELLET

POSITION	PELLET LENGTH	PELLET O.D.
FP-10	.2768-.2770	.3007
FP-9	.2740-.2774	.3007
FP-8	2733 - 2746	.3007
FP-7	.2935 - .2940	.3009
FP-6	.2940 - .2945	.2998
FP-5	.2960 - .2961	.2997
FP-4	.2975 - .2959	.2998
FP-3	.2959 - .2963	.2995
FP-2	.2945 - .2948	.3006
FP-1	.2968-.2975	.3007

POSITION	PELLET LENGTH	PELLET O.D.
FP-20	.2930 - .2957	.2998
FP-19	.2985 - .2997	.3004
FP-18	.3188 - .3192	3007
FP-17	.2932 - .2937	.3004
FP-16	.2916 - .2929	.3006
FP-15	.2944 - .2947	.3006
FP-14	.2944 - .2946	.3005
FP-13	.2776 - .2786	.3003
FP-12	.2937 - .2941	.3008
FP-11	.2828 - .2829	.3007

POSITION	PELLET LENGTH	PELLET O.D.
FP-30	.2969 - .2985	.3013
FP-29	.2763 - .2766	.3005
FP-28	.2953 - .2958	.2998
FP-27	.2963 - .2978	.3007
FP-26	.2731	.3004
FP-25	.2759	.3006
FP-24	.2765	.3006
FP-23	.2774	.3004
FP-22	.2763	.3006
FP-21	.2747	.3006

POSITION	PELLET LENGTH	PELLET O.D.
LBP-22	.187	.3015
UBP-6	.3264	.3014
UBP-5	.3273	.3013
UBP-4	.3273	.3014
UBP-3	.3285	.3014
UBP-2	.3213	.3013
UBP-1	.3275	.3014
FP-32	.2945 - .2952	.3045
FP-31	.2760	.3013

POSITION	PELLET LENGTH	PELLET O.D.
LSP-9	.1624	.3012
LSP-67	.1599	.3012
USP-10	.1480	.3012
USP-16	.1618	.3012
LIP-X	.187	.3015
UIP-X	.187	.3015

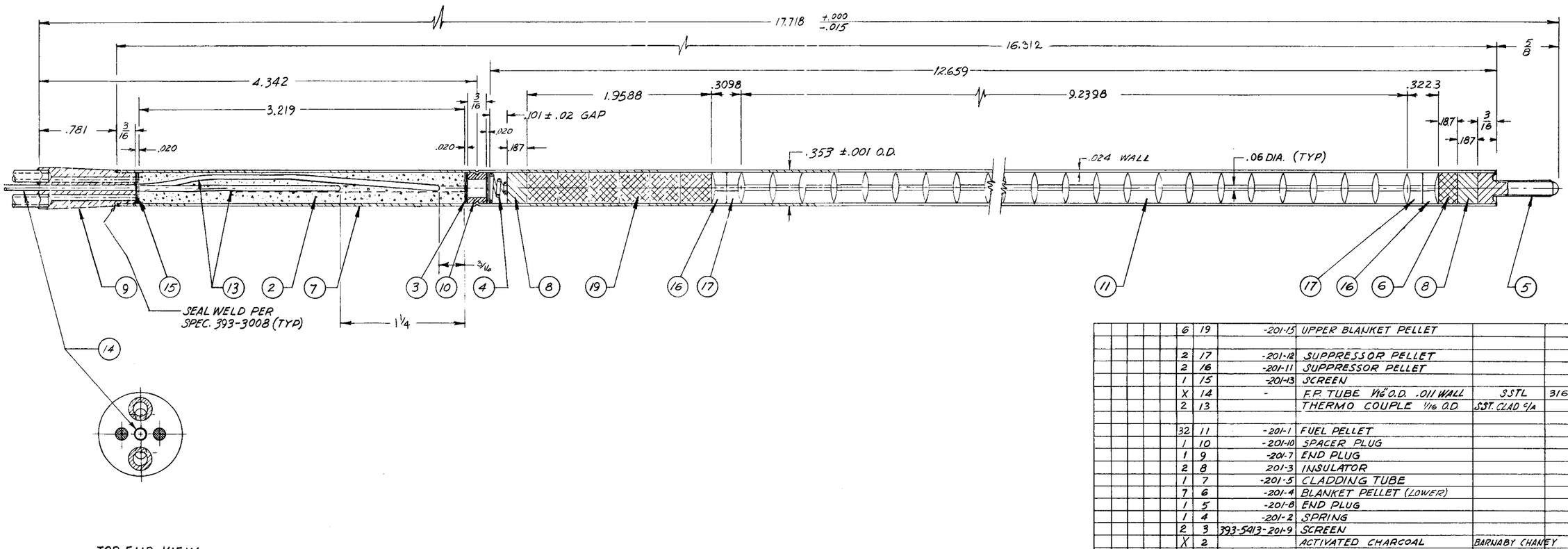

					6	19	-201-15	UPPER BLANKET PELLET		
					2	17	-201-12	SUPPRESSOR PELLET		
					2	16	-201-11	SUPPRESSOR PELLET		
					1	15	-201-13	SCREEN		
					X	14	-	F.P. TUBE 1/16" O.D. .011 WALL	SSTL	316
					2	13		THERMO COUPLE 1/16 O.D.	SST. CLAD C/A	
					32	11	-201-1	FUEL PELLET		
					1	10	-201-10	SPACER PLUG		
					1	9	-201-7	END PLUG		
					2	8	201-3	INSULATOR		
					1	7	-201-5	CLADDING TUBE		
					7	6	-201-4	BLANKET PELLET (LOWER)		
					1	5	-201-8	END PLUG		
					1	4	-201-2	SPRING		
					2	3	393-5413-201-9	SCREEN		
					X	2		ACTIVATED CHARCOAL	BARNABY CHANEY IM	
						1	-1	ASSEMBLY		
					-1					

Fig. 4.7. Detail of parts for capsule P9 (Part 1)

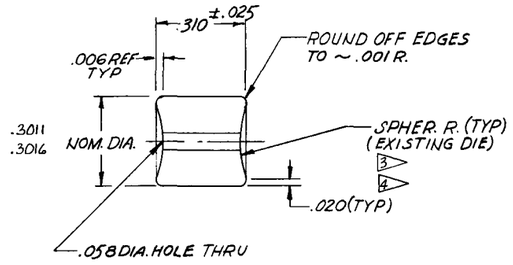

(1)

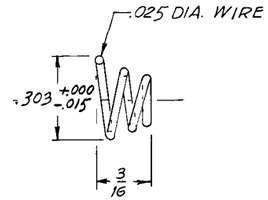

(2)

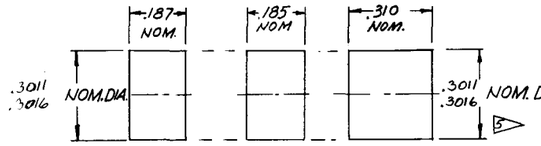

(3) (15) (4)

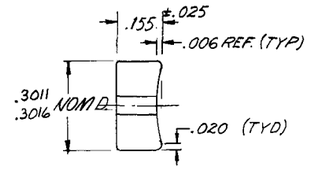

(11) (12)

NOTES:

1. REMOVE ALL BURRS & SHARP EDGES.
2. DIA. OF FUEL PELLETS TO BE .003 TO .005 LESS THAN THE MEASURED AVERAGE TUBE I.D. TOLERANCE ON FINISHED PELLET TO BE ±.0005; METHOD OF MEAS. TUBE I.D. TO BE IN ACCORDANCE WITH SPEC. 393-5001
3. USE EXISTING DIE GGA TOOL NO. 393-DH-275
4. FUEL PELLETS TO BE FABRICATED IN ACCORDANCE WITH SPEC. 393-3007
5. USE EXISTING DIE GGA TOOL NO. 393-F-280.
6. TUBE I.D. TO BE MEASURED PER SPEC. 393-5001 TUBE WALL THICKNESS TO BE MEASURED PER SPEC. 393-5003.
7. MAKE FROM .375 O.D. X .031 WALL TUBE. GRIND OUTSIDE DIA. ON A HARDENED STEEL MANDRIL TO DIMENSION SHOWN.
8. TOLERANCE SYMBOLS PER MIL-STD-8.
9. DIA. TO BE .0005 -.001 SMALLER THAN MEAS. I.D. OF ITEM (5).

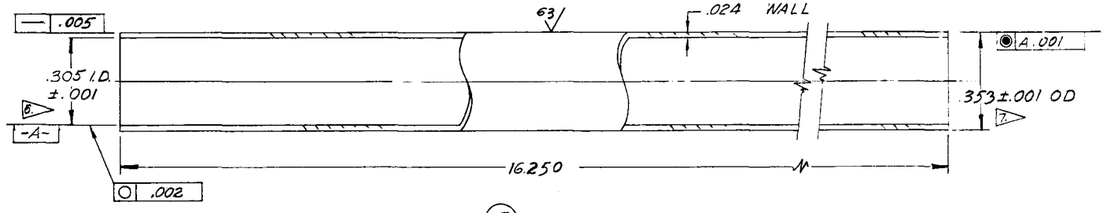

(5)

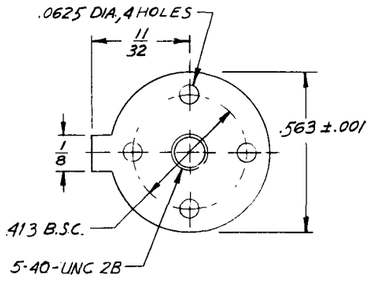

(6)

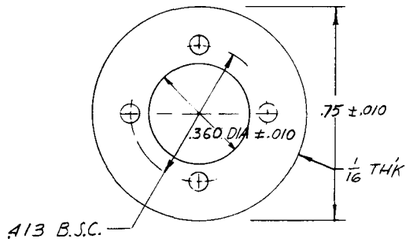

(14)

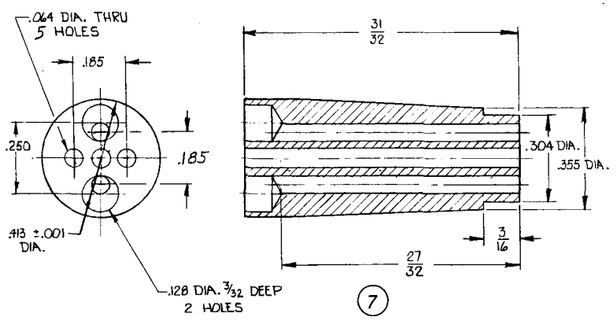

(7)

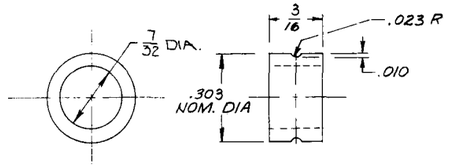

(10)

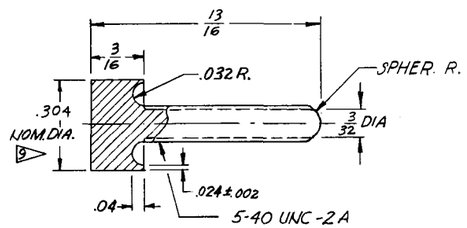

(8)

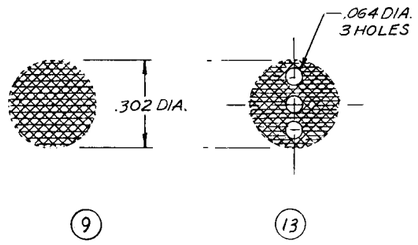

(9) (13)

						15		LOWER BLANKET PELLETS	DEPL. UO_2	
						14		LOCATING COLLAR	SST-304	
						13		SCREEN	SST-316	30-40 MESH
						12		SUPPRESSOR PELLET	83% Enr UO_2	393-2016
						11		SUPPRESSOR PELLET	14.9% Enr UO_2	393-2016
						10		SPACER PLUG	ST STL-316	393-2014
						9		SCREEN	ST STL-316	30-40 MESH
						8		END PLUG	ST STL-316	393-2013
						7		END PLUG	ST STL-316	393-2013
						6		BOTTOM LOCK 1/32 THK	ST STL-304	
						5		CLADDING TUBE	ST STL-316	393-2015
						4		BLANKET PELLET (UPPER)	DEPL. UO_2	393-2009
						3		INSULATOR PELLET	AL_2O_3	393-2008
						2		SPRING	INCONEL	718, 393-3017
						1		FUEL PELLET	PUO_2-UO_2	393-2012

Fig. 4.7. Detail of parts for capsule P9 (Part 2)

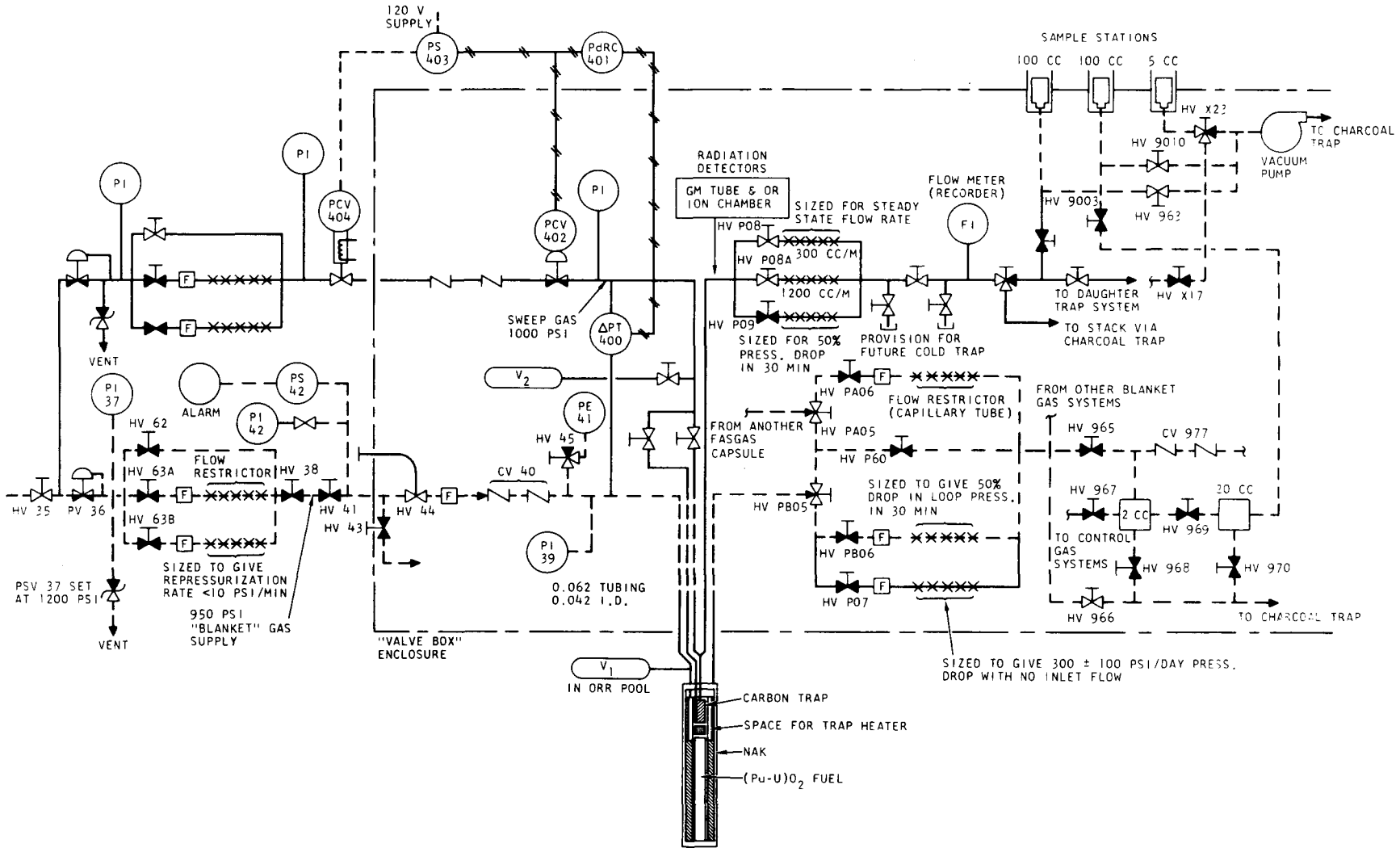

Fig. 4.8. Diagram of fission-product-trap monitoring system for capsule 04P9

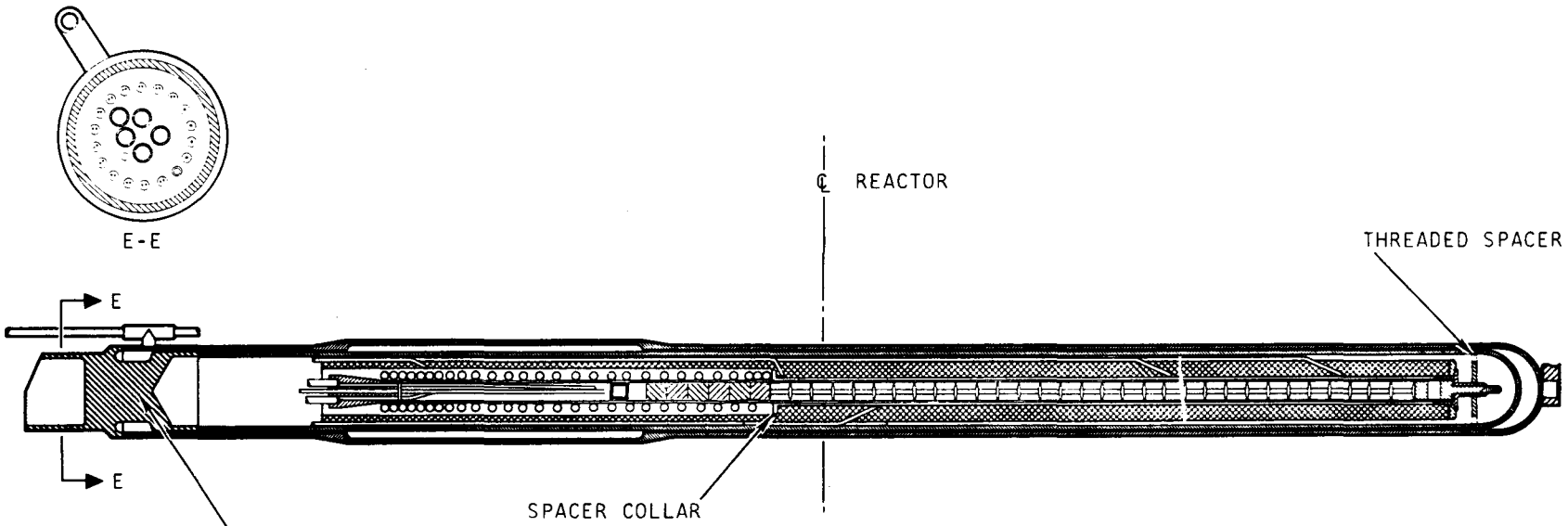

DESIGN FOR GCFR CAPSULE P9. (MODIFICATION OF EXISTING P8 PARTS, I.E., LINEAR POWER GENERATION = 15 KW/FT @ CLAD TEMPERATURE OF 700°C)

Fig. 4.9. Capsule 04P9 design

TABLE 4.7

PLANNED IRRADIATION TEST CONDITIONS FOR CAPSULE 04P9

Rod specimen	GA-20
Cladding material	316 SS
Cladding o.d., in.	0.355
Cladding thickness, in.	0.024
Cladding o.d./i.d.	1.156
Bond-gap fluid	Helium
Cladding o.d. surface temperature, C	700 + 0, - 25
Fuel	[88 U (9% enr)-12 Pu]O_2
Fuel smear density, % TD	$\leq$85
Linear power generation (max), kW/ft.	15±2
Burnup exposure, MWd/Te	$\geq$50,000 (15 x 10^{20} f/cc)
External pressure, psig	950±25
Initial internal trap pressure, hot, psig	1000±25
End-of-life internal trap pressure, hot, psig.	1000±25
Trap temperature surface, C	300±50
Pressure differential trap wall, psi	50, nominal; not to exceed 300
Number of power (temperature) cycles	100 standard (700 C → 300 C → 700 C); 6 nonstandard (700 C → x → 700 C)
Number of pressure cycles.	20 standard (1000 psig → 100 psig → 1000 psig); 9 nonstandard (1000 psig → x → 1000 psig)

TABLE 4,8

CAPSULE 04P9 FUEL ROD LOADING DATA

Pellet Type[a] and Position	Pellet Identification	Oxygen-to-Metal Ratio	Pellet wt (g)	U wt (g)	U-235 wt (g)	Pu wt (g)	Pellet length (in.)	Pellet i.d. (in.)	Pellet o.d. (in.)	Cladding i.d. (in.)	Fuel Cladding Diametral Gap (in.)	Pellet Density (g/cc)/ % TD	Smear Density (g/cc)/ %SD
Axial Gap	--	--	--	--	--	--	.101-.026	--	--	--	--	--	--
UIP	X	--	--	--	--	--	.187	--	.3015	--	--	--	--
UBP 6	14	2.0038	--	--	--	--	.326	--	.3014	--	--	--	--
UBP 5	13	2.0038	--	--	--	--	.3273	--	.3013	--	--	--	--
UBP 4	12	2.0038	--	--	--	--	.3273	--	.3014	--	--	--	--
UBP 3	11	2.0038	--	--	--	--	.3285	--	.3014	--	--	--	--
UBP 2	9	2.0038	--	--	--	--	.3218	--	.3013	--	--	--	--
UBP 1	8	2.0038	--	--	--	--	.3275	--	.3014	--	--	--	--
Totals	--	--	--	--	--	--	1.9588	--	--	--	--	--	--
USP 8.3	No i.d.	2.005	--	--	--	--	.1480	--	.3012	--	--	--	--
USP 14.9	16	2.004	--	--	--	--	.1618	--	.3012	--	--	--	--
Totals	--	--	--	--	--	--	.3098	--	--	--	--	--	--
FP 32	29	--	3.330	2.5934	.2334	.3634	.2952/.2945	.06	.3013	.3045	.0032	91.8/10.80	9.47/ 865
FP 31	3	1.983	3.056	2.3558	.2120	.3335	.2760	.06	.3013	.3045	.0032	9.89/90.07	9.27/ 846
FP 30	38	1.9925	3.254	2.5084	.2257	.3551	.2969/.2985	.06	.3013	.3045	.0032	9.76/88.9	9.16/ 830
FP 29	12	1.983	3.069	2.3658	.2129	.3349	.2763/.2766	.06	.3005	.3045	.0040	9.96/90.7	9.30/ 849
FP 28	25	1.9925	3.247	2.5031	.2252	.3543	.2953/.2958	.06	.2998	.3045	.0047	9.91/90.3	9.20/ 838
FP 27	11	1.983	3.337	2.5724	.2315	.3641	.2963/.2978	.06	.3007	.3045	.0038	10.07/91.7	9.41/ 859
FP 26	4	1.983	3.036	2.3404	.2106	.3313	.2731	.06	.3004	.3045	.0041	9.79/89.16	9.31/ 850
FP 25	5	1.983	3.064	2.3620	.2126	.3343	.2759	.06	.3006	.3045	.0039	9.97/90.8	9.30/ 849
FP 24	6	1.983	3.073	2.3689	.2132	.3353	.2765	.06	.3006	.3045	.0039	9.97/90.8	9.31/ 850
FP 23	7	1.983	3.061	2.3597	.2124	.3340	.2774	.06	.3004	.3045	.0041	9.91/90.26	9.24/ 844
FP 22	8	1.983	3.053	2.3535	.2118	.3331	.2763	.06	.3006	.3045	.0039	9.92/90.35	9.26/ 846
FP 21	10	1.983	3.021	2.3288	.2096	.3296	.2747	.06	.3006	.3045	.0039	9.87/89.89	9.21/ 841
FP 20	24	1.9925	3.253	2.5077	.2257	.3547	.2930/.2957	.06	.2998	.3045	.0047	9.97/90.8	9.25/ 842
FP 19	17	1.984	3.289	2.7645	.1588	.2497	.2985/.2997	.06	.3004	.3045	.0041	9.86/89.8	9.21/ 841
FP 18	18	1.984	3.536	2.7258	.2453	.3858	.3188/.3192	.06	.3007	.3045	.0038	9.94/90.5	9.29/ 848
FP 17	30	1.9925	3.221	2.4830	.2235	.3515	.2932/.2937	.06	.3004	.3045	.0041	9.87/89.9	9.19/ 837
FP 16	31	1.9925	3.205	2.4707	.2224	.3497	.2916/.2929	.06	.3006	.3045	.0039	9.84/89.6	9.19/ 837
FP 15	33	1.9925	3.258	2.5115	.2260	.3555	.2944/.2947	.06	.3006	.3045	.0039	9.98/90.3	9.27/ 844
FP 14	34	1.9925	3.264	2.5161	.2264	.3562	.2944/.2946	.06	.3005	.3045	.0040	9.96/90.7	9.28/ 845
FP 13	36	1.9925	3.035	2.3396	.2105	.3312	.2776/.2786	.06	.3003	.3045	.0042	9.80/89.3	9.14/ 832
FP 12	37	1.9925	3.233	2.4923	.2243	.3528	.2937/.2941	.06	.3008	.3045	.0037	9.88/90.0	9.22/ 840
FP 11	35	1.9925	3.104	2.3928	.2155	.3387	.2828/.2829	.06	.3007	.3045	.0038	9.86/89.8	9.19/ 837
FP 10	14	1.983	3.044	2.3466	.2112	.3322	.2768/.2770	.06	.3007	.3045	.0038	9.85/89.7	9.20/ 840
FP 9	15	1.983	3.040	2.3435	.2109	.3317	.2740/.2774	.06	.3007	.3045	.0038	9.88/90.0	9.24/ 844
FP 8	16	1.983	2.985	2.3011	.2071	.3257	.2733/.2746	.06	.3007	.3045	.0038	9.78/89.1	9.13/ 834
FP 7	32	1.9925	3.233	2.4923	.2243	.3528	.2935/.2940	.06	.3009	.3045	.0036	9.86/89.8	9.22/ 839
FP 6	26	1.9925	3.251	2.5061	.2255	.3547	.2940/.2945	.06	.2998	.3045	.0047	9.99/91.0	9.25/ 842
FP 5	27	1.9925	3.256	2.5099	.2259	.3553	.2960/.2961	.06	.2997	.3045	.0048	9.93/90.4	9.21/ 840
FP 4	28	1.9925	3.224	2.4853	.2237	.3518	.2975/.2959	.06	.2998	.3045	.0047	9.82/89.4	9.05/ 824
FP 3	21	1.9925	3.239	2.4969	.2247	.3534	.2959/.2963	.06	.2995	.3045	.0050	9.89/90.1	9.16/ 834
FP 2	20	1.9925	3.232	2.4915	.2242	.3527	.2945/.2948	.06	.3006	.3045	.0039	9.84/89.6	9.19/ 837
FP 1	19	1.984	3.244	2.5007	.2250	.3539	.2968/.2975	.06	.3007	.3045	.0038	9.79/89.1	9.14/ 835
Totals	--	--	101.747	78.435	7.059	11.1026	9.2398	--	--	--	--	--	--
LSP 14.9	9	2.004	--	--	--	--	.1624	--	.3012	--	--	--	--
LSP 8.3	67	2.005	--	--	--	--	.1599	--	.3012	--	--	--	--
Totals	--	--	--	--	--	--	.3223	--	--	--	--	--	--
LBP	22	--	--	--	--	--	.187	--	.3015	--	--	--	--
LIP	X	--	--	--	--	--	.187	--	.3015	--	--	--	--

[a] Defined as

UIP = upper insulator pellet Al_2O_3
UBP = upper blanket pellet depleted UO_2
USP 8.3 = upper suppressor pellet 8.3% enriched UO_2
USP 14.9 = upper suppressor pellet 14.9% enriched UO_2
FP = fuel pellet 12.4 PuO_2-87.6 UO_2 (9% enriched)
LSP 14.9 = lower suppressor pellet 14.9% enriched UO_2
LSP 8.3 = lower suppressor pellet 8.3% enriched UO_2
LBP = lower blanket pellet depleted UO_2
LIP = lower insulator pellet Al_2O_3

on activated carbon and (2) the diffusion coefficient D_{12} for the gas pairs Kr-He and Xe-He. These data provide input to computer calculations (see Section 4.5.4.3) for estimation of diffusion delay times and therefore fission product release fractions from a manifolded and vented fuel specimen, such as the 04P9. The comparison of the actual in-pile performance of 04P9 with the estimated fission product release fractions will then be used to determine the design release fractions for the GCFR fuel element.

The adsorption coefficient experiments are complete and are reported in two previous GCFR quarterly reports (Refs. 33, 35).

Additional tests are underway using a new rig comprised of a 72-in.-long diffusion tube, as compared to the previous rig which used a 19.7-in.-long tube.

In the last quarterly report (Ref. 33) experimental data on the interdiffusion coefficient for Kr in He, (D_{12}), were given. An anomalous departure of D_{12} from the expected linear dependence on inverse pressure was reported. (See Fig. 4.11 of Ref. 33.) Diffusion coefficients measured at 1000 psi He were observed to be about 20% higher than anticipated. Experimental work performed during the current quarter was aimed at determining the nature and cause of this behavior.

Preliminary causal theories were based on possible experimental artifacts, such as convection, or ion chamber design. One theory was that the Kr-He source mixture was not uniformly mixed at the higher pressures (the usual technique is to add Kr tracer and back fill with He to the desired pressure). Accordingly, run No. 18 was initiated after the Kr and He in the source tube were well mixed by thermal cycling (six times over a period of 2 hr).

Run 18 is a repeat of earlier experiments under the same conditions (runs 1 and 13) except that the source chamber was thermally cycled several times to ensure that the Kr was homogeneously mixed with the He

before opening the valve to initiate the diffusion experiment. The diffusion coefficient (D = 0.01156 sq cm/sec) for the SLIDER calculation of run No. 18 was obtained from the plot of diffusion coefficient versus pressure reported previously (Ref. 33). Excellent agreement of the experimental curve and points calculated using SLIDER was found as shown for run 18 in Fig. 4.10. This result shows that nonmixing was not responsible for the deviation of the measured diffusion coefficients from a linear relation with inverse pressure as previously reported.

Another explanation was that the test rig was operated in the upright position, and convective flow (which may be more important at higher pressures) could decrease apparent delay times. Runs 19 and 20, therefore, were performed with most of the void space filled with a 1/4-in.-diam metal rod extending the entire length of the diffusion tube to minimize convection loops in the tube. Although the purpose of the rod was to inhibit convection, the effects of geometry and convection are not clearly separable in the analysis of the experiment with the SLIDER computer program because it is one-dimensional. In this case, however, the length of the rod was 15.75 in.,compared to the tube inside diameter of 0.31 in.,and the entrance and exit effects should therefore be negligible and geometric and convection effects separable. The diffusion coefficient for the SLIDER calculation was selected from the D vs P curve provided by earlier experiments (Ref. 33) and then corrected by the ratio of the flow areas in the open and rod-filled tubes. The comparisons of the experimentally measured and SLIDER computed curves are shown as run 19 (1 atm) and run 20 (69 atm) in Fig. 4.10. The agreement between the computed and experimental curves is satisfactory. It is assumed that the geometric effects (end effects) other than the flow area reduction are negligible, and the results indicate that thermal convection cannot account for the divergence of the diffusion coefficient from a linear inverse pressure proportionality.

In a third explanation, anomalies in the ion chamber response versus Kr concentration and He pressure are assumed. It was theorized

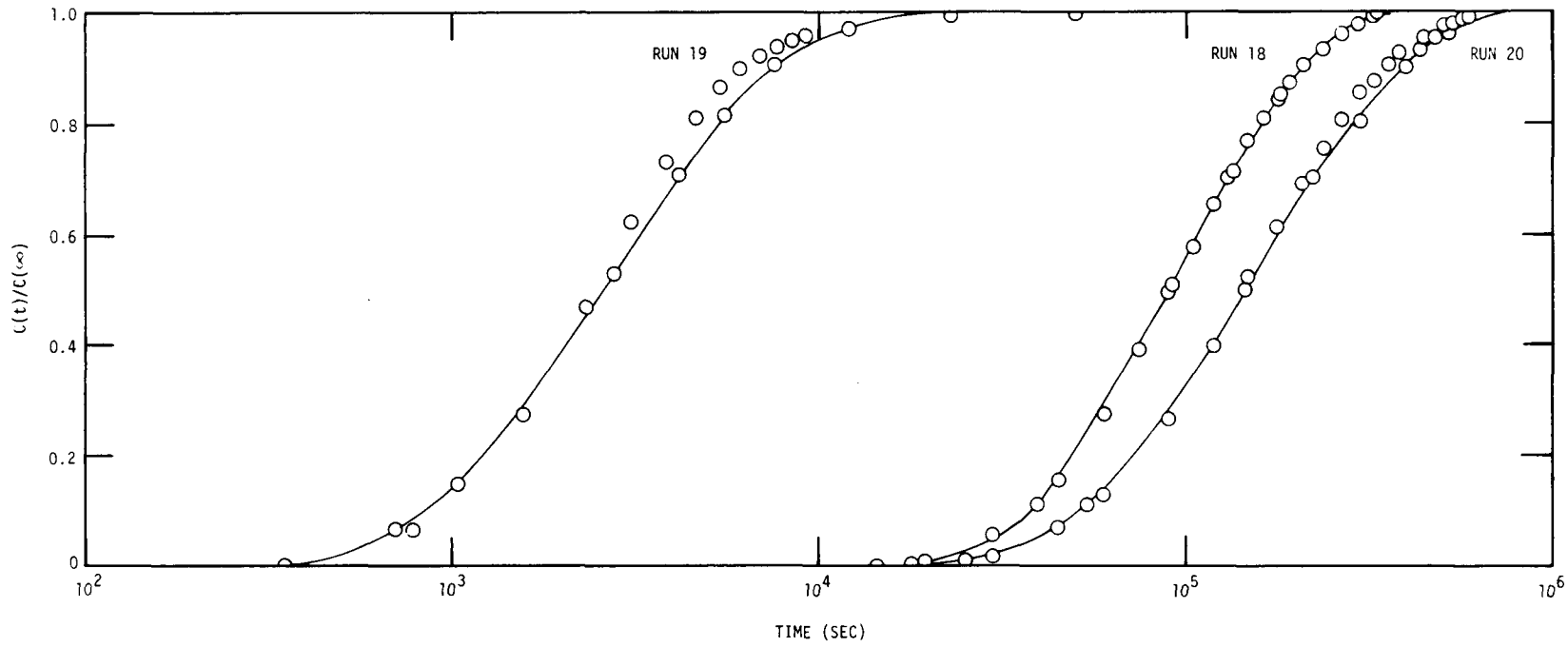

Fig. 4.10. Plot of ratio of Kr concentration in the ion chamber (of diffusion experiment rig) to that in the chamber after equilibrium has been reached as a function of time for runs 18-20

that the ion current may not be linear with Kr concentration due to ion pair recombination or other possible effects (since this chamber was specially designed and fabricated for these tests). Accordingly, a complete calibration of the ion chamber was performed. The data are given in Figs. 4.11 through 4.15. Figures 4.11 through 4.14 show that the ion chamber response is essentially linear with Kr concentration, while Fig. 4.15 shows that He pressure causes a nonlinear increase in ion current. This nonlinear effect has been observed previously and should not alter the results of the diffusion tests because the ion current data are reported in relation to the final equilibrium ion current, that is, C/C_{max}. Furthermore, since each test is run at a specific, constant pressure, the nonlinearity should have no bearing on the outcome of the experimental data.

Although the above results tend to rule out experimental artifacts caused by erratic ion chamber behavior, there still remains doubt as to the validity of the analytic approach for a static system whose ion chamber volume constitutes a major fraction of the total volume. Accordingly, tests have been initiated using a 6-ft-long diffusion tube. It is anticipated that volume effects of the ion chamber should be negligible in the tube with the longer diffusion path. Moreover, the 6-ft apparatus is positioned horizontally, thereby minimizing convective flow. These tests are underway and the results will be reported in the next quarterly.

4.5.4.3. Analysis of Kr Diffusion Experiments. Analysis of the Kr diffusion experiments is being conducted using the SLIDER computer program. In the previous quarterly report (Ref. 33) the results of analyses of diffusion of Kr in gas-filled tubes were reported. In the current report period, diffusion of Kr in tubes partially filled with fuel pellets, blanket pellets, and charcoal traps was analyzed using a stepwise procedure. First diffusion coefficient results from the He filled tubes were compared with the results of other investigators and with theoretical equations in the literature. These coefficients were then applied to the gas-filled regions of tubes, which, in addition, contained regions loaded with metal pellets simulating either fuel or blanket pellets

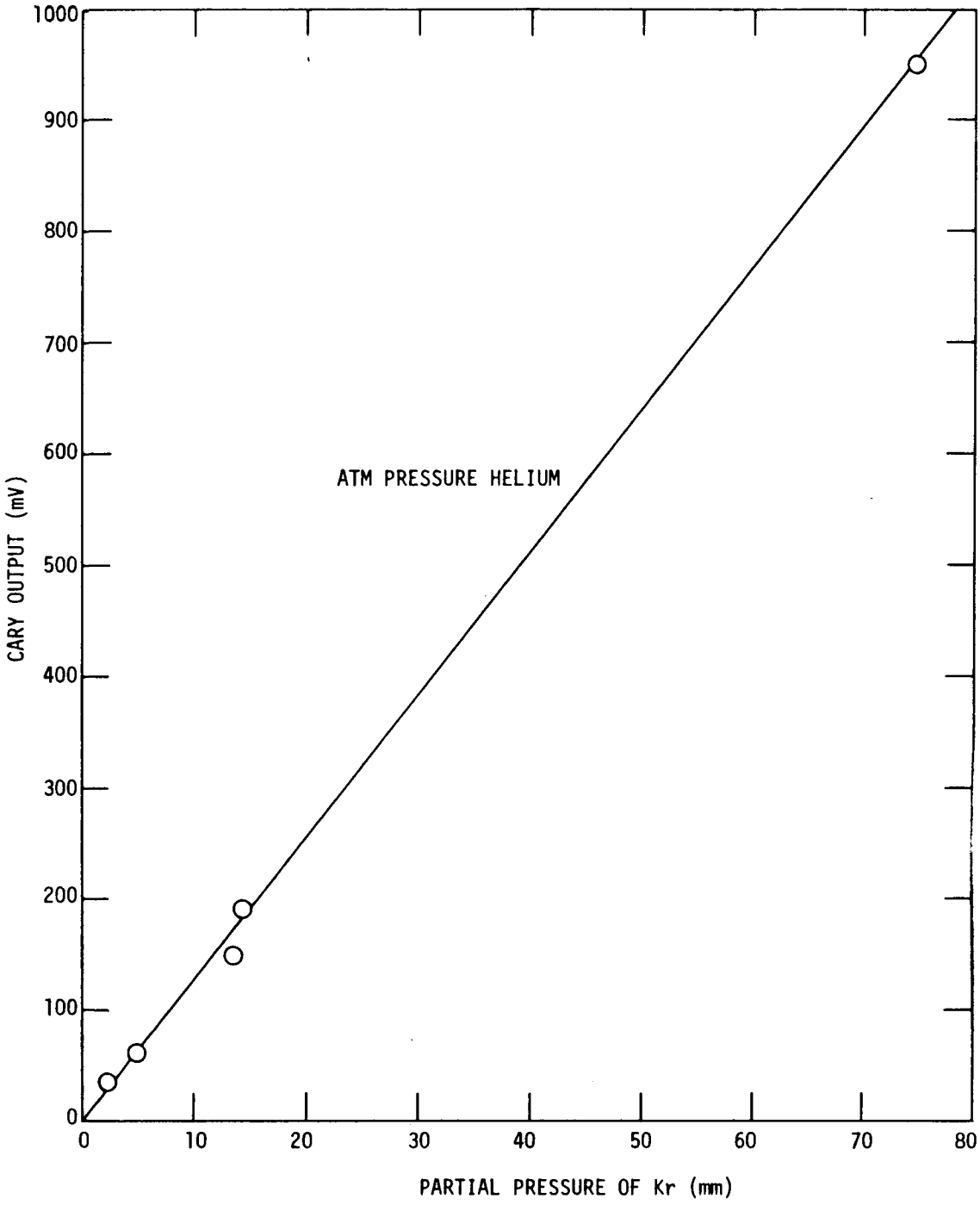

Fig. 4.11. Cary output vs Kr pressure at 1atm He

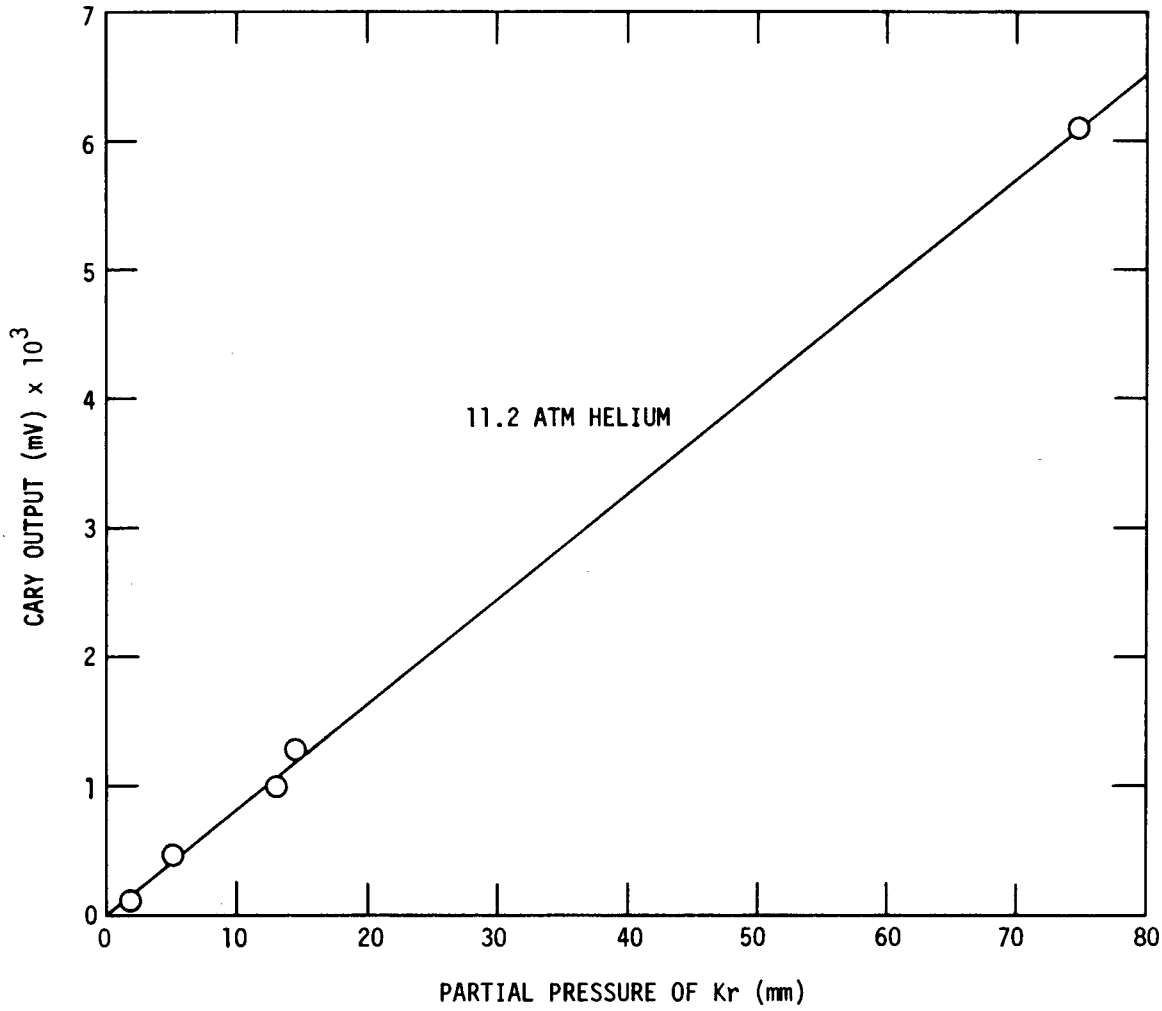

Fig. 4.12. Cary output vs Kr pressure at 11.2 atm He

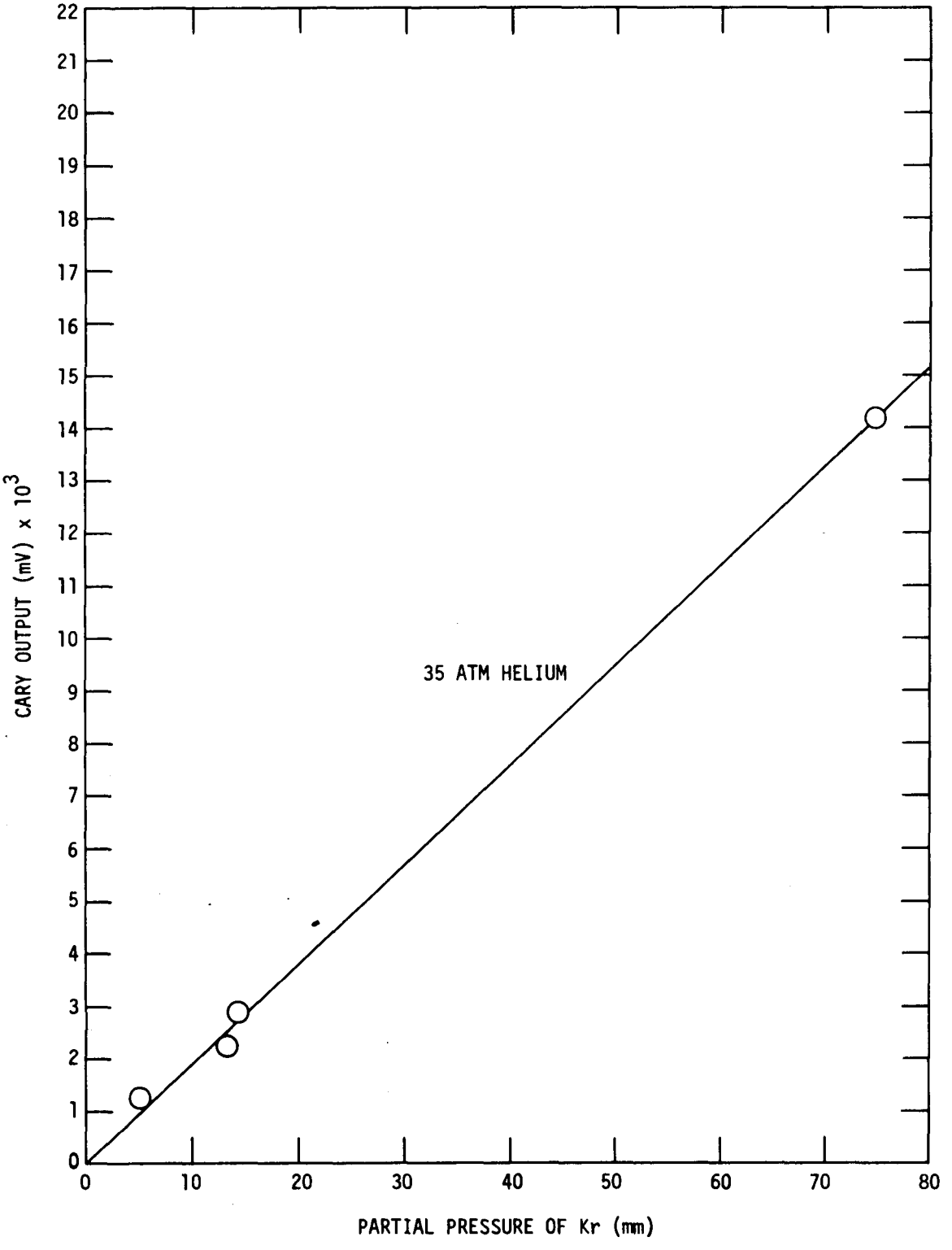

Fig. 4.13. Cary output vs Kr pressure at 35 atm He

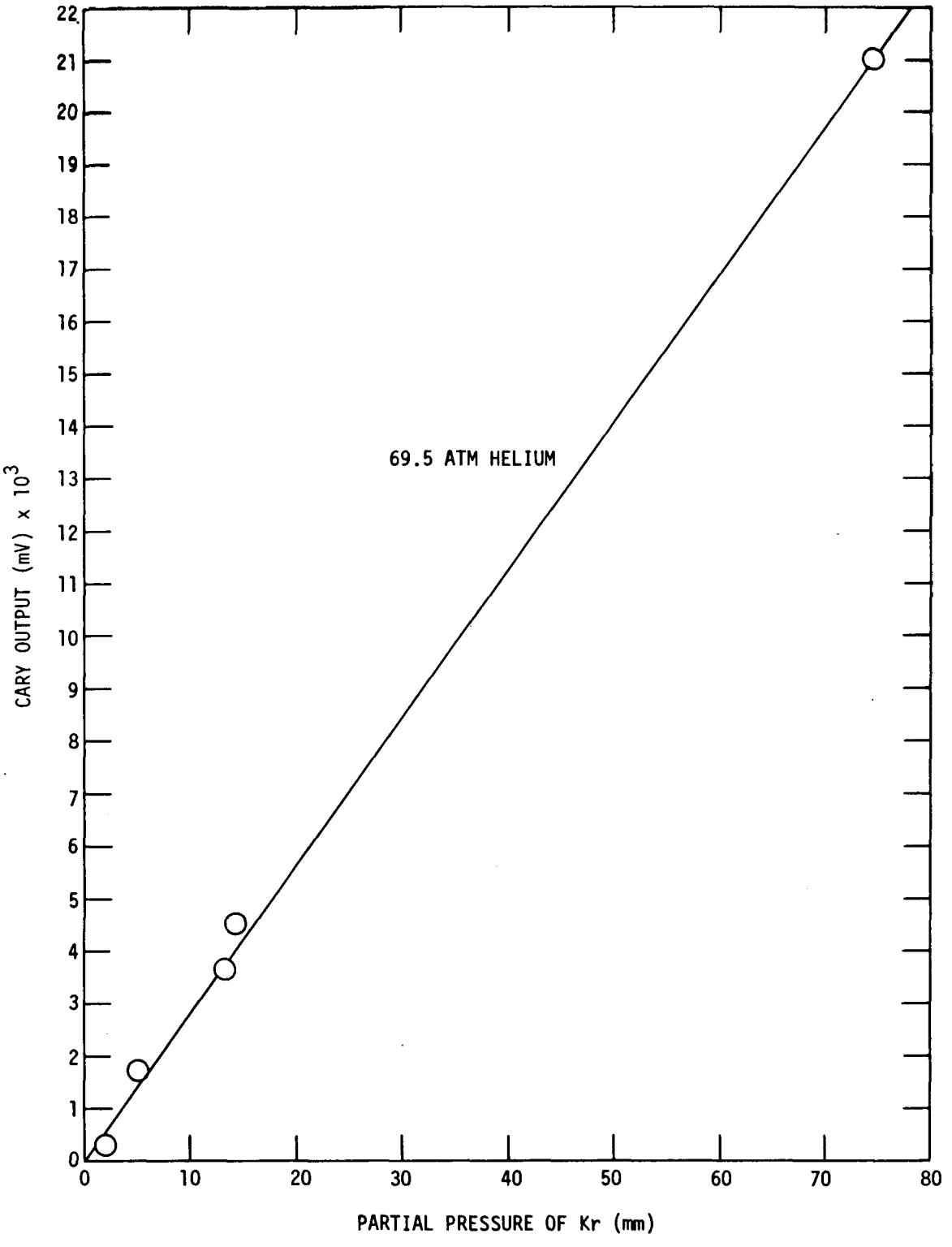

Fig. 4.14. Cary output vs Kr pressure at 69.5 atm He

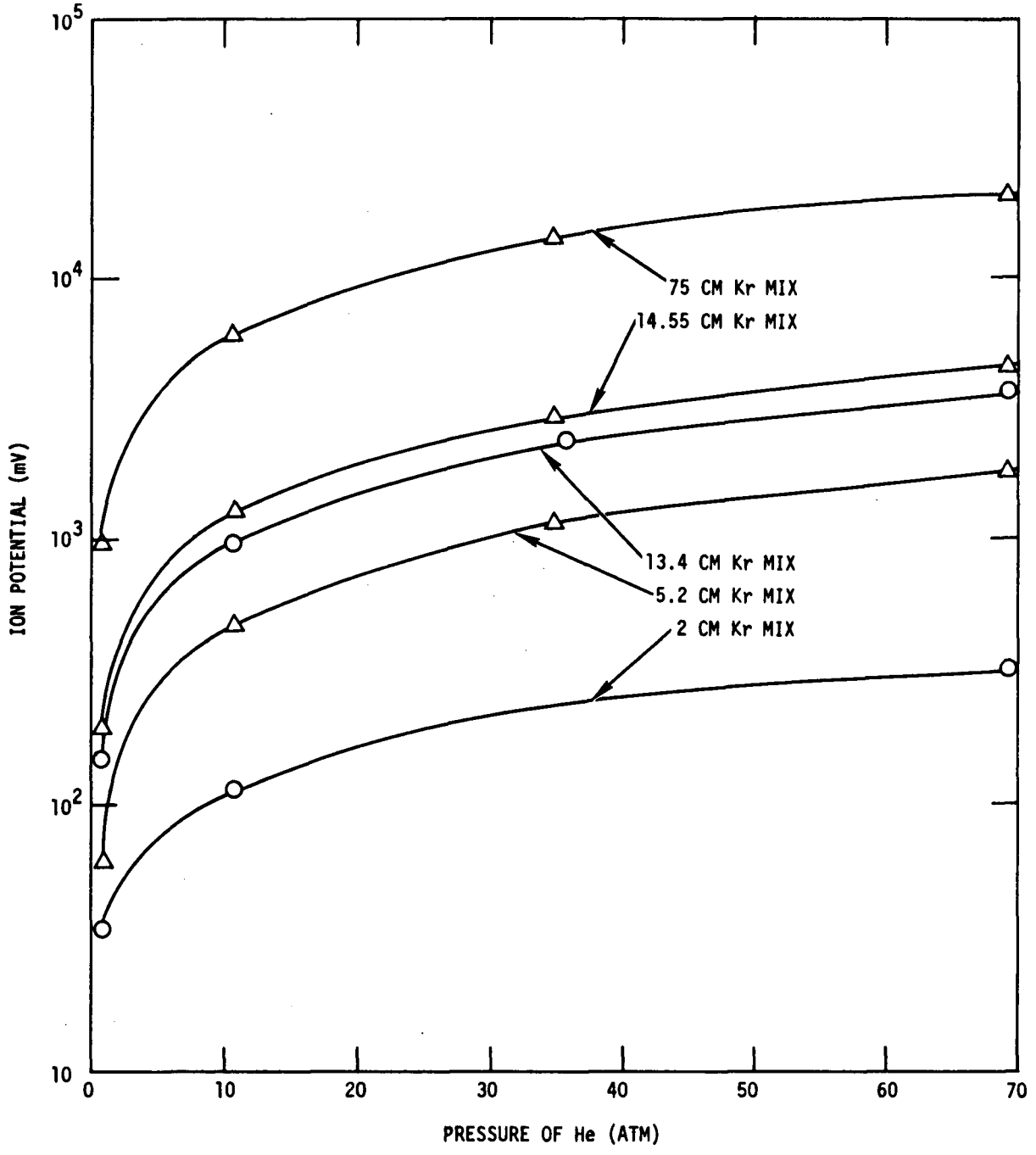

Fig. 4.15. Ion chamber pressure vs ion potential (mV) at various Kr concentrations in GCFR diffusion rig

and permitted determination of the diffusion coefficients in these regions. Finally, all of the data previously obtained were applied to tubes also containing charcoal traps, which allowed determination of the effectiveness of the trap on the diffusion process. Results of the diffusion experiments and the computer simulation of each group of experiments are shown in Figs. 4.16 through 4.18.

The results obtained from the analysis of gas-filled tubes were previously reported (Ref. 33). Values found were in good agreement with theoretical equations and slightly higher than measurements at atmospheric pressure made by other investigators. A deviation from the expected inverse proportionality of the diffusion coefficient with pressure was noted at pressures above 15 atm and amounted to 20% at 70 atm.

Analytical results from runs 5 through 8 are reported in Table 4.9. In the analysis of these runs, with tubes partially filled with fuel or blanket pellets or both,the diffusion coefficients in the gas-filled tube regions were those determined in the analysis of the earlier runs. By analysis of runs 6 through 8, the effective diffusion coefficient through the blanket regions and pellet-can gap was determined, and, in the analysis of run 5, the effective diffusion coefficient through the combined central fuel-pellet hole and fuel-pellet-can gap was found. Run 5 contained both blanket and fuel pellets, so the diffusion coefficient for the blanket region determined in run 6 was used in the analysis of run 5.

Since SLIDER is a one-dimensional program, the effective diffusion coefficient D_e in the hole and annular gap may be expressed

$$D_e = \frac{D_m}{G} ,$$

where D_m is the molecular diffusion coefficient (gas-filled tube) and G is a geometrical factor which simulates the two-dimensional effects. The flow area ratio of the open to partially blocked tube (AR) may be

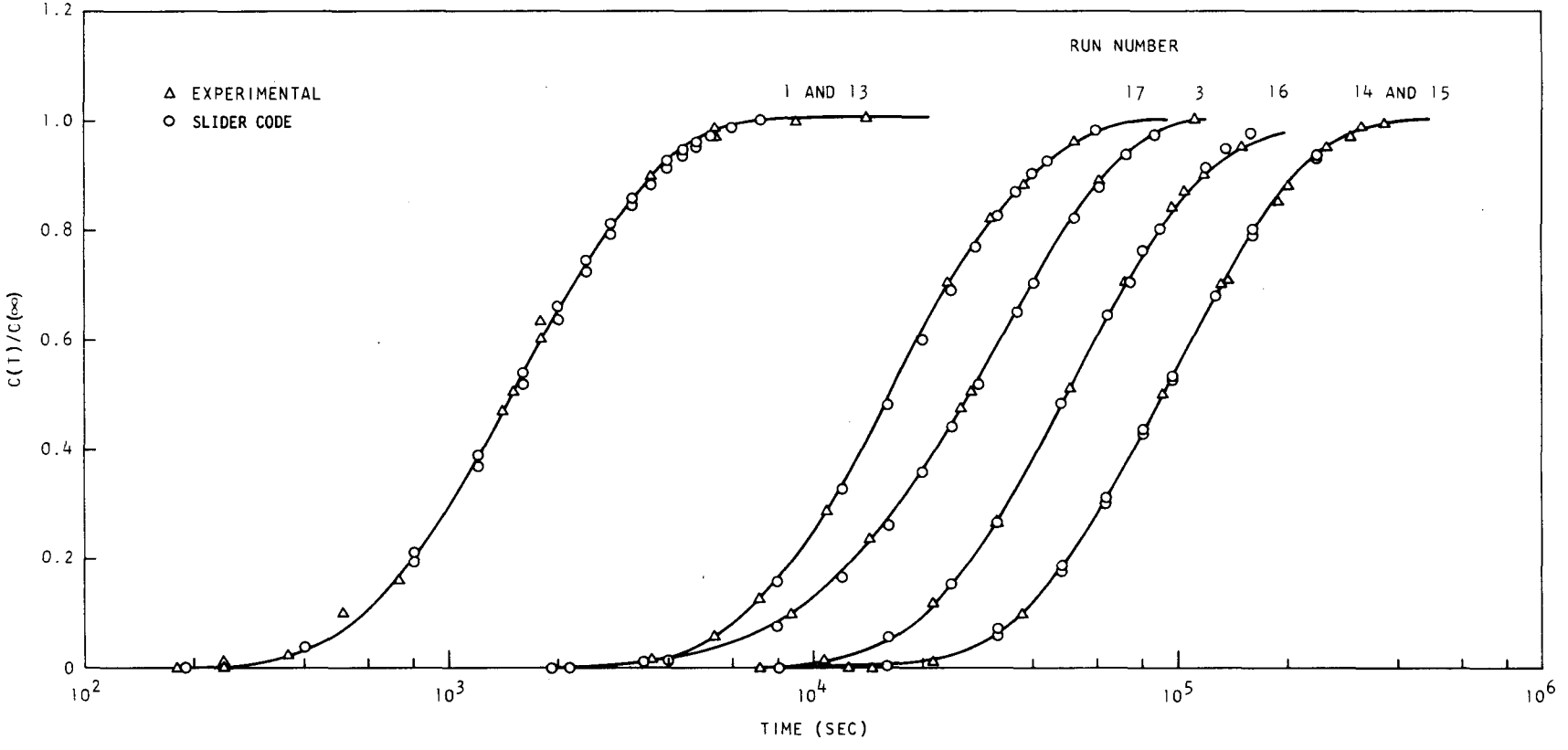

Fig. 4.16. Plot of ratio of Kr concentration in the ion chamber (of diffusion experiment rig) to that in the chamber after equilibrium has been reached as a function of time for runs 1, 3, and 13-17

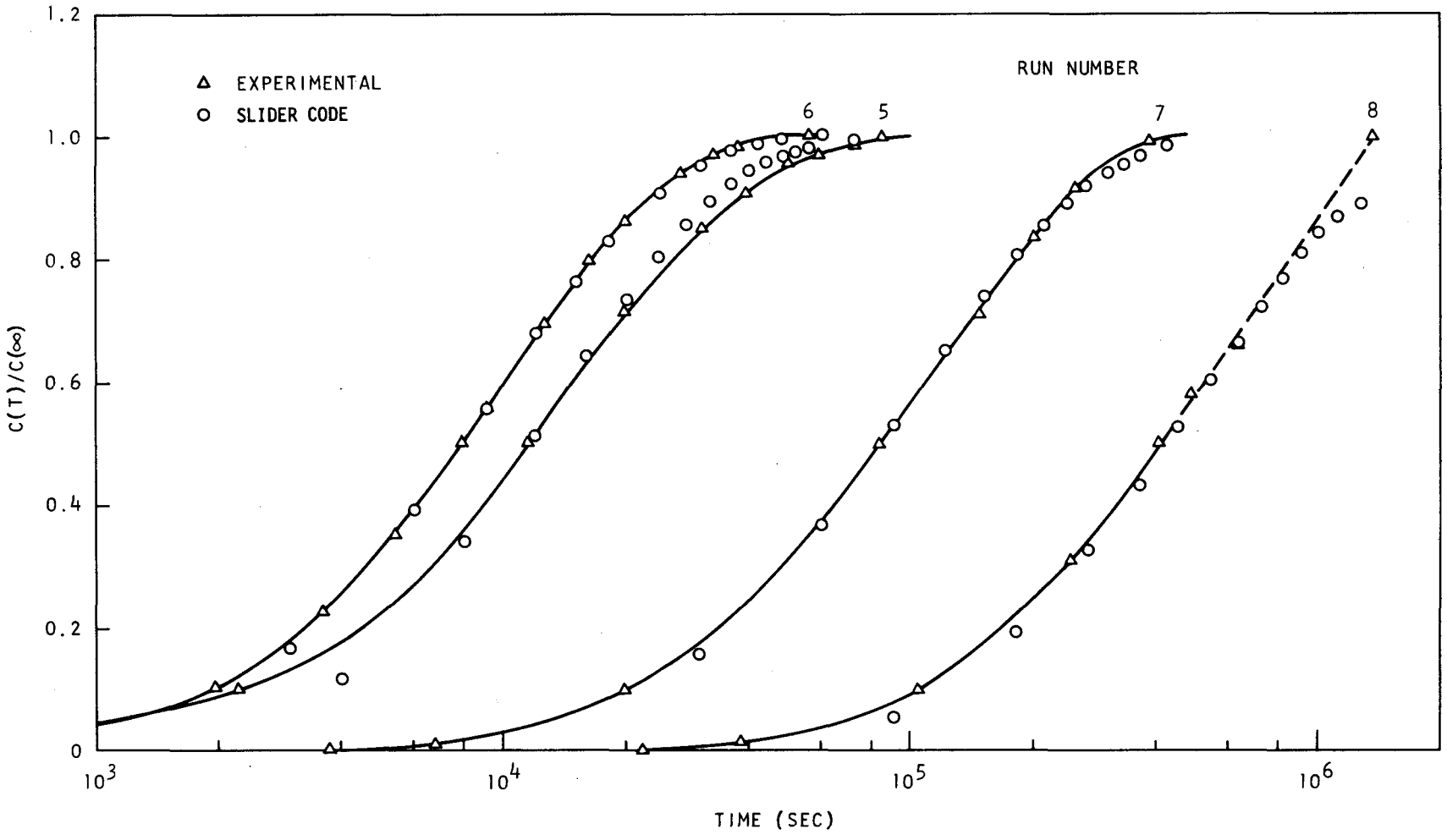

Fig. 4.17. Plot of ratio of Kr concentration in the ion chamber (of diffusion experiment rig) to that in the chamber after equilibrium has been reached as a function of time for runs 5-8

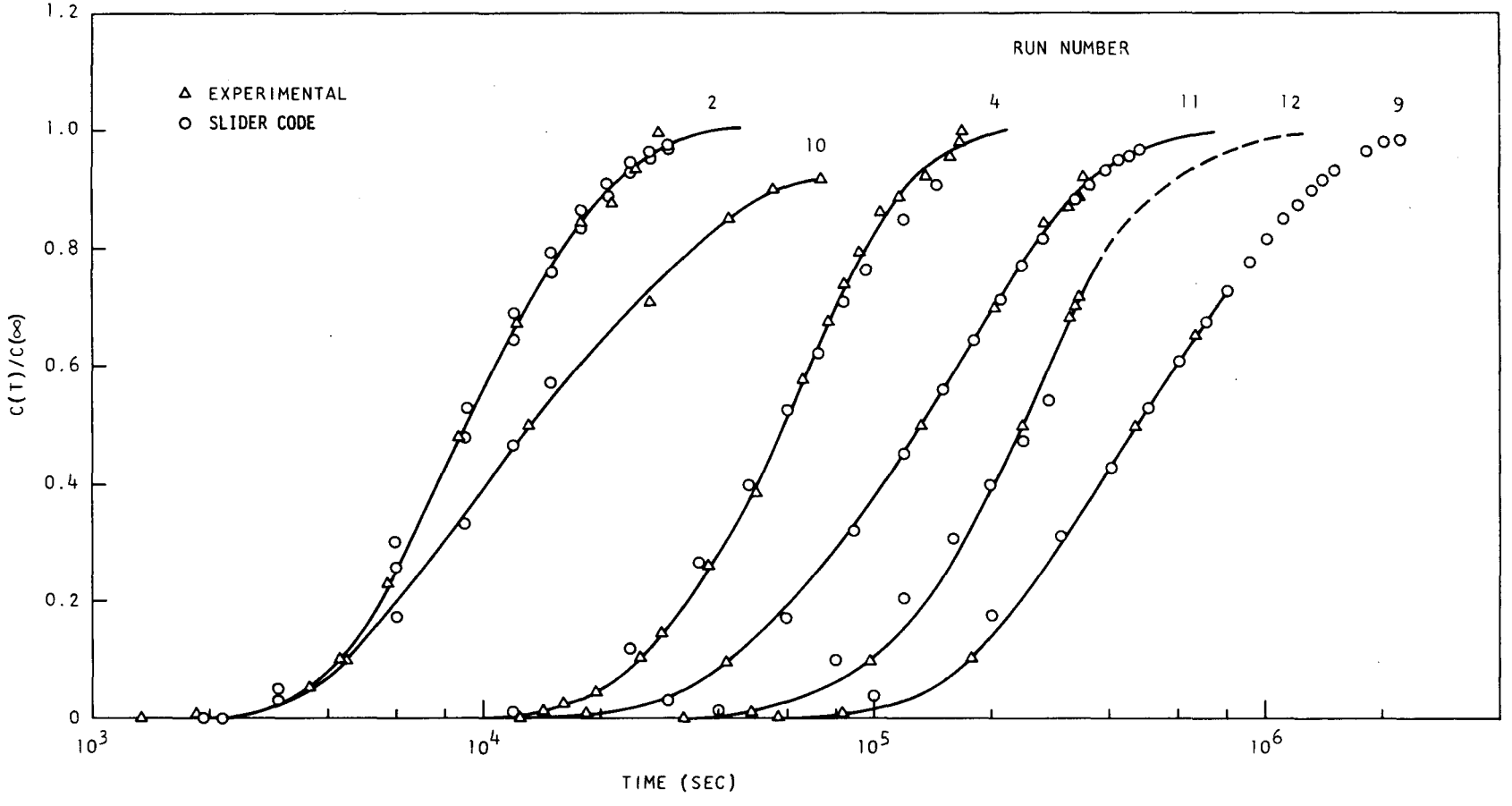

Fig. 4.18. Plot of ratio of Kr concentration in the ion chamber (of diffusion experiment rig) to that in the chamber after equilibrium has been reached as a function of time for runs 2, 4, and 9-12

TABLE 4.9

EFFECTIVE Kr-He DIFFUSION COEFFICIENTS IN FUEL AND BLANKET REGIONS

Run No.	Region of Interest	Pressure (atm)	D(R)[a] (sq cm/sec)	Area Ratio, AR	Geom. Factor, G	Geom./ Area, G/AR
5	Fuel	1.0	6.80×10^{-2}	21.0	9.78	0.465
6	Blanket	1.0	1.55×10^{-2}	77.0	42.9	0.556
7	Blanket	11.0-11.2	1.45×10^{-3}	77.0	41.3	0.535
8	Blanket	66.0-69.5	2.94×10^{-4}	77.0	33.25	0.433

[a] D(R) - Effective diffusion coefficient in the region of interest.

separated from G, leaving a second geometry factor G/AR not based on area (e.g., the longer flow path associated with the convergence and divergence of the current paths at the entrace and exit to the partially blocked region and the longer path caused by the offset from pellet-to-pellet in the gap). As shown in the table this second factor seems to be approximately 0.5 regardless of whether the regions are occupied by fuel or blanket pellets, even though the area ratios are quite different. Also, there appears to be a slight pressure dependence among the G/AR values derived for the blanket region that may be related to relative dimensions of the mean-free-path between molecular collisions and the channel (i.e., wall effects). On the other hand, the overall dependence of D_e on pressure is essentially the same as that found in the gas-filled tube runs.

Analytical results from runs 2, 4, 9, 10, 11 and 12 bases on an equivalent volume model of the charcoal trap are shown in Table 4.10.

The equivalent volume model of the trap is based on a heuristic approach. Since the charcoal adsorbs Kr molecules in the gas phase of the trap, the effect of the trap is to reduce the concentration of Kr in the trap region of the diffusion path. An added volume in the diffusion path at the same location as the trap will simulate the same qualitative relationships. Since the mean-free-path between molecular collisions is very small compared to the dimensions of the system, even in the charcoal bed, access to the equivalent volume region in the model or the charcoal in the experiment are approximately equal. Only the volume of the model must be adjusted to match the trap adsorption.

Using this model, the SLIDER code was used to compute (1) the time of arrival of the concentration front at the detector and (2) the correct concentration-front shape.

TABLE 4.10

CHARCOAL TRAP PERFORMANCE

Run No.	Pressure (atm)	Effective Diffusion Coefficient[a] (sq cm/sec)	Equilvalent Volume/ Trap Volume	Other Diffusion Regions
2	1.0	3.70×10^{-1}	9.67	Empty
4	10.8	3.43×10^{-2}	4.59	Empty
10	1.0	3.70×10^{-1}	6.56	Blanket
11	11.2	3.47×10^{-2}	6.31	Blanket
12	35.0	1.20×10^{-2}	2.50	Blanket
9	69.5	5.33×10^{-3}	2.00	Blanket

[a] The effective diffusion coefficient in the charcoal trap was taken to be

$$D'_e = \frac{D_m}{TP},$$

where

D_m = molecular diffusion coefficient (from previous experiments)

T = tortuosity factor = 1.8

p = pressure

Other analytical approaches have been tried but have failed. These include:

1. Use of a simple effective diffusion coefficient for the trap region

2. The treatment of the trap as a homogeneous region with an effective diffusion coefficient and a boundary solution factor to simulate adsorption in the bed

3. The use of a negative source (sink) to simulate adsorption in the trap

4. The use of an effective decay constant to simulate the decreased gas phase concentration caused by adsorption

The results from these approaches were unsatisfactory.

Considering the equivalent volume model, it is only possible in a one-dimensional program such as SLIDER to change the volume by changing the length. However, changing length also changes the diffusion path length, whereas a change in the cross-sectional area is what is desired. For this reason the equivalent volume model may be considered an equivalent length model, and the results obtained may only be considered to be empirical. The performance of a trap of different diameter probably cannot be predicted from these results. An equivalent volume model using the FIPER-2 code may produce more generally useful results since it is a two-dimensional program.

The results given in Table 4.10 and those previously reported (Refs. 33, 35) are applicable to the GA-20 fuel rod being installed in capsule 04P9. Revised release fractions can now be calculated for Kr isotopes and for Xe everywhere except in the trap, where Xe adsorption has not been measured. Additional experiments and analyses will be defined to provide this information

4.5.5. Fast Flux Irradiation

The detailed analysis of several configurations of the B-7 core subassembly is continuing. Each capsule will contain one $(Pu,U)O_2$-fueled rod clad in 316 stainless steel, which will simulate a manifolded rod operating at nominal GCFR demonstration plant conditions: an average burnup of approximately 50,000 MWd/Te, heat generation rates of approximately 15 kW/ft, and a maximum cladding temperature of 650 C to 750 C. A test program is being arranged to provide the most efficient use of reactor test space, while providing a reasonable parametric evaluation of anticipated GCFR conditions.

The standard B-7 core subassembly was chosen as a design basis because it provided space within each capsule for a thermal barrier to raise cladding temperatures. The configurations to be examined are the standard materials irradiation subassembly with individual capsules touching, the wire-wrapped capsules, and a shroud tube configuration, as in the A-19 core subassembly. The first is the most preferable and the last the least because progressively less internal space in the capsule is available. The detailed analysis is being carried out on the standard materials subassembly and the wire-wrapped capsule subassembly (Figs. 4.19a and 4.19b) using a 0.300-in. o.d. cladding. Radial temperature distribution calculations, taking into account the axial flux and coolant temperature variations, indicate that peak clad temperatures of up to 800 C can be achieved in the 62.5 MW core in row 7 of the EBR-II core with a somewhat lower cladding temperature for the wire wrap capsule subassembly because of a thinner thermal barrier. These calculations are not in their final form, but the peak temperatures indicated are not expected to change significantly.

The annular mixed-oxide fuel pellet will be surrounded by 316 stainless steel cladding using an He fuel-cladding bond. The cladding will have a 0.020-in. Na bond to the thermal barrier i.d. The thermal barrier will be a relatively thick tube of 304 stainless steel with deep radial slots to eliminate thermally induced circumferential stresses. Zircaloy is

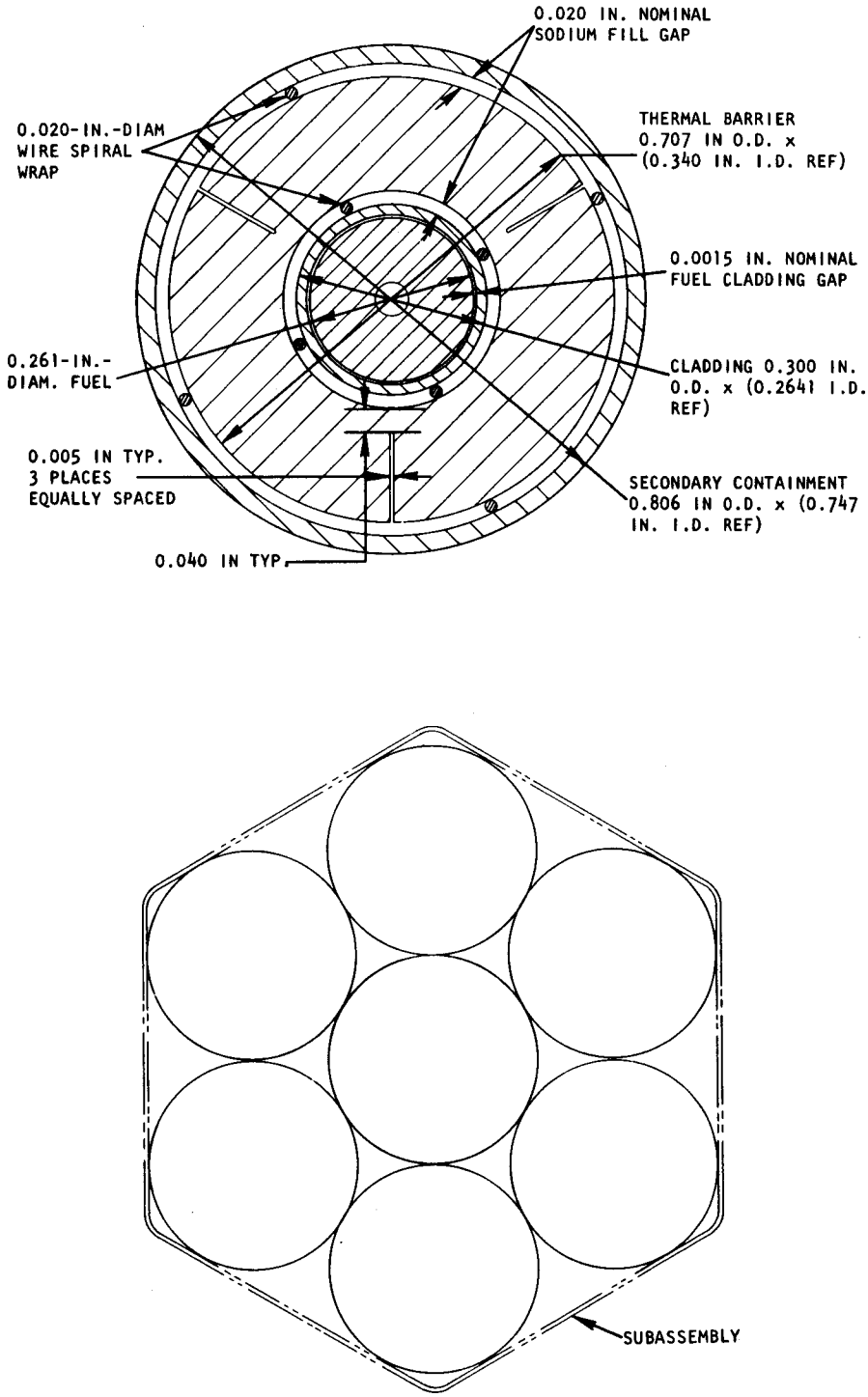

Fig. 4.19a. Illustration of the standard materials irradiation B-7 subassembly design with individual capsules touching

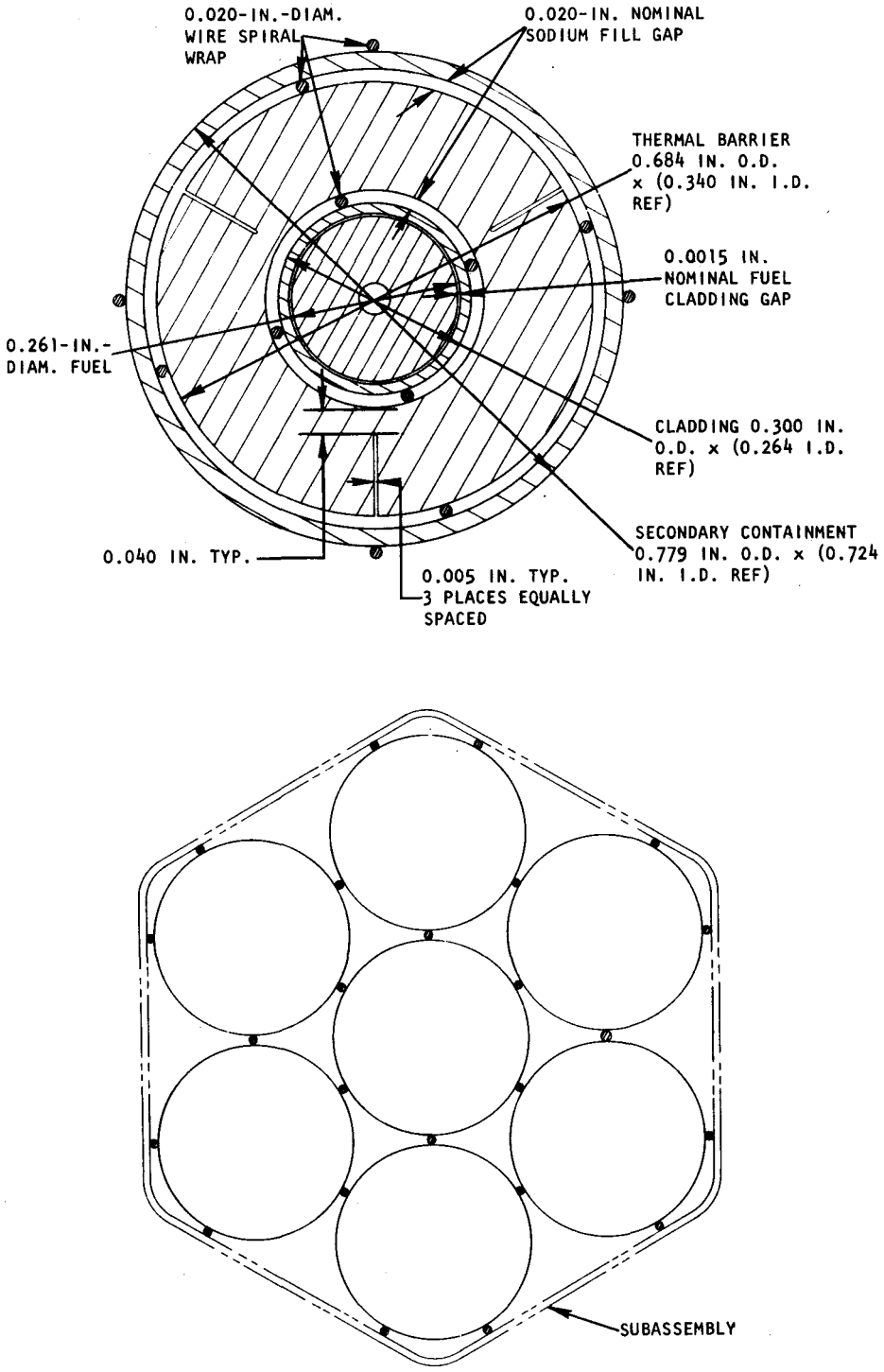

Fig. 4.19b. Illustration of wire-wrapped capsule design for B-7 subassembly

another thermal barrier candidate and offers the advantage of about 10% less thermal conductivity, and several successful GGA irradiations in the ORR have used these thermal barriers. The initial design effort will use 304 stainless steel rather than Zircaloy, which has about one-half the coefficient of expansion of 304 stainless steel. Other forms of thermal barrier were considered that would have the advantage of being thinner; however, these forms would have required a development program or would have used materials with an uncertain irradiation behavior. Another 0.020 Na bond will be located between the thermal barrier o.d. and the capsule i.d. The general axial layout of the capsule is shown in Fig. 4.20 and is not expected to vary significantly in the three radial configurations under consideration. Circumferential hot-spot calculations have not been done in detail; however, preliminary examination of the standard B-7 core subassembly at the capsule o.d. indicates only a 26 F temperature variation. If this 26 F variation is not exceeded in the more detailed calculations the standard design should be satisfactory, and there should be no significant hot-spot effect on an adjacent subassembly.

Preliminary discussions have been held with Atomics International to consider a cooperative effort in which two 50 kW/ft carbide rods would be irradiated to about 20,000 MWd/Te. The effect of 2 rods with this rating on the subassemblies under consideration will have to await the conclusion of the detailed calculations in mid-September. It is planned to submit a letter requesting approval in principal for EBR-II irradiation of the seven fuel rods in the B-7 capsule subassembly during the latter part of September.

Preliminary physics analysis of the experimental subassembly to be irradiated in the EBR-II facility has been made. Fig. 4.21 is a plan view of this 91-subassembly core (Ref. 36).

4.5.5.1. Linear Rating. If gamma heating is neglected, the linear rating λ may be calculated as a function of position by use of the formula

$$\lambda(r,z) = 26.97\ R^2 \sum_i \rho_i\ (r)\ f_i\ (r,z)\ \text{kW/ft}\quad ,$$

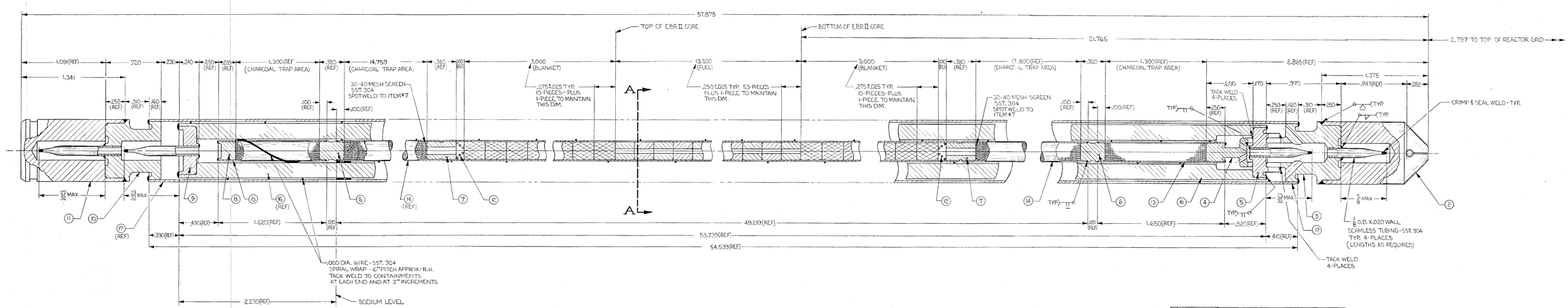

REQUIRED	ITEM	PART NO.	DESCRIPTION	MATL	MATL SPEC
			LIST OF MATERIAL		
1	17		OUTER CONTAINMENT	SST.	304
1	16		SHIELD TUBE	SST.	304
1	15		CLAD - 1.620 LONG	SST.	316
1	14		CLAD - 4½ 2/3 LONG	SST.	316
1	13		CLAD - 1.620 LONG	SST.	316
12	12		SPRING	INCONEL	718
1	11		PAWL END	SST.	304
1	10		ADAPTOR-OUTER CONTAINMENT-TOP	SST.	304
1	9		PLUG - SHIELD TUBE	SST.	304
1	8		CAP-TOP - CLAD	SST.	316
3	7		SPACER PLUG - CLAD	SST.	316
2	6		SPACER CAP-CLAD	SST.	316
1	5		PEDESTAL - SHIELD TUBE	SST.	304
1	4		STANDOFF PLUG - CLAD	SST.	316
1	3		ADAPTOR - OUTER CONTAINMENT - BOTTOM	SST.	304
1	2		TIP ELEMENT	SST.	304
X	1	-1	ASSEMBLY		

Fig. 4.20. Design of fast-flux irradiation assembly

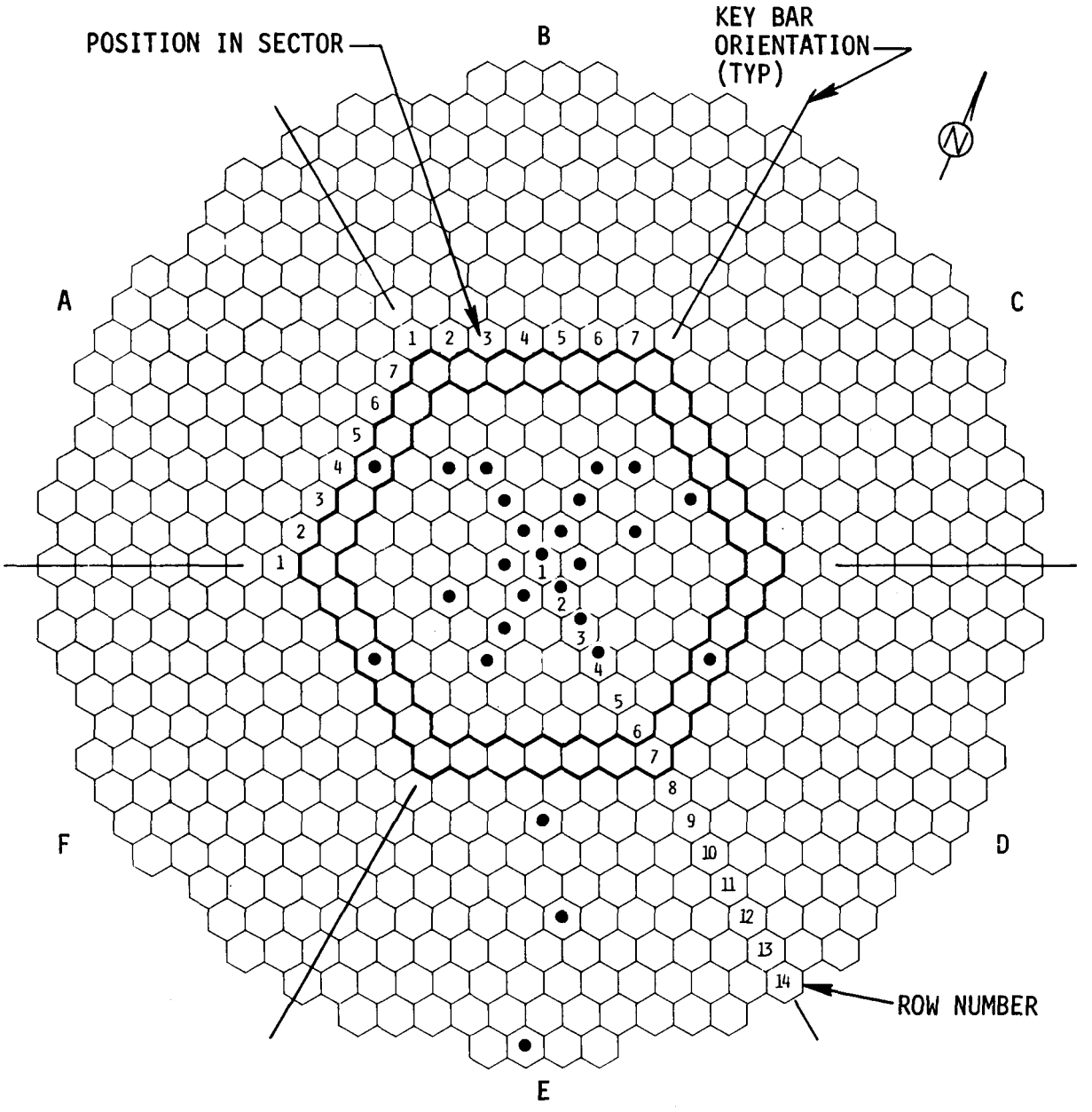

1. SECTORS DESIGNATED BY A THROUGH F
2. CONTROL AND SAFETY RODS SHOWN IN HEAVY BLACK LINE
3. THERMOCOUPLE LOCATIONS SHOWN BY BLACK DOT IN GRID POSITION
4. GRID POSITIONS

CORE	91
INNER BLANKET	36
OUTER BLANKET	510

Fig. 4.21. Plan view of 91 subassembly core

where R = fuel pin radium (cm)

ρ_i = density of isotope i (g/cc)

f_i = fission rate in isotope i (f/g-sec x 10^{13})

This formula is based upon the suggested value (Ref. 36) of 3.55 x 10^{10} f/W-sec. In all calculations, the density ρ was assumed to be 85% of theoretical and the isotopic distribution is shown in Table 4.11.

TABLE 4.11

ISOTOPIC DISTRIBUTION OF URANIUM AND PLUTONIUM

Uranium		Plutonium	
U-235	0.93	Pu-239	0.886
U-238	0.07	Pu-240	0.099
		Pu-241	0.014
		Pu-242	0.001

The fission of the minor Pu isotopes was approximated by increasing the Pu-239 density by a factor

$$\frac{\sum_j y_j \sigma_f^j}{y_{239} \sigma_f^{239}} ,$$

where y = isotopic abundance

σ_f = one group microscopic fission cross section averaged over a GCFR spectrum

and the summation extends over the four Pu isotopes. For the composition listed above, this factor is 1.052.

The appropriate values of f(r,o) for various core positions are listed in Table 4.12, a revision of the values given in Table V of Ref. 36. Figures 4.22 through 4.25 present $\lambda(r,o)$ as a function of power level, pin size, and azimuthal location for rows 4 through 7. Figure 4.26 is a plot of $\lambda(r,o)_{max}$ as a function of core radius for a typical B-19 core subassembly

TABLE 4.12

RADIAL FISSION DISTRIBUTIONS AT REACTOR MIDPLANE
FOR THE 91 SUBASSEMBLY CORE WITH A DEPLETED RADIAL BLANKET
(FISSIONS PER GRAM-SECOND OF ISOTOPE AT 50 MW)

DISTANCE REACTOR CENTER-LINE TO CENTER-LINE OF SUBASSEMBLY (CM)	GRID POSITION N = GRID SECTOR LETTER	PIN NEAREST CORE CENTERLINE — MAXIMUM PIN			PIN IN CENTER OF SUBASSEMBLY — AVERAGE PIN			PIN FARTHEST FROM CORE CENTERLINE — MINIMUM PIN		
		U-235 $X10^{-13}$	U-238 $X10^{-12}$	Pu-239 $X10^{-13}$	U-235 $X10^{-13}$	U-238 $X10^{-12}$	Pu-239 $X10^{-13}$	U-235 $X10^{-13}$	U-238 $X10^{-12}$	Pu-239 $X10^{-13}$
0.0	1N1	0.926	0.642	1.120	0.926	0.642	1.120	0.921	0.625	1.114
5.89	2N1	0.917	0.604	1.108	0.909	0.594	1.098	0.898	0.615	1.086
10.21	3N2	0.900	0.602	1.090	0.883	0.609	1.069	0.859	0.574	1.033
11.78	3N1	0.888	0.611	1.076	0.869	0.594	1.049	0.841	0.553	1.010
15.59	4N2	0.852	0.569	1.026	0.815	0.529	0.980	0.773	0.502	0.930
15.59	4N3	0.852	0.569	1.026	0.815	0.529	0.980	0.773	0.502	0.930
17.68	4N1	0.817	0.530	0.982	0.780	0.506	0.942	0.741	0.482	0.889
20.41	5N3	0.777	0.504	0.936	0.732	0.476	0.877	0.684	0.432	0.811
21.25	5N2	0.761	0.496	0.917	0.716	0.462	0.855	0.669	0.419	0.795
21.25	5N4	0.761	0.496	0.917	0.716	0.462	0.855	0.669	0.419	0.795
23.57	5N1	0.714	0.460	0.852	0.669	0.421	0.795	0.622	0.372	0.732
25.69	6N3	0.679	0.429	0.803	0.625	0.373	0.738	0.569	0.294	0.663
25.69	6N4	0.679	0.429	0.803	0.625	0.373	0.738	0.569	0.294	0.663
27.00	6N2	0.648	0.400	0.765	0.595	0.332	0.700	0.542	0.238	0.622
27.00	6N5	0.648	0.400	0.765	0.595	0.332	0.700	0.542	0.238	0.622
29.46	6N1	0.589	0.321	0.688	0.539	0.237	0.617	0.482	0.151	0.536
30.62	7N4	0.572	0.295	0.663	0.509	0.188	0.575	0.440	0.113	0.479
31.18	7N3	0.557	0.269	0.638	0.495	0.174	0.552	0.424	0.102	0.463
31.18	7N5	0.557	0.269	0.638	0.495	0.174	0.552	0.424	0.102	0.463
32.81	7N2	0.513	0.197	0.576	0.449	0.123	0.495	0.380	0.072	0.411
32.81	7N6	0.513	0.197	0.576	0.449	0.123	0.495	0.380	0.072	0.411
35.36	7N1	0.436	0.113	0.479	0.376	0.071	0.404	0.321	0.047	0.339
35.84	8N4	0.433	0.109	0.478	0.362	0.065	0.390	0.303	0.041	0.315
35.84	8N5	0.433	0.109	0.478	0.362	0.065	0.390	0.303	0.041	0.315
36.80	8N3	0.405	0.087	0.444	0.338	0.052	0.356	0.282	0.035	0.288
36.80	8N6	0.405	0.087	0.444	0.338	0.052	0.356	0.282	0.035	0.288
38.64	8N2	0.351	0.059	0.370	0.296	0.039	0.305	0.246	0.026	0.253
38.64	8N7	0.351	0.059	0.370	0.296	0.039	0.305	0.246	0.026	0.253
41.25	8N1	0.285	0.036	0.298	0.239	0.025	0.244	0.200	0.007	0.198

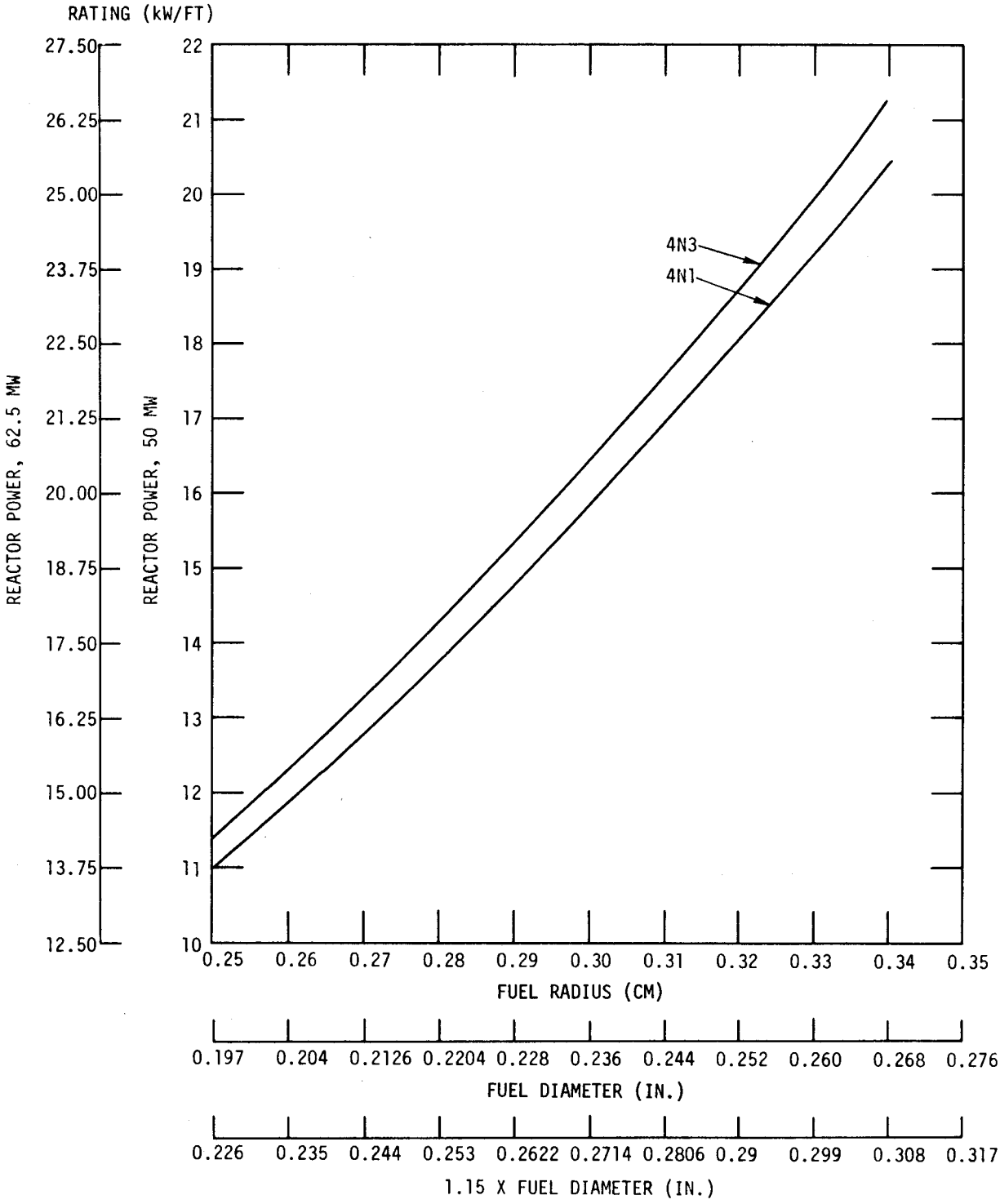

Fig. 4.22. $(Pu,U)O_2$ fuel rod linear heat rating as a function of EBR-II reactor power level, rod size, and azimuthal location in row 4

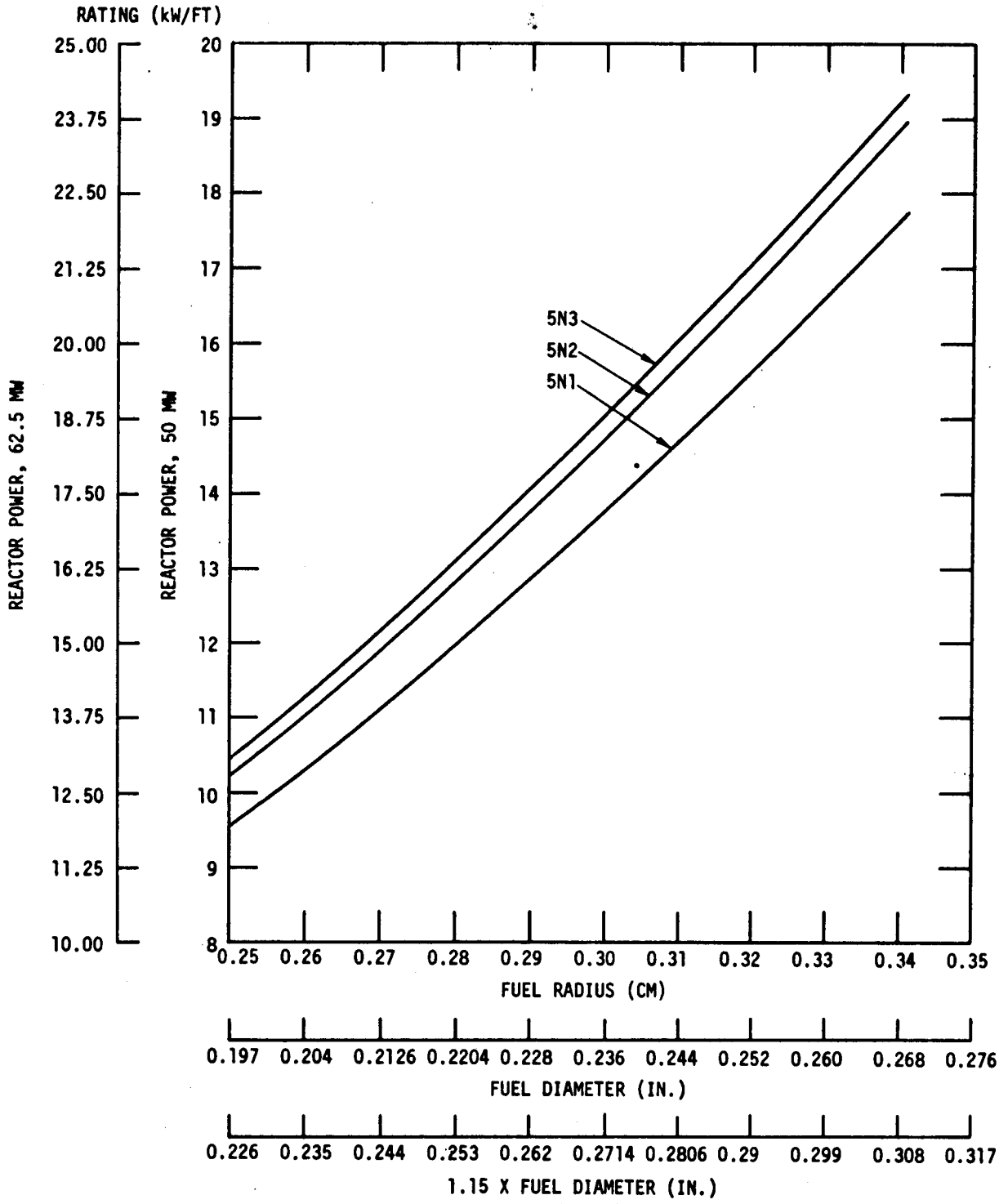

Fig. 4.23. $(Pu,U)O_2$ fuel rod linear heat rating as a function of EBR-II reactor power level, rod size, and azimuthal location in row 5

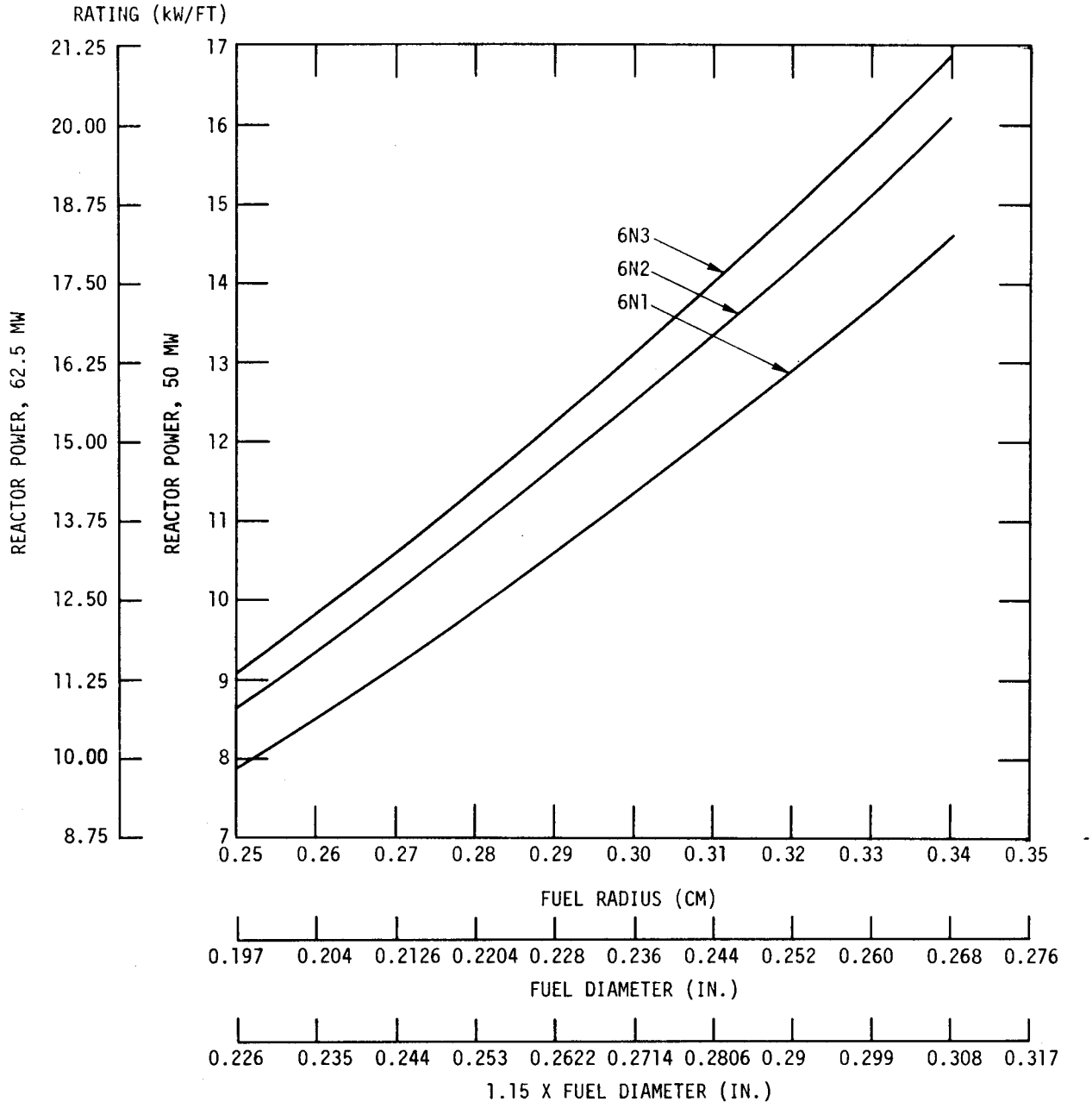

Fig. 4.24. $(Pu,U)O_2$ fuel rod linear head rating as a function of EBR-II power level, rod size, and azimuthal location in row 6

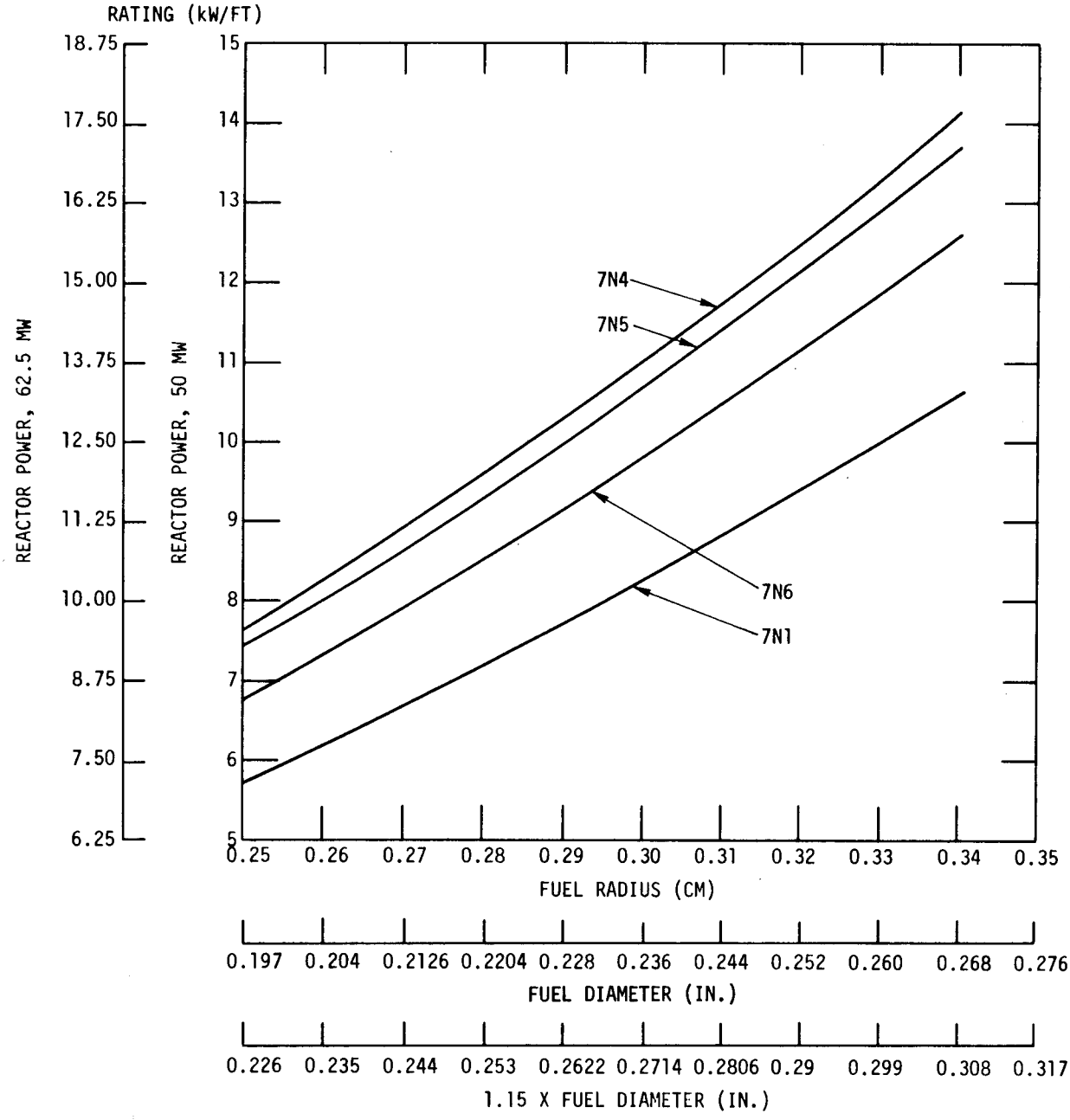

Fig. 4.25. $(Pu,U)O_2$ fuel rod linear heat rating as a function of EBR-II reactor power level, rod size, and azimuthal location in row 7

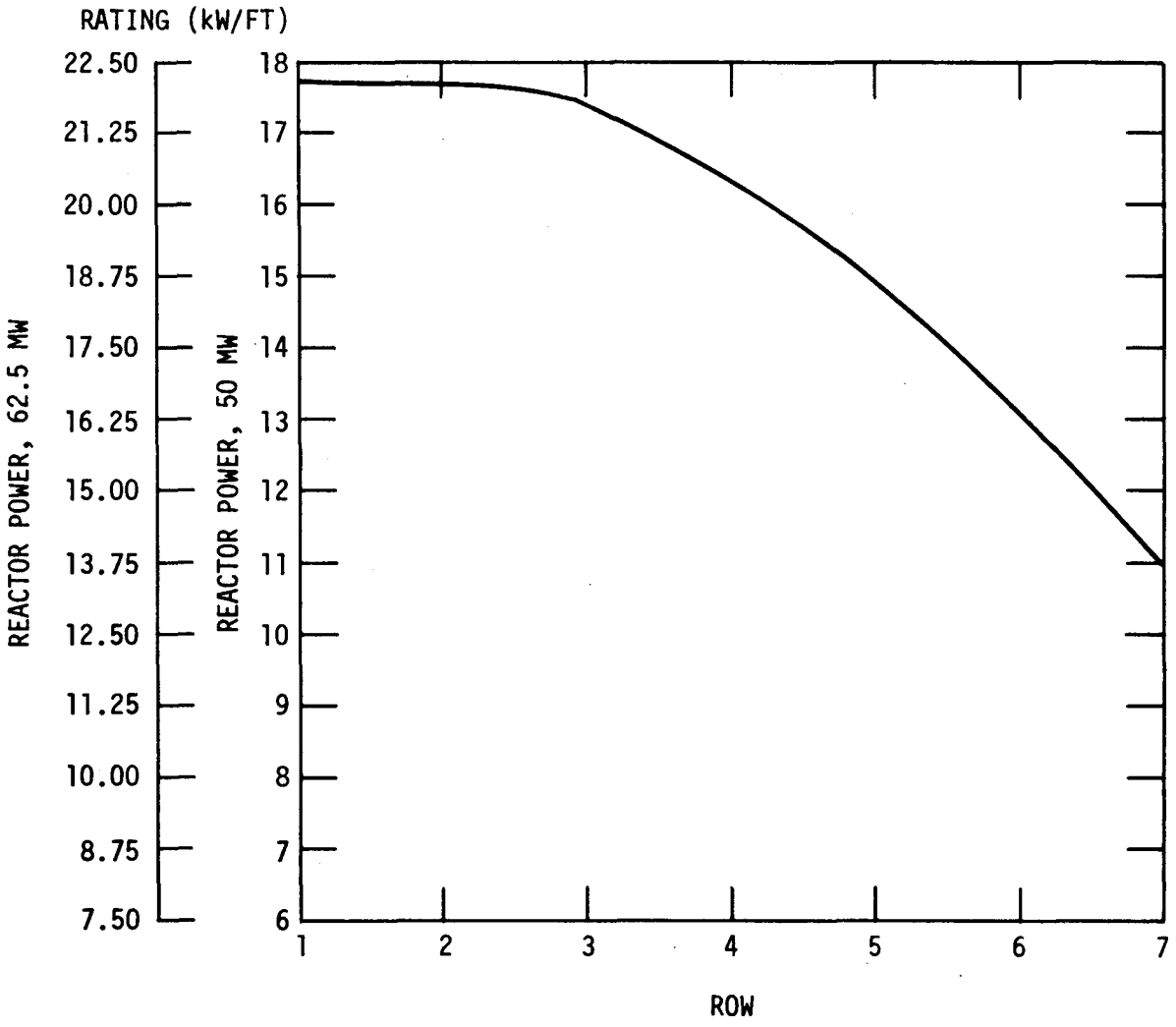

Fig. 4.26. Maximum $(Pu,U)O_2$ fuel rod linear rating at the EBR-II core centerline for a rod with a cladding o.d. of ∿0.27 in. and an o.d./id. of 1.15 and 15% Pu-85% U fuel as a function of EBR-II reactor power level and row position

containing GCFR fuel (i.e., $0.85UO_2$-$0.15\ PuO_2$). Figure 4.27 depicts the dependence of linear rating upon Pu content; the insensitivity exists because the fission cross section of this highly enriched U is approximately equal to that of Pu. The linear ratings given on these curves are maximum values, i.e., at the core centerline in the pin nearest the center of the core. They may be converted to average values by division by the the axial peak-to-average or the flux tilt across the row.

The increase in linear rating due to gamma heating may be estimated from Fig.17 of Ref. 36. In row 7, the inner blanket row (where it would be expected that the contribution of gamma heating would be largest), the heat deposition is 6.75 W/g U or, in terms of equivalent fissions, 0.03734 x 10^{13} f/g-sec. It is apparent from Table 4.12 that this will increase the linear rating by approximately 6.5% at the maximum pin centerline.

4.5.5.2. Flux Tilt Across Row 7. The magnitude of the flux tilt across the subassembly was estimated as follows:

1. The published fission rates (Table 4.12) imply a max-to-average flux of approximately 1.16. This value, based upon a depleted blanket element adjacent to the core, overestimates the tilt in a heavily fueled experimental subassembly.

2. A 33-group transport theory problem was run in which it was assumed that a ring of experimental subassemblies enclosed the core. The calculated flux tilt was 1.08. This is an underestimate of the actual tilt because the depression caused by the depleted blanket elements in row 7 adjacent to the experiment was not accounted for.

These results therefore imply that

$$1.08 < \text{flux tilt} < 1.16 \quad ,$$

i.e., the tilt is within acceptable bounds.

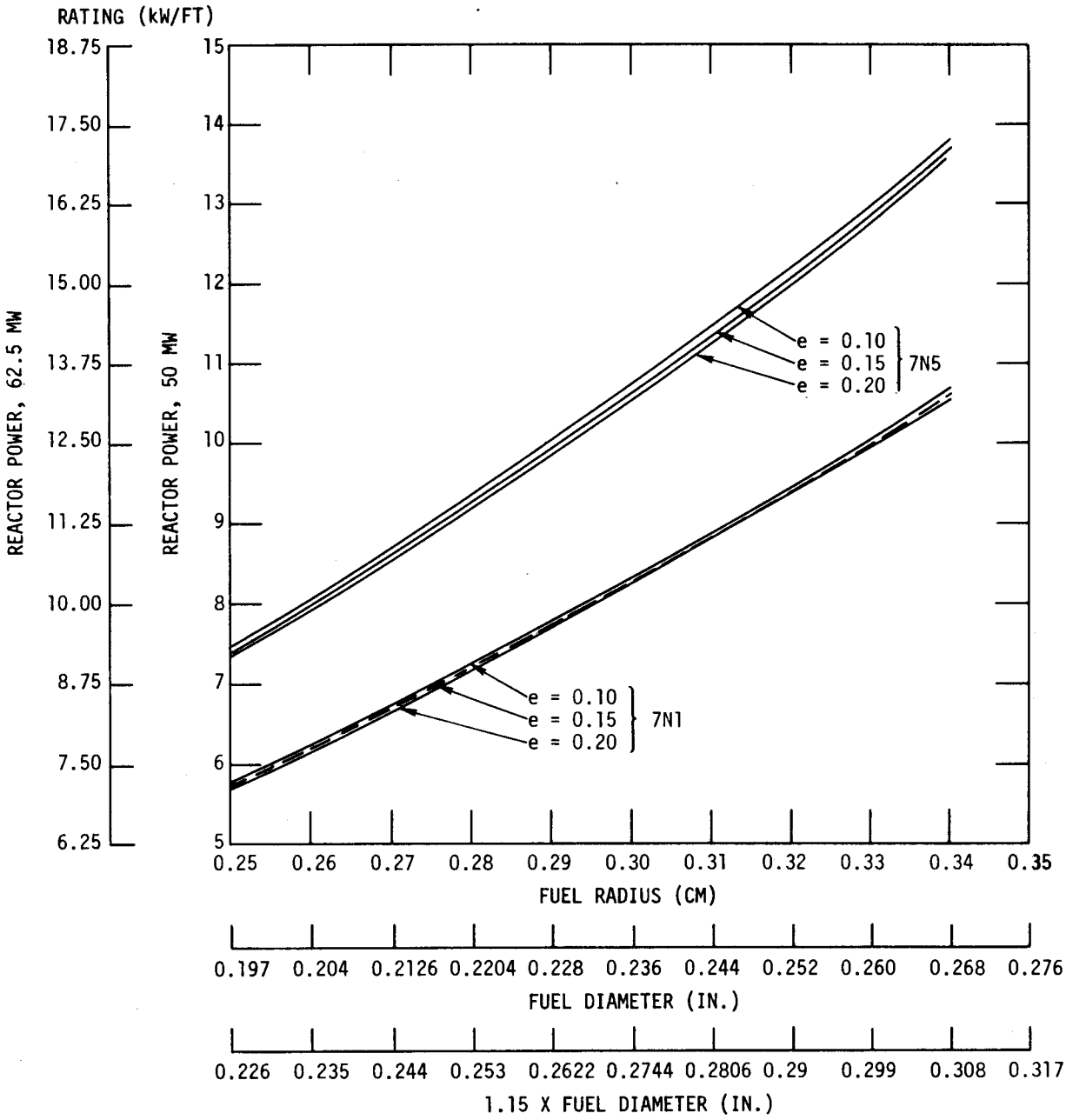

Fig. 4.27. $(Pu,U)O_2$ fuel rod linear rating in row 7 of EBR-II reactor for several plutonium concentrations as a function of EBR-II reactor power level, rod size, and azimuthal location

4.5.5.3. Reactivity Perturbation. The reactivity addition to the core was estimated by running a IDF similar to the case mentioned above except that blanket elements replaced the experimental ring. The loss in reactivity was 0.03378 Δk, and, since there are 36 elements in row 7, it follows that one experimental subassembly will increase the system eigenvalue by approximately 0.00094 Δk, a negligible amount.

4.5.5.4. Future Studies. Future analyses, based upon a specific subassembly position, will be oriented towards the elimination of approximations as well as the determination of the fine detail of the in-capsule flux. In particular:

1. The gross flux shape across the experimental subassembly will be calculated using a hexagonal mesh, two-dimensional diffusion theory code.

2. The gamma heating will be calculated by use of the PATH code.

3. The fine detail of the in-capsule flux will be computed using two-dimensional transport theory.

4.6. THERMAL-CYCLING RIG

The thermal cycling rig is in the check out phase to verify that power and pressure can be cycled on a simulated fuel rod over expected ranges for the GCFR. The check out continued at higher power levels during this quarter. Previously (Ref. 33) the rig was run successfully at 10 kW/ft with cladding temperatures of about 615 C. Several changes were made for the 12 kW/ft run; the heater length was increased to decrease the axial temperature gradient near the rod center, the heater diameter was increased to maintain a constant heat flux on the heater surface as in previous runs, the UO_2 was increased to accommodate the larger heater and the cladding to heat sink gap was decreased to 0.003 in. to keep cladding temperature in the desired range at the higher heat flux.

The first run was made at a reduced power level of 4 kW/ft for 24 hr that was then raised to 12.1 kW/ft, resulting in cladding temperatures of 480 C to 600 C for the four thermocouples at 90-deg circumferential positions at the cladding midlength. The test terminated after 2.8 hr at 12.1 kW/ft Upon disassembly it was found that a tungsten heater burnout had occured at the connection to the lower molybdenum connector. This was believed to have been caused by the extended heater connection operating in a portion of the heat sink that was not adequately cooled. Whisker growth was noted on the heater after the relatively short time at full power.

The heater length was decreased to its oroginal value and Pt washers were placed at each threaded end connection between the W and Mo to serve as a braze to decrease resistance in the threaded joint. In normal operation this point should operate below the melting temperature of Pt, but in case of increased resistance the ohmic heating would cause the Pt to melt and form a brazed joint. The second run was started and as power was increased excessive heating at 6.1 kW/ft of the top Mo connector where it passed through a rubber O-ring was noted. Cladding temperatures were 370 C, 370 C, and 330 C. The test was discontinued and examination indicated a failure in electrical insulation in the normally low-temperature region, allowing possible shorting-out to the pressure chamber.

Another sample is being set up with improved end electrical insulation which can withstand higher temperatures, and a somewhat smaller heater will be used to avoid whisker growth on the W, allowing shorting out to the UO_2 pellet i.d. The experiment capabilities of the thermal cycling rig are well enough known to plan a program of experimental work for the next quarter.

REFERENCES

1. "Development of Fuel Elements for Fast Breeder Reactors" Euratom Report EUR FNR-472 (also Karlsruhe Report KFK-700) p. V-1, December 1967.

2. Thompson, W. I., Gulf General Atomic Incorporated "Interpretation of Thermal Irradiations of Fast Reactor Fuel Elements," unpublished data.

3. Farnsworth, P. L., et al., "Creep Behavior of Mixed Oxides," Battelle Northwest Laboratory contribution to the 27th High Temperature Fuels Committee Meeting, December 1968, page F-1.

4. Clauer, A. H., M. S. Seltzer, and B. A. Wilcox, "Mechanisms of Creep in UO_2 and UO_2-PuO_2," in "Progress on Development of Materials and Technology for Advanced Reactors During October-December 1968," USAEC Report BMI-1857, Battelle Memorial Institute, January 1969.

5. Nabarro, F. R. N., Report Conference on Strength of Solids, Physical Society of London, 1948, p. 275.

6. Herring, C., J. Appl. Phys. 21, 457 (1950).

7. Keller, D., Battelle Memorial Institute-Columbus, private communication.

8. Armostrong, W.M., and W. R. Irvine, J. Nucl. Mater. 9, 121 (1963).

9. Christie, G., and J. Williams, J. Nucl. Mater. 5, (1962).

10. Armostrong, W. M., and W. R. Irvine, J. Nucl. Mater. 12, 261 (1964).

11. Asamoto, R., General Electric Company (San Jose), private communication.

12. Perrin, J., Battelle Memorial Institute-Columbus, private communication.

13. Konobeevsky, S. T., N. F. Pravdyuk, and V. I. Kutaitsev "Effect of Irradiation on Structure and Properties of Fissionable Materials," First Geneva Conference Proceedings, United Nations, Geneva, 1955, v. 7, p. 433 (P/681).

14. Buckley, S. N., "The Relationship between Irradiation Growth in Mono- and Poly-Crystalline Alpha-Uranium," in the Proceedings of a Symposium on Uranium and Graphite held in London on 20 and 21 March 1962, The Institute of Metals, 1962, Monograph No. 27.

15. Roberts, A. C., and A. H. Cottrell, Phil. Mag. 1, 711 (1956).

16. Zaimovsky, A. S., "Influence of the Structure Properties of Uranium on its Behavior under Irradiation," Second Geneva Conference Proceedings, United Nations, Geneva, 1958, v. 5, p. 566 (P/2191).

17. Hesketh, R. V., Phil. Mag. 7, 1417 (1962).

18. Holmes, J. J., and L. O. Peterson, Phil. Mag. 16, 845 (1967).

19. Frost, B. R. T., "Studies of Irradiation Effects in Ceramic Fuels at Harwell," paper presented at the 71st Annual Meeting of the American Ceramic Society, May 1969, Paper 20-INS-69.

20. Brucklacher, D., W. Dienst, and F. Thuemmler, "Considerations of the Creep Behavior of UO_2 Under Neutron Irradiation, " paper presented at the 71st Annual Meeting of the American Ceramic Society, May 1969, Paper 9-INS-69. Also see Karlsruhe Report KFK 817, July 1968 (in German).

21. Wilson, W. R. D., J. A. Walowit, and J. N. Anno, "Mechanical and Thermal Analyses," in "Progress on Development of Materials and Technology for Advanced Reactors During October-December 1968," USAEC Report BMI-1857, Battelle Memorial Institute, January 1969.

22. Peterson, S. L., J. S. Perrin, and R. A. Wullaert, "Postirradiation Compressive Creep Testing of UO_2 and UO_2-PuO_2," in "Progress on Development of Materials and Technology for Advanced Reactors During October-December 1968," USAEC Report BMI-1857, Battelle Memorial Institute, January 1969.

23. Stiegler, J. O., E. E. Bloom, and J. R. Weir, Jr., "Report on Irradiation Effects in Reactor Structural Materials," Quarterly Progress Report, May-July 1968, USAEC Report BNWL-870, Battelle Northwest Laboratory, 1968, p.11.73.

24. Brager, H. R., "Reactor Fuels and Materials Development Programs for Fuels and Materials Branch of USAEC Division of Reactor Development and Technology," Quarterly Progress Report, July-September 1968, USAEC Report BNWL-919, Battelle Northwest Laboratory, 1968, p. 12.35.

25. Holmes, J. J., et al., Acta. Met. 16, 955 (1968).

26. Cawthorne, C., E. J. Fulton, and C. G. Bell, "Voids in the Cladding of Irradiated P.F.R. Type Fuel Elements," United Kingdom Atomic Energy Authority, Dounreay, Memo TRG-Memo-4345(D) (1968).

27. Cawthorne, C., and E. J. Fulton, Nature 216, 575 (1967).

28. Volin, T. E., and R. W. Balluffi, "Annealing Kinetics of Voids and the Self-Diffusion Coefficient in Aluminum," Phys. Status Solidi 25, 163 (1968).

29. Lifshitz, I. M., and V. V. Slyozov, Phys. Chem. Solids 19, 35 (1961).

30. Jost, W., Diffusion in Solids, Liquids, and Gases, Academic Press, New York, 1960.

31. Baumann, C. D. "Neutron Flux Spectra in the Experimental Facilities of the Oak Ridge Research Reactor," USAEC Report ORNL-3756, Oak Ridge National Laboratory, January 1965.

32. "Gas-Cooled Fast Breeder Reactor, Annual Progress Report for the Period Ending July 31, 1967," USAEC Report GA-8107, Gulf General Atomic Incorporated, June 25, 1968.

33. "Gas-Cooled Fast Breeder Reactor, Quarterly Progress Report for Period February 1, 1969 through April 30, 1969," USAEC Report GA-9359, Gulf General Atomic Incorporated, June 12, 1969.

34. "Gas-Cooled Fast Breeder Reactor, Quarterly Progress Report for the Period August 1 through October 31, 1968," USAEC Report GA-8895, Gulf General Atomic Incorporated, December 2, 1968.

35. "Gas-Cooled Fast Breeder Reactor, Quarterly Progress Report for the Period November 1, 1968 through January 31, 1969," USAEC Report GA-9229, Gulf General Atomic Incorporated, March 24, 1969.

36. "Guide for Irradiation Experiments in EBR-II," EBR-II Project Revision 3, Argonne National Laboratory, July 1969.

5. TASK D - REACTOR PHYSICS PROGRAM

5.1. INTRODUCTION

5.1.1. Purpose of the Program

Considerable effort is being expended on the experimental verification of neutronic calculations on fast spectrum reactors. There are at least a dozen large, fast critical assemblies planned or in operation in the USA, the USSR, and Europe. Most of this critical experiment work, however, is being performed in sodium-cooled reactor programs; hence, the systems considered and results obtained differ considerably from that suitable for the GCFR concept. And, while the applicable data from past, clean, fast critical experiments of the GODIVA type can be used to some extent to verify computational methods and high-energy cross sections for the GCFR program, there are unique characteristics and problems associated with the GCFR that require critical experiment verification. For example, the substitutions of helium for liquid metal coolants lead to considerably different reactivity coefficients, and the GCFR fuel is characterized by particularly high ratios of fertile to fissile material. In addition, methods for dealing with the reactivity changes induced by steam or water entry into the GCFR core need to be verified.

So that these different characteristics may be understood and the key reactor physics parameters verified, a detailed GCFR critical experiment program is being planned. This program includes a core mock-up of the reactor experiment, determination of the effect of water entry into the core, determination of reactivity coefficients and control-rod worth as a function of position in the core, and Doppler coefficient and reactivity worth measurements.

It had been determined earlier, however, that it would be possible to perform a series of simple, low cost, critical experiments and obtain data of immediate use to the overall GCFR project. These critical experiments would provide an initial check on calculational methods used in GCFR studies and the results obtained therefrom (such as conversion ratio, critical volume, etc.) and provide an integral check on cross sections, particularly cross sections for plutonium and the resonance poison materials hafnium, gadolinium,and dysprosium.

These experiments were performed at BNWL's Critical Mass Facility at Hanford, Washington, and consisted of the measurement of the critical mass and volume of bare cubical plutonium-fueled assemblies. In the experiments, conducted in 1967 and reported in Ref. 1, fuel which was a homogeneous mixture of plutonium-dioxide polystyrene with a 5 to 1, H to Pu ratio was used. The neutron spectrum of this system corresponds to that of a partially-flooded GCFR. These experiments were also conducted as part of the BNWL Critical Mass Facility's continuing program for the measurement of the critical mass and volume of plutonium fuel over the full range of densities and H to Pu ratios that can occur in reprocessing plants.

It was determined during these experiments that it should be feasible to produce plutonium fuel with a 1 to 1,H to Pu ratio. Results of critical assembly measurements with this fuel would considerably extend the range and usefulness of the data obtained from the 5 to 1 program; thus, an experimental program using this fuel was planned.

5.1.2. Experimental Program Description

The following experimental program was planned for the 1 to 1,H to Pu ratio, plutonium-fueled assemblies:

1. Measurement of the critical mass and size of an unclad, near-cube shape plutonium fuel with a 1 to 1,H to Pu ratio.

2. Measurement of the critical size and mass of an unclad, plutonium-fueled assembly of 1 to 1,H to Pu ratio with a base size suitable for the resonance-poison plates (e.g., 12 in. x 18 in.).

3. Measurement of the critical size and mass of an unclad,plutonium-fueled assembly of 1 to 1,H to Pu ratio containing layers of resonance-poison plates. (The number of poison layers added to be limited by the fuel available for criticality.):

    a. with Gadolinium-oxide plates
    b. with Hafnium-oxide plates
    c. with Dysprosium-oxide plates.

4. Measurement of the fission ratios for Pu-239 and U-235 in the unclad 1 to 1,H to Pu assembly (item 1), and flux distribution measurements in this unclad assembly and at least one of the poisoned systems.

5.1.3. Summary

Considerable difficulty was encountered in manufacturing plutonium fuel with a 1 to 1,H to Pu ratio, and only about 60 kg were finally produced for the experiments. Preliminary calculations had indicated that about 100 kg of this fuel would be required for criticality of an unclad cube at this H to Pu ratio. To overcome this problem a "driver" region of 5 to 1,H to Pu fuel, which was available at the BNWL Critical Mass Facility, was used to produce a critical system for the measurements. The experiments, with the exception of the fission ratio and flux distribution measurements, have been completed and an analysis of the results is underway.

Severe radiation and heating problems were encountered with the 1 to 1 fuel with the result that it was not found possible to perform the fission ratio and flux measurements because these experiments require considerable irradiation time in the critical assembly. It is planned that several

alternative experiments of interest in the GCFR program will be performed in place of these measurements. These alternative experiments were not included in the initial experimental program because of budget and time limitations. The choice of the particular experiments will be made after the analysis of the completed measurements.

5.2. EXPERIMENTAL PROGRAM

5.2.1. Facility Description

The critical experiments were conducted in a large plutonium handling glove box within a heavily shielded cell at BNWL (Ref. 2). The critical arrays, in the form of rectangular prisms, were assembled by the Remote Split-Table Machine (RSTM) (Ref. 3) shown in Fig. 5.1 of Ref. 1. The RSTM consists of two table halves, one movable and one stationary. Together the table halves form a surface 30 in. wide, 42 in. (24 in. and 18 in.) long, and 20 in. above the floor level. Both table halves are covered by a 12-in.-thick, low-density aluminum honeycomb material (ρ = 0.037 g/cc), and the fuel assemblies were stacked on a 1/16-in.-thick aluminum plate resting on this honeycomb material. Thus, the effects of end reflection on the critical mass due to the supporting table were minimized. The table halves have a steel framework supporting the horizontally operated control rods. These control rods operate as movable reflectors and consist of a slab of polystyrene attached to a movable steel rod.

The movable half of the table rides horizontally on two 1.5-in.-diam steel shafts driven by a 1-hp direct current motor. Criticality of the fuel assemblies is achieved by bringing the two table halves together. The speed at which the faces are brought together is reduced automatically as the tables close.

The fuel assemblies themselves are contained and supported by thin aluminum braces at all four corners, attached to the base by magnetic clamps. In addition, one or two horizontal braces of thin aluminum are also attached to the vertical supports by magnetic clamps to ensure uniform

stacking of the fuel assemblies.

The experimental setup was simple and flexible, allowing changes in the program with relative ease. There are, however, definite limitations to this type of experiment. Since no equipment was available for reactivity worth measurements by small sample oscillation techniques and since the basic measurement that could be performed was that of the height of a critical assembly, the worth of the poison materials had to be measured by introducing a large quantity of the material into the system. Addition of a large quantity produced inhomogeneities in the critical assembly and considerably complicated the analysis of the results, which were obtained using the one-dimensional transport codes available. The unpoisoned systems, however, were more easily amenable to analysis.

5.2.2. Fuel Element Design

The fuel used for the previous experiments (5 to 1,H to Pu ratio) had been formed as coated compacts of a homogeneous mixture of plutonium-dioxide and polystyrene powder, with the mixture being adjusted to give a 5 to 1,H to Pu ratio. The polystyrene served as a binder for the fuel and the means to produce the required H to Pu ratio. The fuel was pressed into 2-in. x 2-in. x 1-in. compacts and hand stacked on the RSTM to form the critical assembly. Polystyrene was chosen as the matrix material because of its excellent molding properties at the high temperatures and pressures used in forming the compacts and its stability under alpha irradiation from the radioactive plutonium. However, polystyrene starts to soften at about 90 C, which placed an upper limit on the temperatures that could be allowed in these assemblies. The heat is generated internally by alpha decay in the plutonium.

It was not possible to use polystyrene as the matrix material in the 1 to 1,H to Pu fuel compacts. This was mainly due to the higher heat generation in the plutonium. In addition, the 1 to 1,H to Pu ratio requirement resulted in the use of too little polystyrene for it to serve as a useful binder. After some experimentation it was found that the unmoderated

PuO_2 could be sufficiently compacted to form a useful fuel block. Further mechanical strength and contamination control was provided by a relatively thick layer of a special, temperature-resistant polyvinyl chloride tape surrounding the PuO_2 fuel compact. The H to Pu ratio was provided by water absorbed on the PuO_2 fuel particles and by the hydrogen in the tape coating. The actual H to Pu ratio resulting from this manufacturing procedure was measured as 0.62 to 1. A summary of the fuel compact data is provided in Table 5.1. These data are based on measurements of 20 individual fuel compacts.

5.2.3. Experimental Results

The results of the critical assembly measurements are summarized in Table 5.2. The quoted experimental errors include uncertainties in fuel compact data as well as uncertainties in the critical height measurement.

In addition to the critical assembly data summarized in Table 5.2, measurements were performed to evaluate various experimental corrections, such as temperature and coating thickness effects and reproducibility. As indicated in the table, these corrections have been included in the experimental results.

The resonance poison material was the same as that used in the 5 to 1 experiments reported in Ref. 1. The poison material, hafnium, gadolinium, and dysprosium in the form of powdered oxides was compacted in 20-mil-thick stainless steel containers. Data on these poison containers are summarized in Table 5.3.

5.2.4. Experimental Procedure

The fuel compacts were hand-stacked on the RSTM table halves with the table faces fully open. Initially, a configuration that was well below critical was stacked. Aluminum braces were used to ensure uniform stacking. When considered necessary, thermocouples were added between

TABLE 5.1

PuO_2 FUEL DESCRIPTION

AVERAGE DIMENSIONS AND WEIGHTS

Fuel block with cladding	2.169 in. x 2.169 in. x 1.606 in.
Fuel block with cladding and stacking voids	2.183 in. x 2.183 in. x 1.609 in.
Fuel block without cladding	2.020 in. x 2.020 in. x 1.501 in.
PuO_2 per fuel block (including 0.014 wt-% H_2O)	660.836 ± 2.714 g
Pu per fuel block	581.454 ± 2.388 g
Cladding material per block	24.5 ± 0.3 g

ISOTOPIC COMPOSITION OF PLUTONIUM (wt-%)

Pu-238	0.232 ± 0.020
Pu-239	75.228 ± 0.305
Pu-240	18.354 ± 0.219
Pu-241	5.048 ± 0.191
Pu-242	1.138 ± 0.170

COMPOSITION OF CLADDING MATERIAL (wt-%)

C	45.62
N	0.30
H	6.08
O	48.00

PuO_2 PARTICLE SIZE (mm)

Maximum	0.0450
Mean	0.0083
Minimum	0.0025

TABLE 5.2

BARE PuO_2 EXPERIMENTAL DATA[a]

Experiment Number	Description of Critical Assembly	Driver Region[b]			PuO_2 Region[b]		
		Base (cm)	Height (cm)	Mass (kg Pu)	Base (cm)	Height (cm)	Mass (kg Pu)
18-000-003	7 layers driver fuel plus 2.35 layers PuO_2	31.26x30.96	27.16	57.9±0.29	33.27x33.27	9.76	49.3±0.28
18-000-004	7-2/3 layers driver fuel followed by 1 layer PuO_2, 1-1/32-in. Al plate, and 1.28 layers PuO_2	31.26x30.96	29.96	63.6±0.31	33.27x33.27	9.44	47.9±0.28
18-000-005	8-1/3 layers driver fuel followed by 1 layer PuO_2, 1 layer Dy_2O_3, and 1.15 layers PuO_2	31.26x30.96	32.44[c]	69.3±0.34	33.27x33.27	8.84	45.0±0.26
18-000-006	8-1/3 layers driver fuel followed by 1 layer PuO_2, 1 layer Gd_2O_3, and 1.15 layers PuO_2	31.26x30.96	32.44[c]	69.3±0.34	33.27x33.27	8.84	45.0±0.26
18-000-007	8-1/3 layers driver fuel followed by 1 layer PuO_2, 1 layer HfO, and 1.16 layers PuO_2	31.26x30.96	32.44[c]	69.3±0.34	33.27x33.27	8.87	45.2±0.26
18-000-008	8-1/3 layers driver fuel plus 1.92 layers PuO_2	31.26x30.96	32.44	69.3±0.34	33.27x33.27	7.83	40.2±0.24

[a] From BNWL Critical Mass Facility (Ref. 2)

[b] Data corrected to a central core temperature of 60 C.

[c] Quoted height does not include poison plate layer thickness.

TABLE 5.3

RESONANCE POISON DATA

Parameters	Gd_2O_3	HfO_2	Dy_2O_3
Size of container (in.)	6 x 6 x 0.25	6 x 6 x 0.25	6 x 6 x 0.25
Average mass of oxide powder in container (g)	203.8	593.2	333.6
Average density of oxide powder in container (g/cc)	1.38	4.02	2.26

fuel compact layers to monitor the temperature of the assembly during the experiment. After personnel had left the area and the room was sealed, the table faces were brought together by remote methods. A polyethylene reflector control rod was positioned next to the stationary face during and after the closure. The fuel compacts were stacked so that the faces of the assembly, which come in contact when the table halves are closed, projected slightly (less than 1/8 in.) over the table-half edges. This ensures positive contact on closure and good reproducibility during repeated closures because the two faces were pushed tightly together and matched exactly on reclosure.

After closure, the multiplication of the assembly was measured, using three proportional neutron counters with scaling circuits. Spontanious fission, primarily from Pu-240, provided the required neutron source. Two multiplication measurements were made during each closure, one with the reflector rod in place and one with the reflector rod removed. A current plot of inverse multiplication versus height was maintained during the experiment, and the height required for criticality was estimated after each closure. The amount of fuel added during the next stacking was half, or less than the estimate required for criticality.

After the measurements had been made, the fuel stacks were separated and further fuel additions were made. The complete procedure was then repeated until criticality was achieved with the reflector control rod in position. The height of the unclad system for criticality without the reflector control rod was then obtained by extrapolation of the inverse multiplication curve for the unclad system parallel to the reflector inverse multiplication curve.

Because criticality often required less than a complete layer of 1/2 in. high fuel compacts and because there is always some small deviation in the results of the three neutron detectors, a least squares analysis of the inverse neutron multiplication data was used to obtain the critical dimensions.

5.2.5. Analysis of Experiments

A summary of the results of the analysis is presented in Table 5.4. In addition to the calculation of the 1 to 1,H to Pu critical assemblies, three other critical experiments are being reevaluated using the current Pu-239 cross-section data sets of interest. These experiments are the 15 to 1 and 5 to 1,H to Pu critical assemblies measured at the BNWL Critical Mass Facility and at the Los Alamos Plutonium Metal Sphere. When combined with the 1 to 1,H to Pu experiments, the results of this analysis should yield a good integral check on Pu-239 cross-section data over the energy range of interest in the GCFR. The three Pu-239 evaluated cross-section data sets used in the analysis are summarized in Table 5.5.

TABLE 5.4

SUMMARY OF CRITICAL ASSEMBLY ANALYSIS RESULTS

Calculational Summary

System	Calculated k_{eff} Using 94.2394 Cross Section Data
JEZEBEL Pu-metal sphere	1.0141
1 to 1,H to Pu assembly 18-000-003	1.0358
5 to 1,H to Pu assembly	0.9985
15 to 1,H to Pu assembly	1.0210

Pu-239 Data Set Intercomparison Calculations

System Description	Calculated k_{eff} 94.2394	94.2396	94.2398
JEZEBEL, 12.568-cm-diam Pu sphere [a]	1.0141	1.0038	0.9822
34.04-cm-diam 1 to 1,H to Pu sphere [b]	1.000	0.9944	0.9750
38.98-cm-diam 5 to 1, H to Pu sphere [b]	1.000	1.0052	0.9854

[a] Actual, measured critical assembly.

[b] The diameters of these systems were chosen to give k_{eff} = 1.0 with 94.2394.

TABLE 5.5

Pu-239 CROSS SECTION DATA SET SUMMARY DESCRIPTION

Data Set Label	Description
94.2394	The evaluated data set of Drake and Dyos as compiled in Ref.4 was combined with a resolved resonance parameter set given in Ref. 5 and White's (Ref. 6) high energy data.
94.2396	Data taken from an evaluation by Schmidt et al. in Ref. 7, including resonance parameters.
94.2398	2-D scattering arrays were taken from Ref. 7 and the 1-D arrays (σ_f, σ_a, σ_{sc}, etc.) and resonance parameters were evaluated from various sources, including the latest ORNL and RPI "α" measurements.

REFERENCES

1. "Gas-Cooled Fast Breeder Reactor - Annual Progress Report for the Period Ending July 31, 1967," USAEC Report GA-8107, General Dynamics, General Atomic Division, July 31, 1967.

2. Reardon, W. A., et al., "Hazards Summary Report for the Hanford Plutonium Critical Mass Laboratory," USAEC Report HW-66266, Hanford Atomic Products Operation, General Electric Company, August 1, 1966.

3. Richey, C. R., et al., "Hazards Summary Report for the Hanford Plutonium Critical Mass Laboratory, Supplement No. 1 - The Remote Split-Table Machine," USAEC Report HW-66266 Hanford Atomic Products Operation, General Electric Company, October 1963.

4. Drake, M. K., and M. W. Dyos, "A Compilation and Evaluation for the Major Plutonium Isotopes," USAEC Report GA-6576, General Dynamics, General Atomic Division, July 30, 1965.

5. Baxter, A., "Resolved Resonance Parameters for Pu-239," USAEC Informal Report GAMD-8077, General Dynamics, General Atomic Division, July 7, 1967.

6. White, P. H., J. G. Hodgekinson, and G. J. Wall, "Measurement of Fission Cross Sections for Neutrons of Energies in the Range 40-500 keV," paper SM 60/14 presented at the JAEA Symposium on the Physics and Chemistry of Fission, Salzberg, Austria, March 22-26, 1965.

7. Langer, I., J. J. Schmidt, and W. Woll, "Tables of Evaluated Neutron Cross Sections for Fast Reactor Materials, Karlsruhe Report KFK-750,Kernforschungszentrum, Karlsruhe (West Germany Institut fuer Material und Festkoerperforschung), January 1968.